STRUCTURAL CHARACTERIZATION OF THE PHITSANULOK BASIN, ONSHORE THAILAND, AND INVERTED PULL-APART BASIN SANDBOX ANALOG MODELS

A Thesis Presented to

the Faculty of the Department of Earth and Atmospheric Sciences

University of Houston

In Partial Fulfillment

of the Requirements for the Degree

Master of Science

By

Phinphorn Amonpantang

May 2019

STRUCTURAL CHARACTERIZATION OF THE PHITSANULOK BASIN, ONSHORE THAILAND, AND INVERTED PULL-APART BASIN SANDBOX ANALOG MODELS

Phinphorn Amonpantang

APPROVED:

Dr. Jonny Wu, Chairman

Dr. Paul Mann

Dr. Elizabeth Baker

Dr. Dan E. Wells, Dean, College of Natural Sciences and Mathematics

ACKNOWLEDGEMENT

I would like to express my deepest appreciation to all those who gave me the possibility to complete this thesis project. Firstly, I am extremely grateful to PTT Exploration and Production Ltd. who support me a scholarship and Phitsanulok basin data for the master's degree and thesis project. I am especially indebted to my thesis advisor Dr. Jonny Wu, department of Earth and Atmospheric Sciences, who always gave me a great supervise through the thesis project. I would like to thank to my committee Dr. Paul Mann and Dr. Elizabeth Baker for invaluable insight into regional tectonic analysis.

This thesis project would not have been possible without the Blueblack Toolbox seismic software and Petrel license from Cegal Group AS Software company and Schlumberger Limited.

I would like to extend my sincere thanks to Dr. Sarawute Chantraprasert, and Ms. Kamonporn Inraikhing for their valuable advices and ideas.

I would also like to extend my thanks to the PTTEP Senior vice president and vice president, Mr. Nopadon Chinabutr, Mr. Supakorn Krisadasima, and Mr.Dittapon Soothi-O-Soth, for permission to use all the require data. Many thanks to Mr. Prarop Sirisali, PTTEP's lawyer, for processing the confidential agreement. Special thanks to Sirikit Oilfield stuff for providing me data.

I also want to thank tectonics and structural student group, who learn and support together over one and a half year of my M.Sc. study at University of Houston.

STRUCTURAL CHARACTERIZATION OF THE PHITSANULOK BASIN, ONSHORE THAILAND, AND INVERTED PULL-APART BASIN SANDBOX ANALOG MODELS

An Abstract of a Thesis

Presented to

the Faculty of the Department of Earth and Atmospheric Sciences

University of Houston

In Partial Fulfillment

of the Requirements for the Degree

Master of Science

By

Phinphorn Amonpantang

May 2019

ABSTRACT

The Phitsanulok basin is the largest onshore rift basin in Thailand and has been a major hydrocarbon producer for over 30 years. Due to its proximity to the India-Asia collision, the Phitsanulok basin was subjected to transtensional rifting, transtensional to transpressional reactivation, post-rift thermal subsidence, and late inversion between the early Miocene to present. It is recognized that the northern Phitsanulok basin is predominantly extensional whereas the southern Phitsanulok basin has experienced inversion that has produced unconformities, folding, and reverse faults. However, the transition between these domains has not been well-quantified, nor are the possible hydrocarbon implications. This study had two aims: (1) structurally characterize the Phitsanulok basin from an extensive 2D and 3D seismic petroleum industry dataset and examine the basin structure within a regional tectonic context; and, (2) structural analysis of the complex, internal geometry of inverted pull-apart basin sandbox models through the development of a new 3D analog model reconstruction method using Petrel software. In Study 1, analysis of structural styles, time structure and isochron maps, fault patterns, fault dip angles, fault throws, and fault azimuths, newly define a Northern and Southern structural domain across 16°50'N latitudes. Our interpreted 16°50'N structural boundary occurs near the southern limit of major earthquakes, changes in regional fault trends, and a possible terrane boundary, which suggests the structural domains could be controlled by deep structures. We compare our structural domains to Phitsanulok Basin hydrocarbon data (i.e. hydrocarbons in place, production rates) and show the hydrocarbon implications. In Study 2, we found that inverted pull-apart basins formed rhomboidal basins that hosted complex border faults and a throughgoing cross-basin fault system. 3D analysis of the internal sandbox model geometries using our newly developed workflow revealed two distinct fault azimuth populations (0° - 5° and 35° - 40°) relative to the master strike-slip faults, changes in fault-dip angles, and increased inactive faults during pull-apart basin inversion.

CONTENTS

Chapter 1 Introduction

1.1. Geographic setting and significance

The Phitsanulok basin is located approximately 400 km north of Bangkok, Thailand, and is the largest Cenozoic-aged, onshore Thailand sedimentary basin (Figure 1.1) (Flint *et al*., 1988). The Phitsanulok basin covers an area of ~6,000 km^2 and contains up to 8 km of sediments (Flint *et al*., 1988). Commercial hydrocarbon accumulations have been proven within the Phitsanulok basin since the 1980’s (Thai Shell Exploration and Production Co.Ltd, 1988). The Phitsanulok basin has produced hydrocarbon for more than 30 years and the current production rate is around 25,000 bbl/d (PTTEP, 2017a). This thesis has two aims: (1) to structurally characterize the Phitsanulok basin from an extensive 2D and 3D seismic petroleum industry dataset and examine the basin structure within a regional tectonic context; and, (2) structural analysis of the complex, internal geometry of inverted pull-apart basin sandbox models through the development of a new 3D analog model reconstruction method using Petrel software. Section 1.6 provides a more detailed description of the thesis aims.

1.2. Regional tectonic setting

The Phitsanulok basin is generally considered to be an intracratonic rift basin that formed within a complex convergent zone formed by multiple plates including the Indian and Eurasian plates, and Sundaland (Bal *et al*., 1992; Charusiri and Pum-Im, 2009; Morley *et al*., 2011a; Morley *et al*., 2001; Packham, 1993; Polachan *et al*., 1991; Pubellier and Morley, 2014). The basin is surrounded by four main faults: the Mae Ping fault, the Uttaradit fault, the Phetchabun fault, and the Western Boundary fault (Figure 1.2) (Flint *et al*., 1988; Thai Shell Exploration and Production Co.Ltd, 1988). Regional fault patterns show a conspicuous change in strike across the Phitsanulok basin, from N to S orientations to the north and N to S and NNE to SSW orientations to the south (Figure 1.2, 1.3).

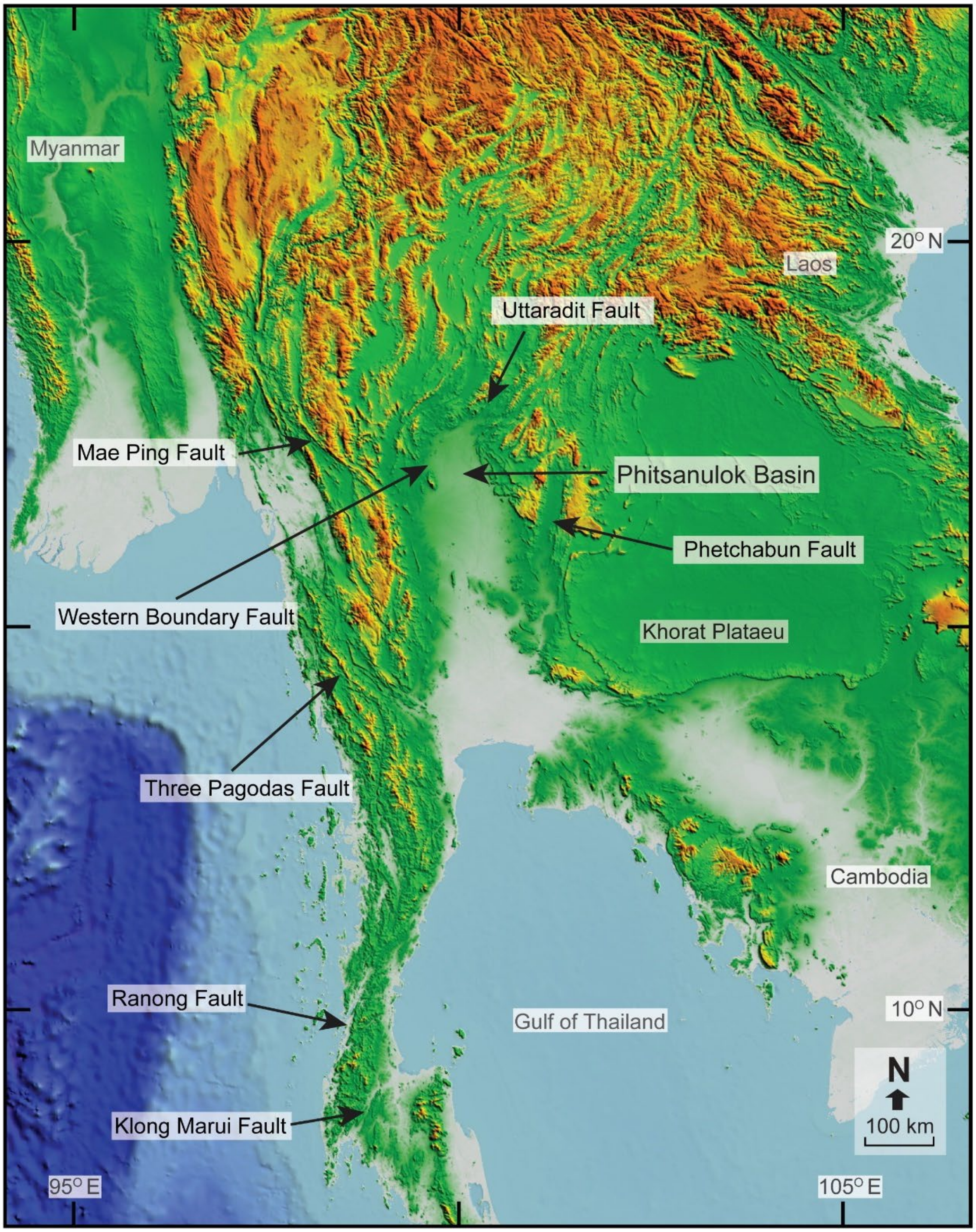

Figure 1.1 Southeast Asia Digital Elevation Model (DEM) showing the Phitsanulok basin location and surrounding tectonic features.

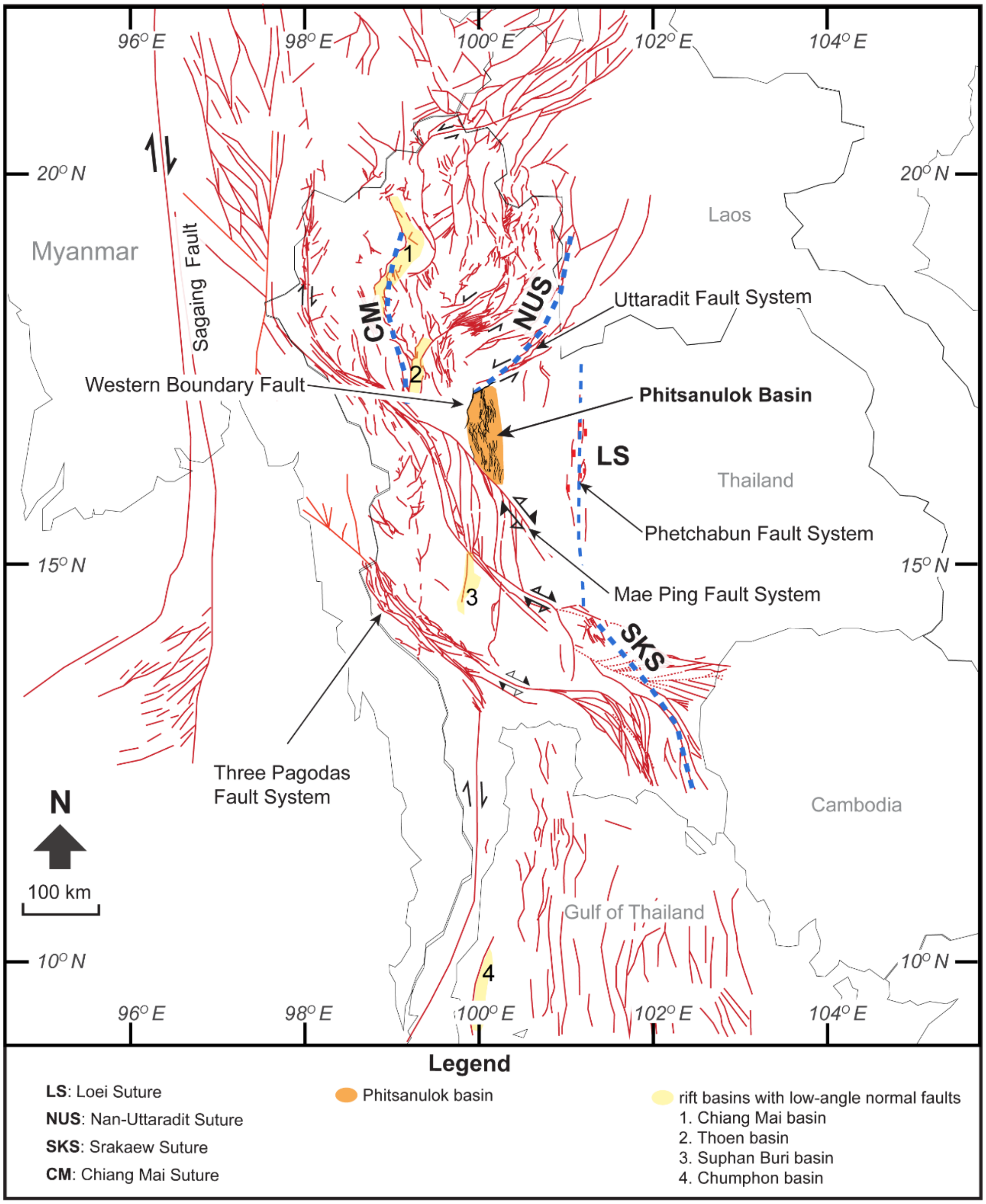

Figure 1.2 Central Thailand regional structure map showing the Phitsanulok basin location. Interpreted faults are shown by the red lines (modified from Morley, 2009). The Phitsanulok basin is situated between four regional fault systems: the Mae Ping fault, Uttaradit fault, Phetchabun fault and the Western Boundary fault, which is a low-angle normal fault. Other Thailand rift basins bounded by low-angle normal faults are shown in the yellow fill.

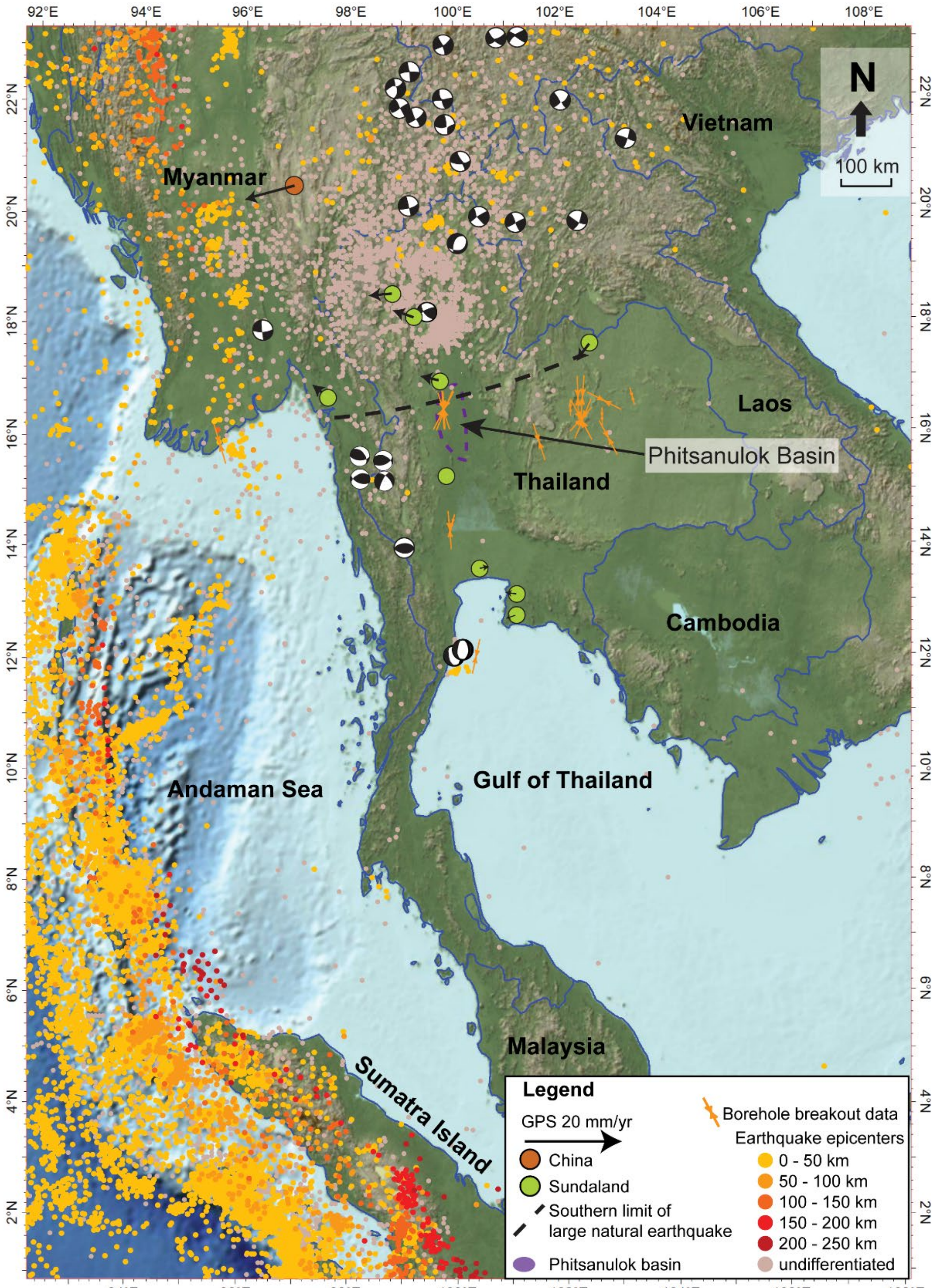

Figure 1.3 Southeast Asia digital elevation model (30 m DEM) illustrates with; modern GPS velocity from Simons *et al*. (2007) relative to China and Sundaland; south east Asia earthquake epicenters from Thai Meteorological Department (TMD) (Pailoplee, 2014) and https://earthquake.usgs.gov/ earthquakes/browse/stats.php; and borehole breakout analysis data from Tingay *et al*. (2010).

The Phitsanulok basin is in a region of slow westward motions (<10 mm/yr) relative to Sundaland (Figure 1.3). It has been observed that earthquake frequencies decrease dramatically to the south of the Phitsanulok basin (Figure 1.3) (Morley *et al*., 2011a). Earthquakes to the north show strike-slip hypocenters (Figure 1.3). The south of the Phitsanulok basin, earthquake focal mechanisms were non-strike-slip (i.e. normal, reverse, and oblique reverse slips) (Figure 1.3). The modern stress state near the basin is oriented approximately N - S based on borehole breakouts (Figure 1.3).

The Phitsanulok basin is thought to be located near or above a transition between the more rigid Sibumasu and Nakhon-Thai (Indochina) continental blocks (Figure 1.4). The nature of the basement below Phitsanulok basin is debated; uncertainty exists whether the Sukhothai arc subduction complex extends below the basin (Figure 1.4) (Ridd *et al*., 2011). Alternatively, the Phitsanulok basin may overlie the Nan-Srakaew Suture (Figure 1.5a & b) (Charusiri, 2002; Charusiri and Pum-Im, 2009). It is thought that the 'Western Boundary fault', a low-angle extension fault, could be formed above older thrusts within the suture zone (Figure 1.5b). Regardless, based on regional fault patterns (Figure 1.2), present-day seismotectonics (Figure 1.3) and basement maps (Figure 1.4), it seems the Phitsanulok basin could be located above or near an importance tectonic transition within Thailand. In this thesis, we will conduct a tectonostratigraphic analysis of the Phitsanulok basin and later place our observations against the regional tectonic framework.

1.3. Phitsanulok basin evolutionary history

The Phitsanulok basin initiated during divergent dextral strike-slip movement on the Mae Ping and sinistral strike-slip movement of Uttaradit fault system during the Paleogene period, which produced extension along the 'Western Boundary fault' (Bal *et al*., 1992; Charusiri and Pum-Im, 2009; Flint *et al*., 1988; Polachan *et al*., 1991). According to Thai Shell Exploration and Production Co.Ltd (1988), the first evolutionary phase was started by transtension along the

Western Boundary Fault (Figure 1.6a). In this stage the Phitsanulok basin was opening in the E-W direction and created extensional faults that showed N - S major trends (Morley *et al*., 2007; Morley, 2009). A phase of complex transtension to transpression then occurred within the southern area of the basin from 18 Ma to 5 Ma that included periods of tectonic inversion (Figure 1.6b) (Morley *et al*., 2007; Morley *et al*., 2001; Morley, 2009; PTTEP, 1998). The linkage of faults within the central part area of the Phitsanulok basin occurred during two tectonic phases, producing vertically-discontinuous normal faults (Morley, 2017; Morley *et al*., 2007). In this phase the inversion was introduced into the Phitsanulok basin due to the dextral slip action of the Mae Ping fault system. Some models consider that the basin experienced a final phase of post-rift thermal subsidence after 10 Ma (Figure 1.6c) (Bahae, 2017). Two alternative tectonic evolution models are shown in Figure 1.7 tectonics model.

1.4. Basin stratigraphy

The Phitsanulok basin consists of six lithostratigraphic units that were deposited between the Paleogene period to recent: the Sarabop, Chum Saeng, Lan Krabu (LKU), Pratu Tao (PTO), Yom, and Ping formations (Figure 1.7) (Flint *et al*., 1988; Thai Shell Exploration and Production Co. Ltd, 1988). These formations were deposited in continental depositional environments that included alluvial systems, lacustrine deltas, open lake, and fluvial systems (Bal *et al*., 1992).

Within the Sarabop and Nong Bua formation, the earliest sediments were deposited within an alluvial fan (Figure 1.7 stratigraphy) (Morley *et al*., 2011b). The Sarabop formation was separated from the Chum Saeng and LKU from the thin lacustrine shale layer which called Lower intermediate seal (LIS) (Flint *et al*., 1988; Morley *et al*., 2011b). The basin then became a lacustrine environment and the Chum Saeng and LKU formations were deposited within an interfingering pattern (Figure 1.7 stratigraphy). The LKU formation contains the seismic marker H 40 or LKU-L of 18 Ma age which is equivalent to the Lower Early Miocene from well log data

(Figure 1.7) (PTTEP, 2017b). Alternating layers of sandstones and shales within the Chum Saeng and LKU formations created good hydrocarbon reservoirs and seals (Flint *et al*., 1988).

There was another thin lacustrine shale between the top of LKU-L formation and top of the Chum Saeng formation (Flint *et al*., 1988; Morley *et al*., 2011b). This thin layer shale was called Upper Intermediate Seal (UIS). Then the basin was filled by the maximum flooding surface or Chum Saeng formation (PTTEP, 2017b; Thai Shell Exploration and Production Co.Ltd, 1988). The top of the Chum Saeng formation is a key seismic marker H20 or Main seal of Upper Early Miocene that represents a 17 Ma age (Figure 1.7) (PTTEP, 2017b). The PTO formation is comprised of fluvio-deltaic sediments and was deposited on top of the Chum Saeng Formation. The Yom formation, which is deposited during the Pliocene period sediment, recorded a fluvial system that developed after deposition of the Chum Saeng formation sediments. The 10 Ma, end of transtension – transtension from Bahae (2017) model, was presented in intra Yom formation (PTTEP, 2017b). The Ping formation, the last sediment package, deposited on top of the Yom formation.

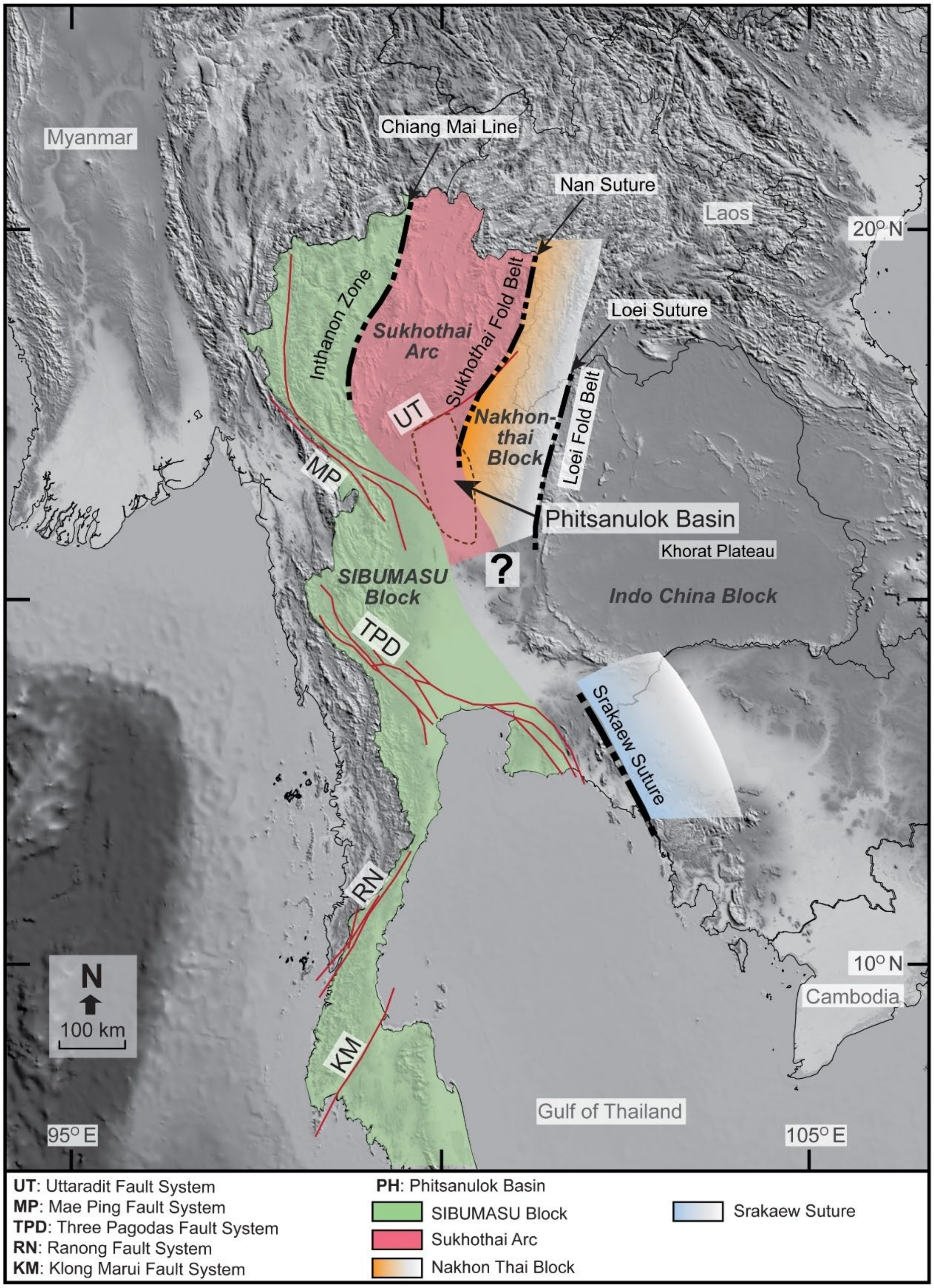

Figure 1.4 Tectonic basement map of Thailand illustrates with fold belt and suture location superimposed on a Digital Elevation Model. Sibumasu block (green area); Sukhothai arc (pink); and Nakhonthai block (yellow).

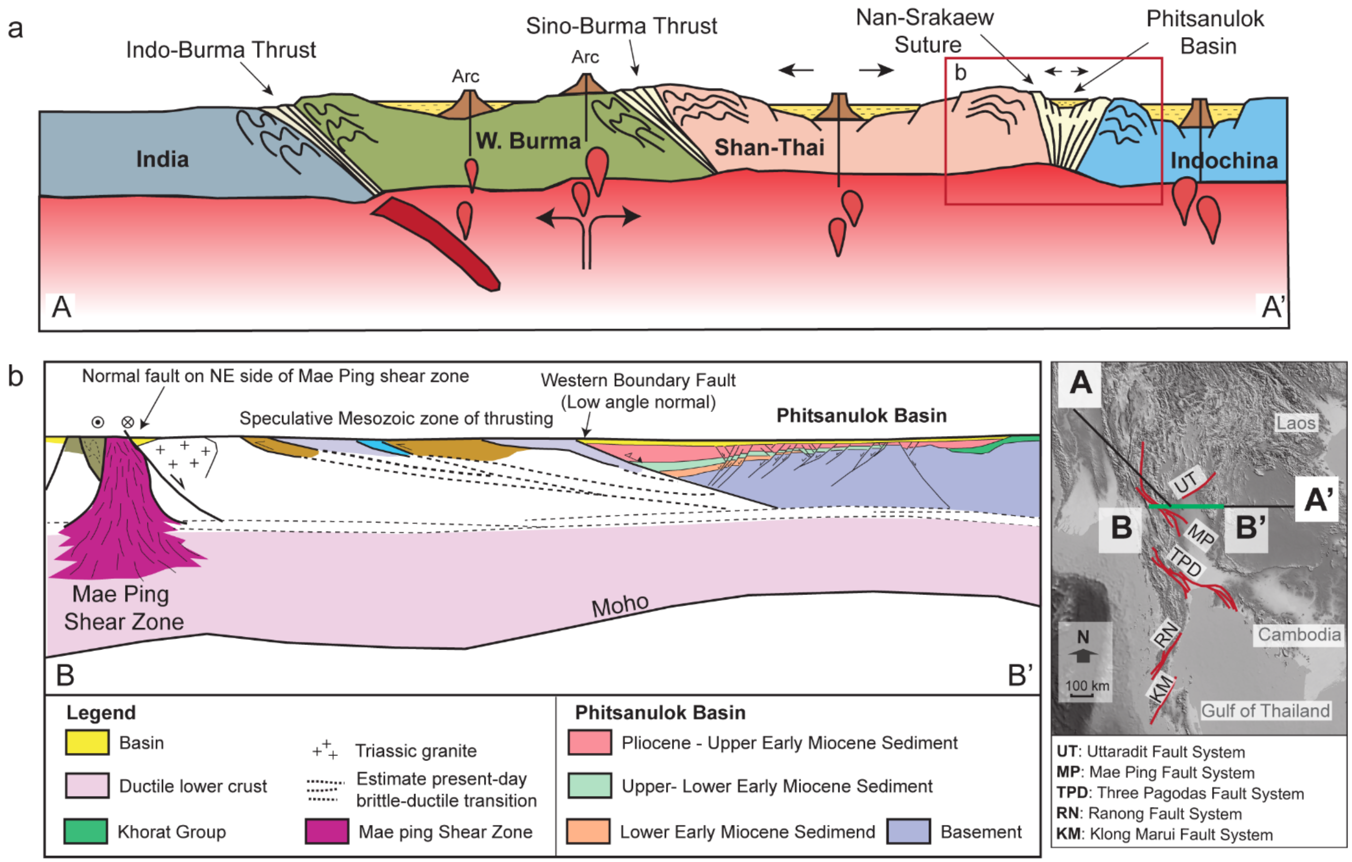

Figure 1.5 Regional cross section of the Phitsanulok basin; a) Tectonic cross section across A-A' modified from Charusiri (2002). It shows the Phitsanulok basin located on top of Nan-Srakaew Suture which was a boundary of Shan-Thai and Indochina Plate. See bottom right for location map. b) Cross section across the red rectangle in a) that shows the Mae Ping fault system and low-angle Western Boundary fault formed above deeper Mesozoic thrusts (modified from Morley *et al*., 2011a).

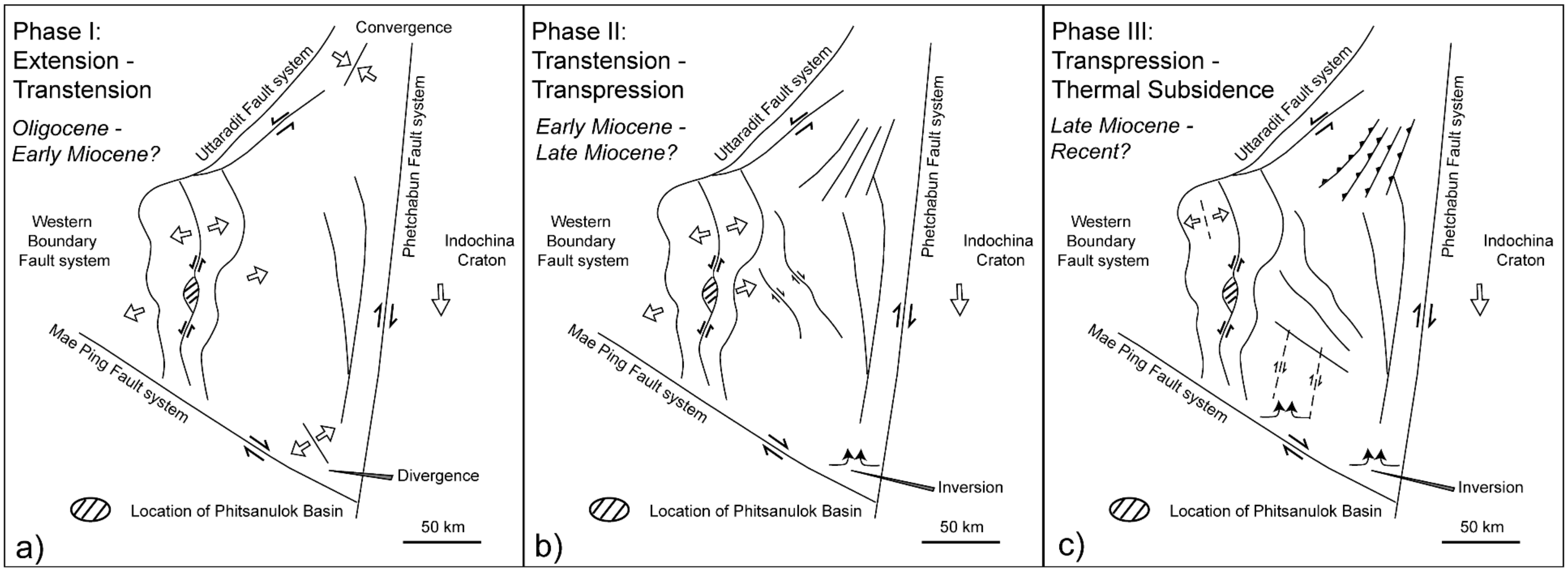

Figure 1.6 Phitsanulok basin tectonic evolution modified from Thai Shell Exploration and Production Co.Ltd (1988). a) Evolution phase I associated with extensional to transtensional deformation. In this stage the Phitsanulok basin was opened in the E-W direction and created N-S trending faults. b) Tectonic phase II associated with transtensional – transpressional deformation. In this stage the Phitsanulok basin was subjected to a changing stress regime due to an effect of the Mae Ping fault system and occurrence of the inversion in the southern part. c) Tectonic phase III is transpression to thermal subsidence.

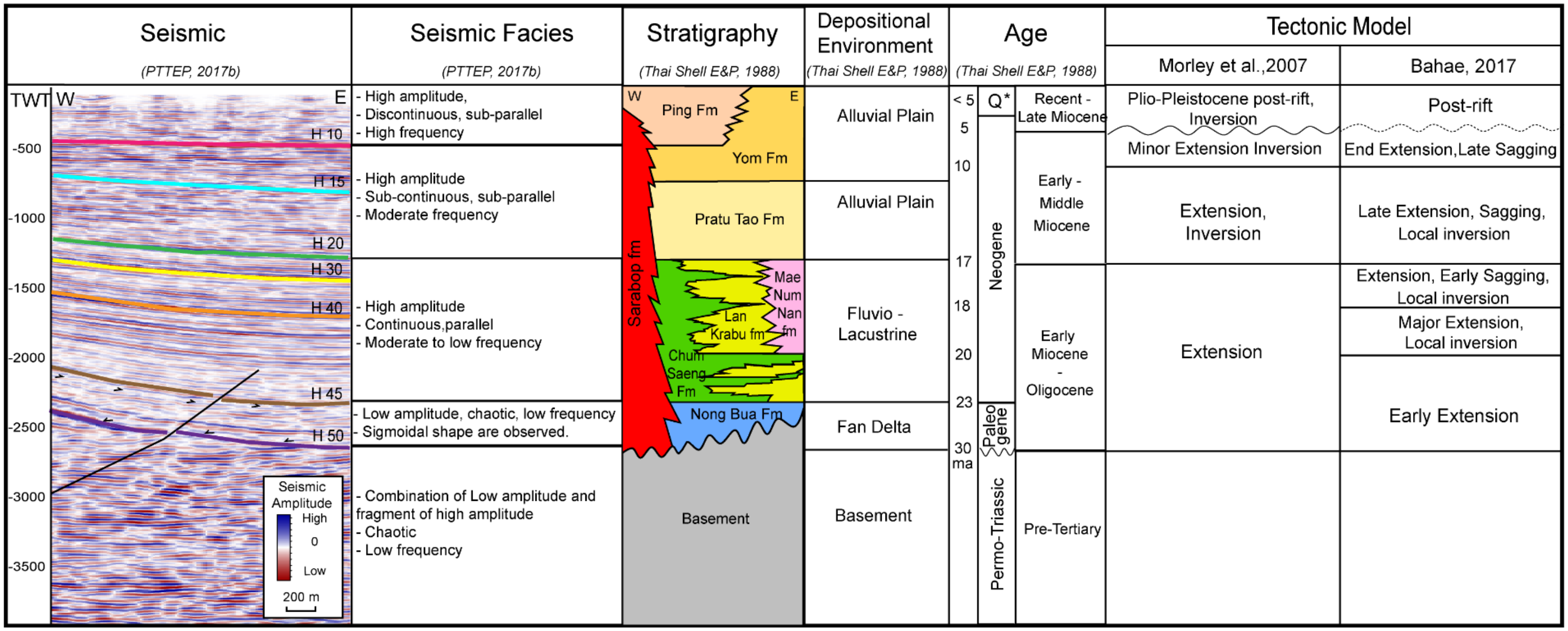

Figure 1.7 Phitsanulok basin stratigraphy and tectonic models (modified from Bahae, 2017; Morley *et al.*, 2007; PTTEP, 2017b; Thai Shell Exploration and Production Co.Ltd, 1988).*Q = Quaternary period; TWT = Two way time.

1.5. Basin structural styles

The Phitsanulok basin shows a half graben geometry that is bounded by a low angle (<30° dip) normal fault to the west which called the Western boundary fault (Figure 1.5b) (Morley, 2009). According to Morley (2009), the Western Boundary fault terminated against the ENE Uttaradit fault system (Figure 1.2). The Western Boundary fault started to move in the Oligocene period and followed the Nan-Uttaradit suture pre-existing fabric (Morley *et al*., 2011a; Morley, 2009). The influence of Mae Ping fault system and Nan-Uttaradit caused the Western Boundary fault to be a normal low angle fault as showed in Figure 1.5 b (Charusiri and Pum-Im, 2009; Morley *et al*., 2011a; Morley, 2009). Other rift basin with low-angle normal faults in Thailand are shown by the yellow polygons in Figure 1.2. Some basins in Thailand including the Chiang Mai basin are associated with metamorphic core complexes; however, the Phitsanulok basin Western Boundary fault is not associated with a metamorphic core complex (Morley, 2009). Instead, it has been speculated that the low-angle of the Western Boundary fault could be the result of reactivating a deeper, Mesozoic-age thrust belt within the basement (Figure 1.5b) (Morley et al., 2011a).

Details of previously recognized structural styles within the Phitsanulok basin are illustrated in Figure 1.8 using seismic cross sections. It has been recognized that the southern and southeastern parts of the Phitsanulok basin show inversion features that are recorded by erosional surfaces (Figure 1.8a) (Bahae, 2017; Morley, 2007). Linked normal faults with two major fault azimuths were observed in the northeast area as shown in Figure 1.8a (Morley, 2007). Details on key structural features are illustrated in Figure 1.8 seismic cross sections. To the north, the seismic transect shows a conjugate set of normal fault arrays of synthetic and antithetic normal faults (Figure 1.8b). The southern area shows a different structural style with obviously folded strata and erosional unconformity surfaces, as shown by the yellow and orange horizons in Figure 18c. Based on the seismic stratigraphy shown in Figure 1.7, these unconformities would be Early Miocene in age.

1.6. Thesis aims

The broad theme of this thesis is the quantitative structural characterization of complex fault systems at the Phitsanulok basin, onshore Thailand, and for inverted pull-apart basin sandbox analog models.

The following studies will be undertaken:

Study 1: Phitsanulok basin's tectonostratigraphic analysis

In Chapter 2, a tectonostratigraphic analysis across a large swath of the Phitsanulok basin is presented from petroleum industry 2D and 3D seismic. A 3D geological model of interpreted seismic horizons and faults is produced from interpreted faults and four interpreted main horizons: a) top of Pliocene, b) top of Upper Early Miocene, c) top of Lower Early Miocene, and d) top of Oligocene (Base syn-rift) were interpreted. The Phitsanulok basin is structurally characterized to define structural domains within the Phitsanulok basin. We then place these domains within the regional tectonic context. Possible hydrocarbon implications of our structural model are invested by comparing against play type distribution maps and hydrocarbon production data supplied by PTTEP.

Study 2: Sandbox model analysis

In Chapter 3, a 3D analysis of three previously-existing but uninterpreted sandbox models of pull-apart basins is undertaken to characterize the internal geometry of inverted pull-apart basins (i.e. formed during strike-slip fault slip-sense reversal), which occur in Thailand and SE Asia (see Ch. 3). To accomplish this analysis, a new 3D sandbox reconstruction method is developed using Petrel software (see Appendix). The inverted pull-apart basin sandbox models results are then briefly compared against published inverted rift basin models to identify common structural styles. Here we note that past studies have interpreted the Phitsanulok basin as a pull-apart basin (Charusiri and Pum-Im, 2009; Polachan, 1989) but it is generally agreed that the basin is more likely to be a complex rifted basin, not a strike-slip basin (Bal *et al*., 1992; Flint *et al*., 1988; Morley *et al*., 2011a; Morley *et al*., 2001). As such, the results of Study 2 are not intended for application to the Phitsanulok basin, but rather, for the analysis of complex structures formed in sandbox model strike-slip basins, and for sandbox model method development.

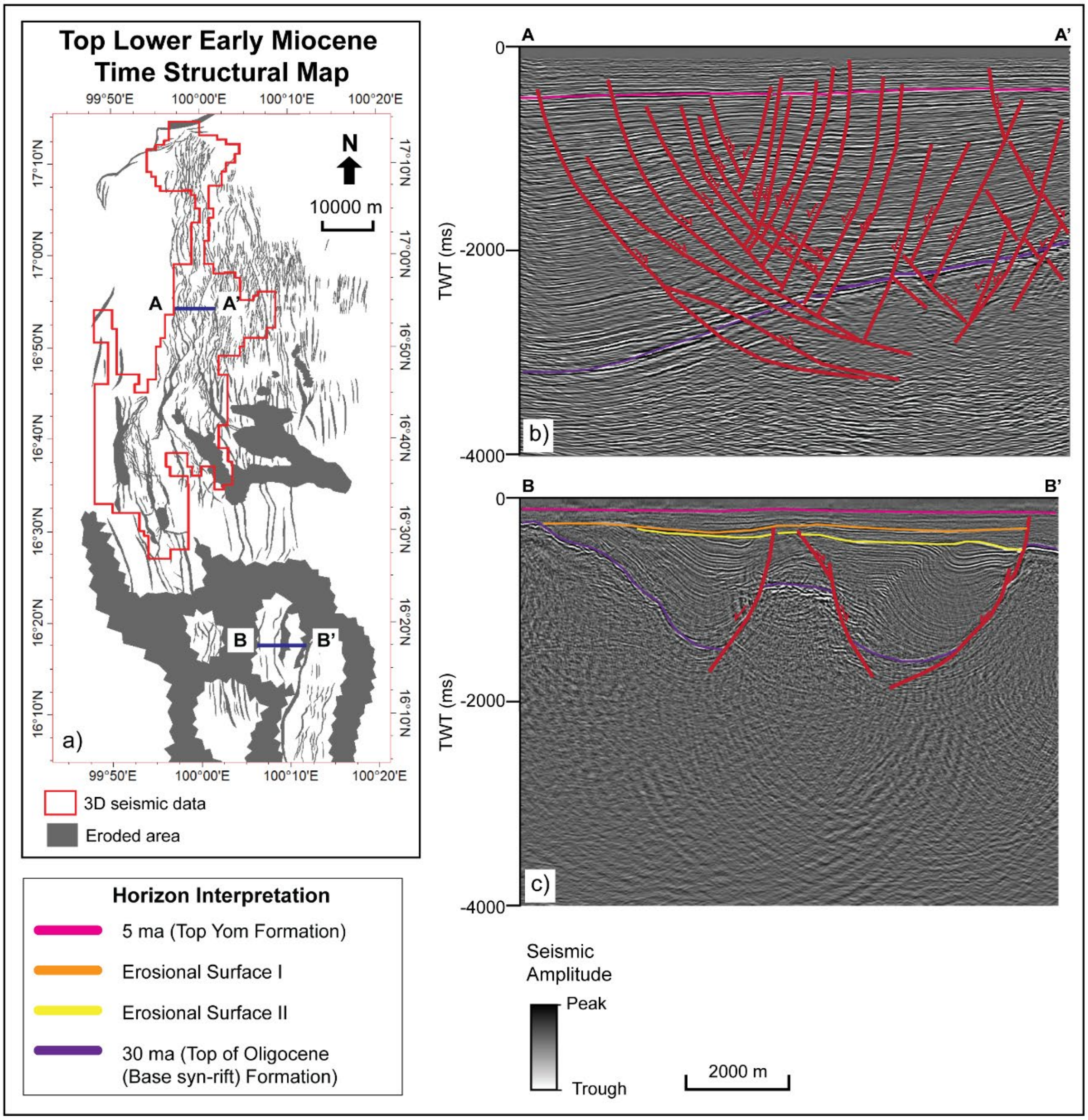

Figure 1.8 a) Fault mapping of the Lower Early Miocene time structural map modified from PTTEP (2015) showing seismic cross section locations for b) and c). Seismic cross-sections showing structural styles in the a) northern Phitsanulok basin (A-A') and b) south (B-B'). The fault and horizon interpretations are showed in the seismic profile. TWT = Two-way time

Chapter 2 Phitsanulok Basin

2.1. Data and methodology

2.1.1.Seismic data

The Phitsanulok basin architecture was interpreted from 2D seismic lines and 3D seismic volumes that were provided by PTT Exploration and Production Public Company Limited (Figure 2.1). This study involved approximately 640 2D seismic lines that covered approximately 6,000 km^2 and a 3D merge seismic cube that covered approximately 1326 km^2 within the PTTEP concession area. The seismic data cover a large swath of the Phitsanulok basin (Figure 2.1) and are appropriate for constructing a comprehensive geological model of the Phitsanulok basin. A project database was set up using Petrel software to enable seismic interpretation and to construct a 3D structural model.

2.1.2.Seismic interpretation and 3D structural model

To analyze the structure and tectonostratigraphy of the Phitsanulok basin, faults and horizons interpretation were performed based on the PTTEP 2D and 3D seismic data. Petrel seismic software was used. A total of 4 horizons and 115 faults were interpreted within the basin (Figure 2.2). The four picked horizons encompassed the main phases of tectonics (Figure 1.7): Top of the Pliocene, Top of the Upper Early Miocene, Top of the Lower Early Miocene, and Top of the Oligocene (Base syn-rift). The horizons were picked according to the PTTEP seismic facies presented in the Figure 1.7. According to PTTEP (2017b), the Top of the Pliocene was represented by sub parallel, discontinuity, moderate to low amplitude reflectors, and high to moderate frequency seismic reflectors. The Top of the Pliocene sequence was bounded by strong negative amplitude at the upper interface and unconformity at the lower interface. The Top of the Upper and Lower Early Miocene were categorized to be the same package by PTTEP (2017b). This package showed sub-parallel, continuous, high to moderate amplitude, and low frequency seismic reflectors. This package was bounded by an unconformity at the top, and high amplitude of the Oligoene (Base syn-rift). In this study the Upper and Lower Miocene was separated by a strong seismic reflector at the top of the Lower Early Miocene. The Basement (i.e. Pre-Tertiary) showed a chaotic pattern with a combination of fragment of high amplitude, and low frequency reflectors. The four horizons were input together with the picked fault framework to form a self-consistent geological model. Fault dip angles, fault throws, and fault azimuths were analyzed based on the interpreted 3D structural framework.

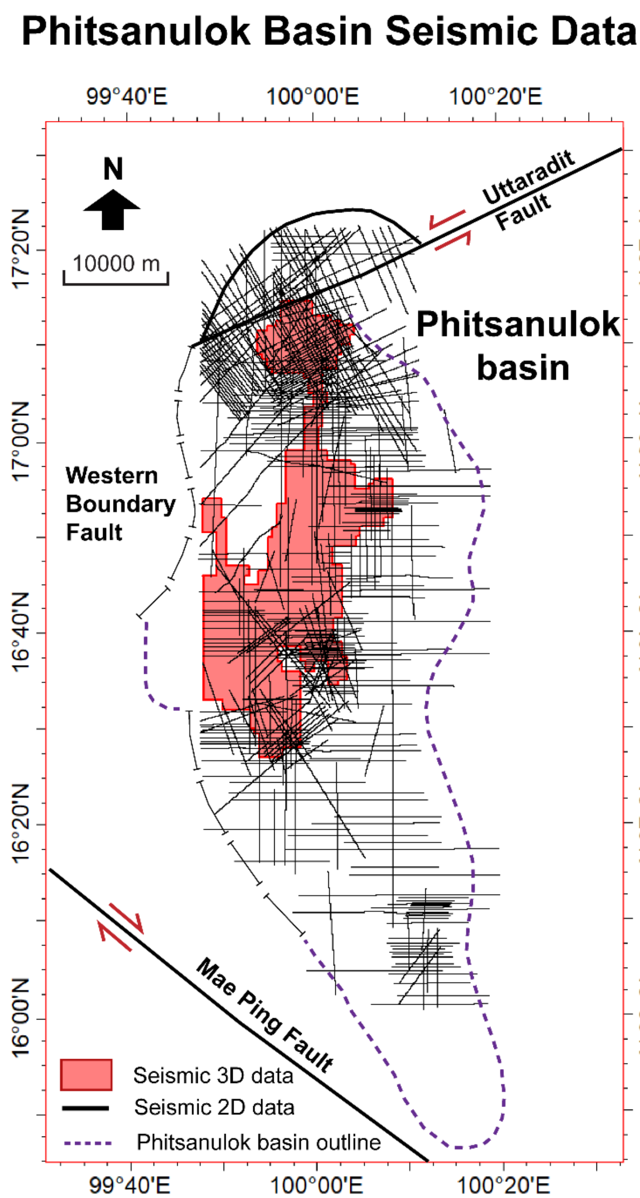

Figure 2.1 Seismic 2D and 3D data provided by PTT Exploration and Production Public Company Limited. The data cover a large swath of the Phitsanulok basin, as shown by the dashed outline.

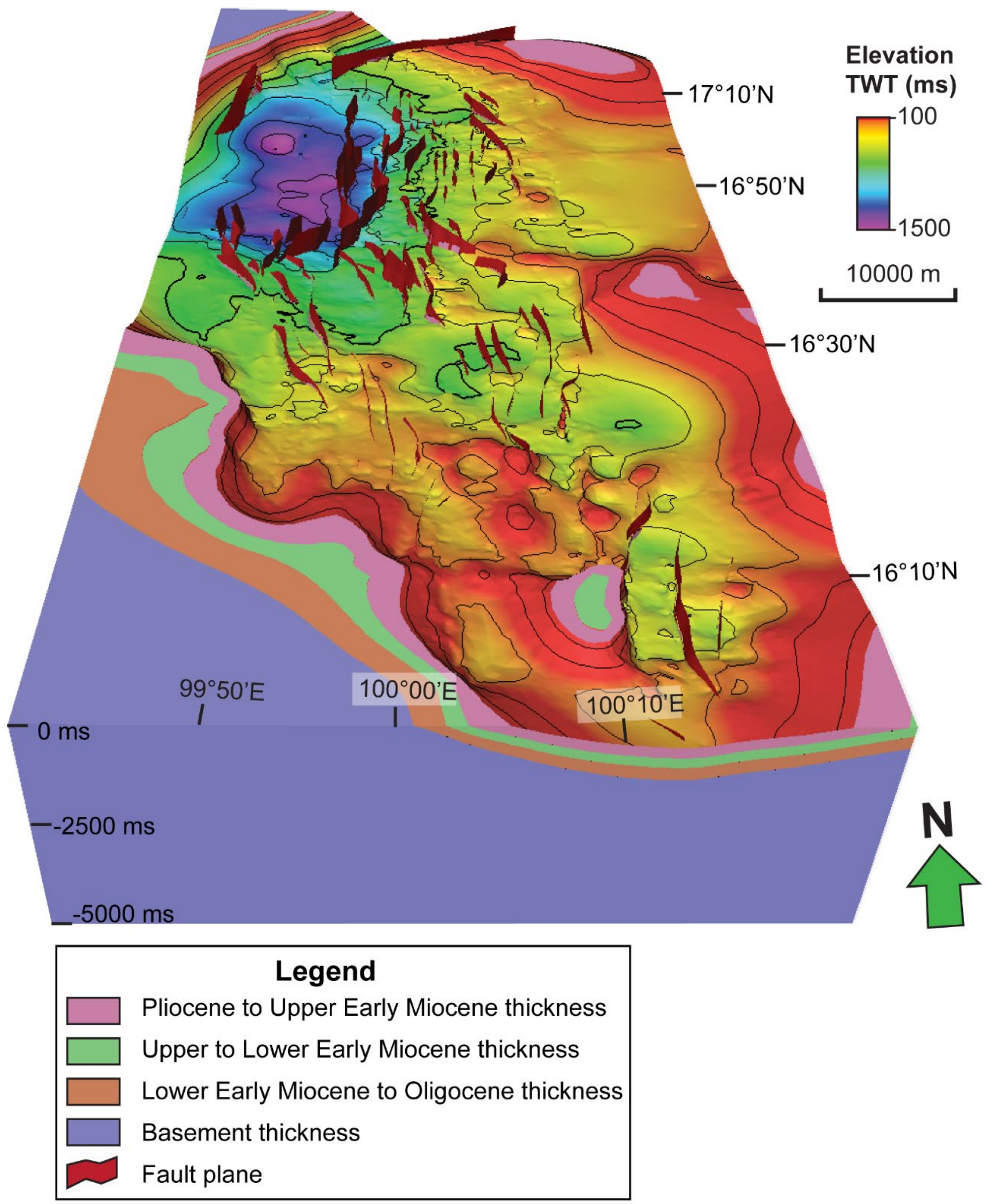

Figure 2.2 3D view of the Phitsanulok basin structural framework in this study, which was constructed from 115 faults and 4 interpreted seismic horizons.

2.2. Results

2.2.1.Phitsanulok basin tectonostratigraphy

Regional seismic transects

To characterize the Phitsanulok basin regional structure, nine E-W seismic cross sections line 1 to line 9 are presented in Figure 2.3. Detailed structures are shown in Figure 2.4. In the northern area, from west to east, the Phitsanulok basin is bounded by an east-dipping, low angle normal fault called the Western Boundary fault (WBF) (Morley, 2009), followed by a wide (25 km), relatively unfaulted area called the Sukhothai depression, and finally, deformed by arrays of closely-spaced, low-displacement conjugate normal faults (Figure 2.3 Lines 2 -5). The thickness of sediments within the Sukhothai depression is approximately 8 km (Flint *et al*., 1988). In the northeast area (Figure 2.3 Lines 1-4) showed conjugate, cross cutting normal fault arrays. This fault pattern is usually associated with crestal collapse faults above a listric normal fault; the specific fault styles are controlled by the underlying listric fault profile (McClay and Ellis, 1987). Hence, the northeast area fault pattern was possibly created to response the low-angle normal fault in the northwest.

In the southwestern area, the Western Boundary fault is present but appears less well imaged; the basin floor is clearly uplifted relative to the northern area (Figure 2.3 Lines 5-9). Here the Western Boundary fault hanging wall is also deformed by an array of curved conjugate synthetic and antithetic faults (e.g., Figure 23 Line 5). In detail, the southern area shows erosion and, in some cases, folding of late Miocene and older strata under a regional unconformity (orange horizon) (Figure 2.4b and c). In contrast, the northern area is relatively free from obvious erosion and folding (Figure 2.4a). In both areas, faults do not significantly penetrate above the regional unconformity (Figure 2.4). The age of the regional conformity is not easily established from the continental stratigraphy but is approximately Late Miocene to Pliocene in age (Bahae, 2017).

In the central area, the basin is deformed by tilted fault blocks as in Figure 2.3 Line 5. In both the eastern and southern area erosional surfaces were observed (Figure 2.3 Lines 4, 6-9). In detail, seismic profile Figure 2.4b showed an erosional surface (yellow horizon) which could be observed in the eastern area of the Phitsanulok basin (Figure 2.4b). Seismic profile c showed erosional surfaces (dark yellow and bright yellow horizons) and folded strata in the southern area of the Phitsanulok basin (Figure 2.4c). The unconformities often eroded across the 10 ma sediment layer (purple horizon) (Figure 2.4b, c). The sediment thickness in the southern area is conspicuously thinner compared to the northern area (Figure 2.3). The variable thickness of the 10 ma horizon (light purple) to Oligocene (Base syn-rift) horizon (dark blue) was clearly shown in both Figure 2.3 and 2.4.

Time structure maps

A time structure map of our four main interpreted horizons; the top of Pliocene, Upper Early Miocene, Lower Early Miocene, and Oligocene (Base syn-rift), are shown (Figure 2.5). The Western Boundary fault and Uttaradit fault are shown on all maps (Figure 2.5 a-d). All maps indicated a deep area within the Phitsanulok basin in the northwest area, the Sukhothai depression (Figure 2.5 a-d). Within the Sukhothai depression, the deepest zone is around 3800 ms TWT (two-way time) as shown on the Oligocene (Base syn-rift) map (Figure 2.5d). The southern limit of the Sukhothai depression ends abruptly around 16°45’N latitudes (Figure 2.5). High intensity erosion can be observed in the southern area from the mapped subcrop unconformities (i.e. the wavy outer boundaries of the mapped areas) at the Upper Early Miocene and Lower Early Miocene stratigraphic levels (Figure 2.5b and c).

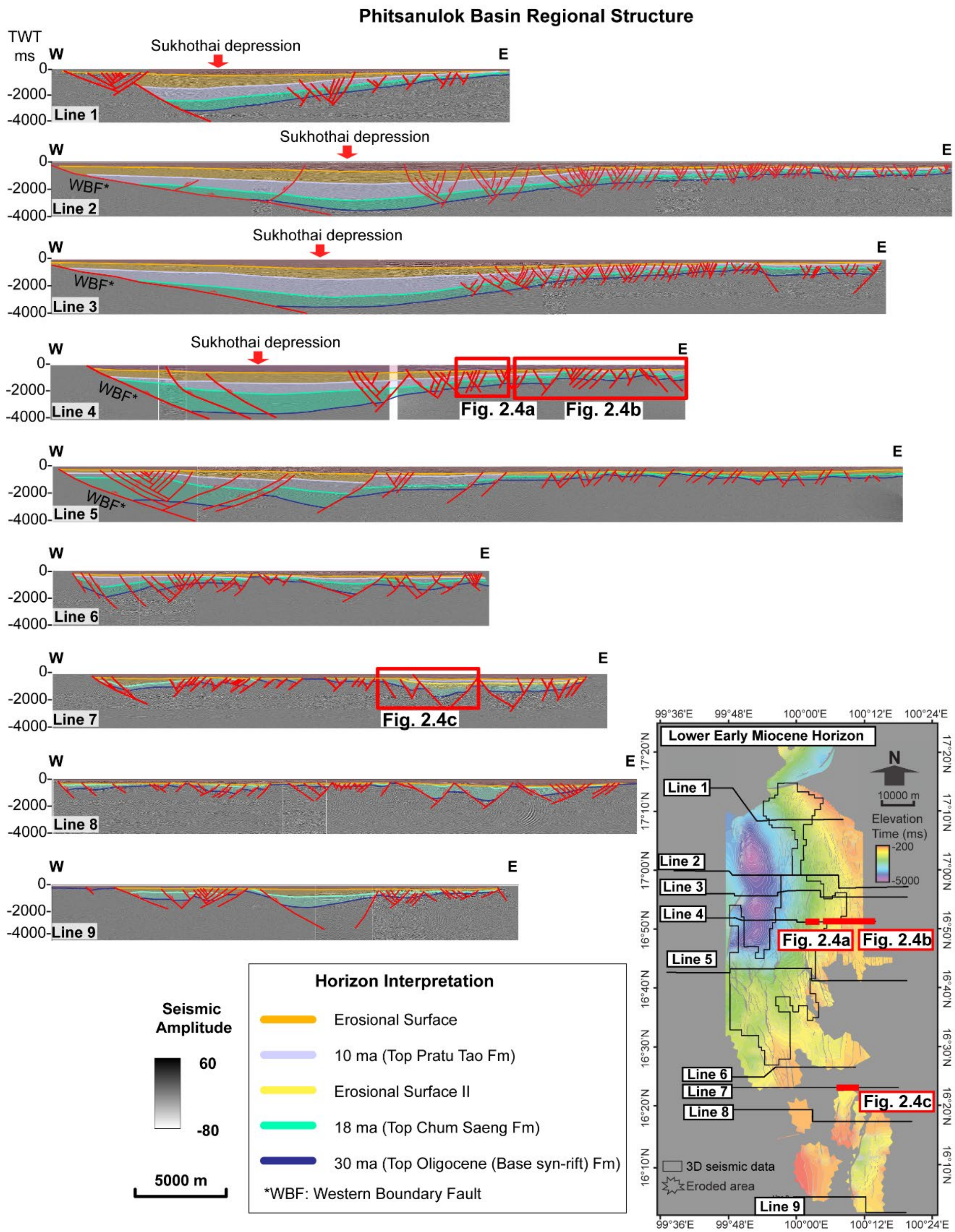

Figure 2.3 Regional W-E seismic cross sections across the Phitsanulok basin showing key horizons and faults. The 3D seismic data is outlined by the black polygon in the index map. *WBF = Western Boundary fault, TWT = Two-way time.

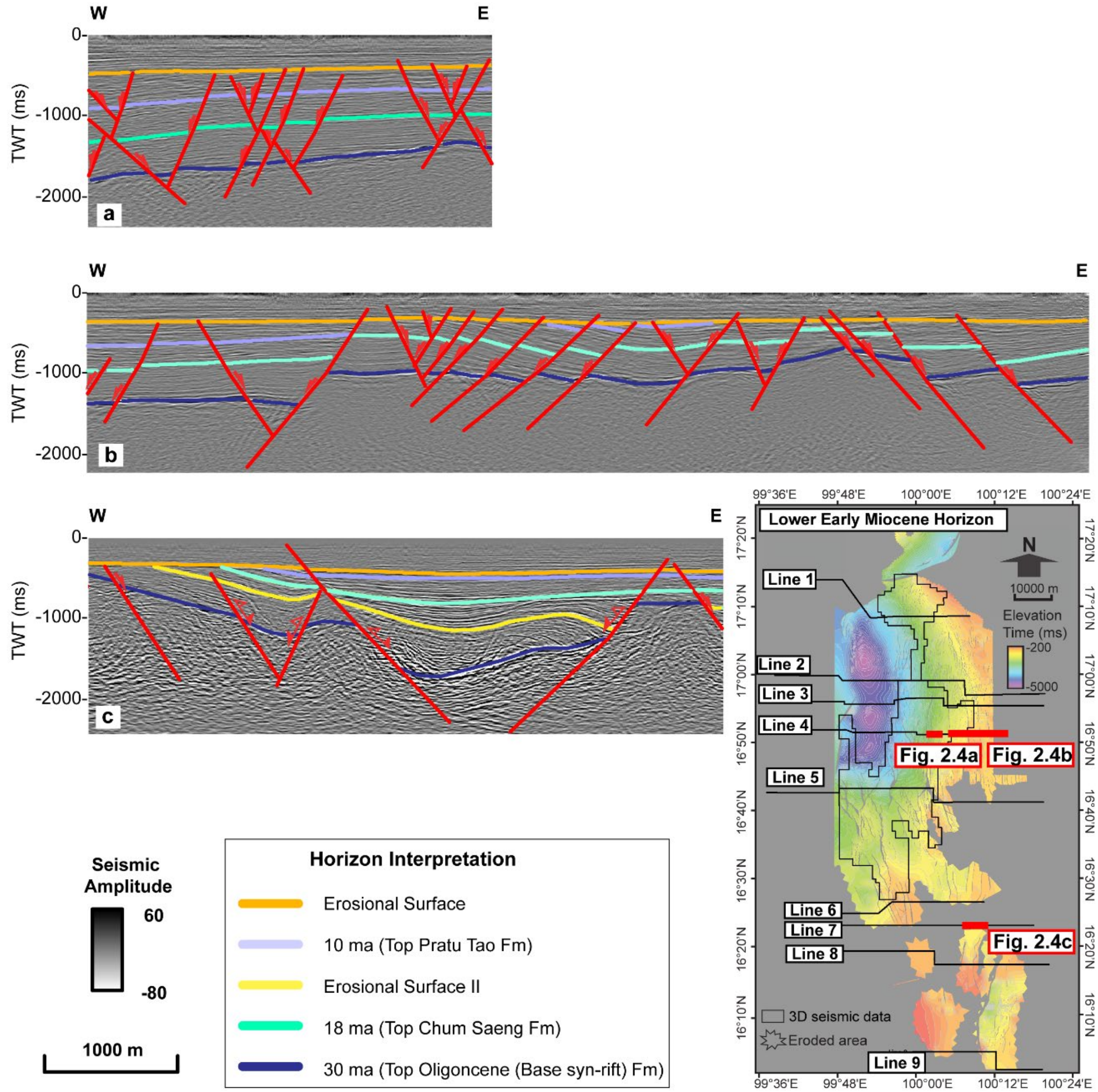

Figure 2.4 Detailed Phitsanulok basin structural geometries within the red boxes shown in Figure 4. Transects 'a' shows the northern extensional regime. Transect 'b' and 'c' show erosional unconformity within the eastern and southern area. The 3D seismic data is outlined by the black polygon in the index map. TWT = Two-way time

Isochron thickness maps

Isochron maps were calculated to show thickness changes across the Phitsanulok basin (Figure 2.6 – 2.7). The four isochron maps measured thickness in two-way time between the: a) Pliocene to Oligocene (Base syn-rift); b) the Lower Early Miocene to Oligocene (Base syn-rift); c) the Upper Early Miocene to Lower Miocene; and, d) the Pliocene to Upper Early Miocene strata (Figure 2.7). To show the overall syn-rift architecture of the Phitsanulok basin (i.e. prior to the post-rift phase; Figure 1.7), a 'Pliocene to Oligocene (Base syn-rift)' isochron thickness map was created as in Figure 2.6. The map clearly shows the Sukhothai depression from the thickened area in the north-west Phitsanulok basin (Figure 2.6). The southern area showed thin sediment thicknesses (<500 ms) (Figure 2.6).

Individual isochron thickness maps are shown in Figure 2.7. The isochron thickness maps for the stratigraphically-lower Lower Early Miocene to Oligocene (base syn-rift) and Upper Early Miocene to Lower Early Miocene thickness map (Figure 2.7b, c) generally show thickened strata along the length of the westernmost Phitsanulok basin, which is consistent with subsidence along the Western Boundary fault system. South of 16°50'N some thinned areas appear near the Western Boundary fault (Figure 2.7b, c). The areas south of 16°25'N are highly thinned to non-existent due to erosion (i.e. wavy lines along the outermost mapped area) (Figure 2.7b, c). Stratigraphically higher, the Pliocene to Upper Early Miocene thickness map (Figure 2.7a) shows a similar thickening near the Western Boundary fault in the northern region only; an abrupt thinning of strata occurred south of 16°50'N. Finally, similar to the lower stratigraphic levels the areas south of 16°25'N are highly thinned to non-existent due to erosion (Figure 2.7a).

2.2.2. Phitsanulok basin fault geometries

Fault mapping

Figure 2.8a to d showed fault maps across the a) Pliocene; b) Upper Early Miocene; c) Lower Early Miocene; and d) Oligocene (Base syn-rift). These four fault maps show relative similar fault orientations across stratigraphic levels (Figure 2.8). To improve the precision of the fault mapping, the variance attribute, which is a similarity measurement attribute (Chopra and Marfurt, 2007) was applied in the mapping workflow (Figure 2.9a-d). The variance attribute maps which were extracted along horizon were illustrated in Figure 2.9a to d; a) Pliocene, b) Upper Early Miocene, c) Lower Early Miocene, and d) Oligocene (Base syn-rift) horizon respectively. The variance was colored by dark reddish color, while, the white regions represent areas with the same similarity (Figure 2.9). Fault patterns north of 16°50'N and south of 16°35'N latitudes show general N - S trends (Figure 2.8b). whereas faults between 16°50'N and 16°35'N latitudes diverge from N - S trends (i.e. both NNE-SSW and NNW-SSE) and appear hard-linked (Figure 2.8b). The most distinct break in fault patterns appears across 16°35'N latitudes. Fault azimuths will be further quantified in Section 2.2.3 below.

Phitsanulok Basin Structural Map

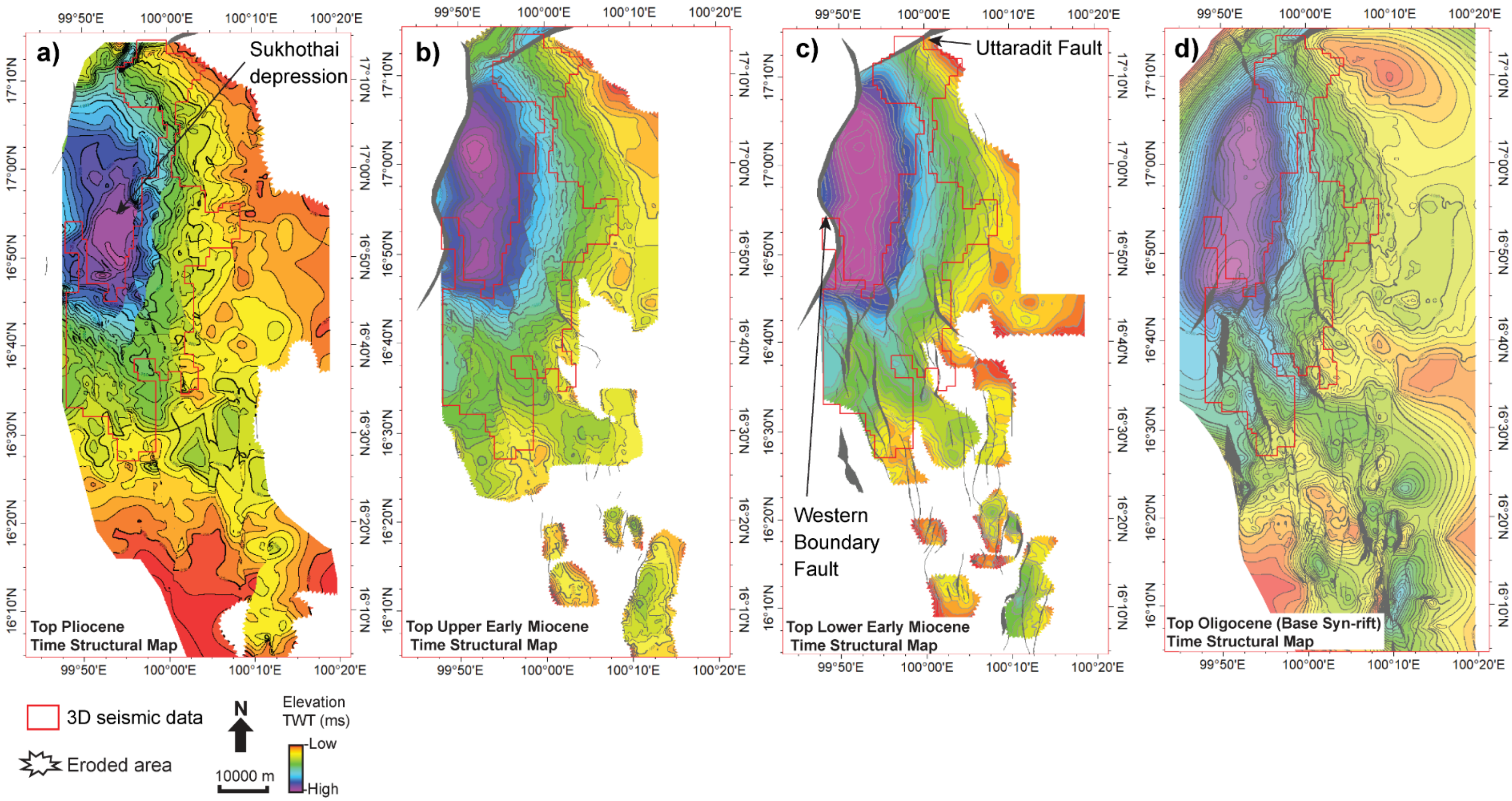

Figure 2.5 Phitsanulok basin time structural maps: a) top Pliocene; b) Upper Early Miocene; c) Lower Early Miocene; and d) Oligocene (Base syn-rift). The 3D seismic data is outlined by red polygon. Wavy edges at the map boundaries indicate erosional contacts.

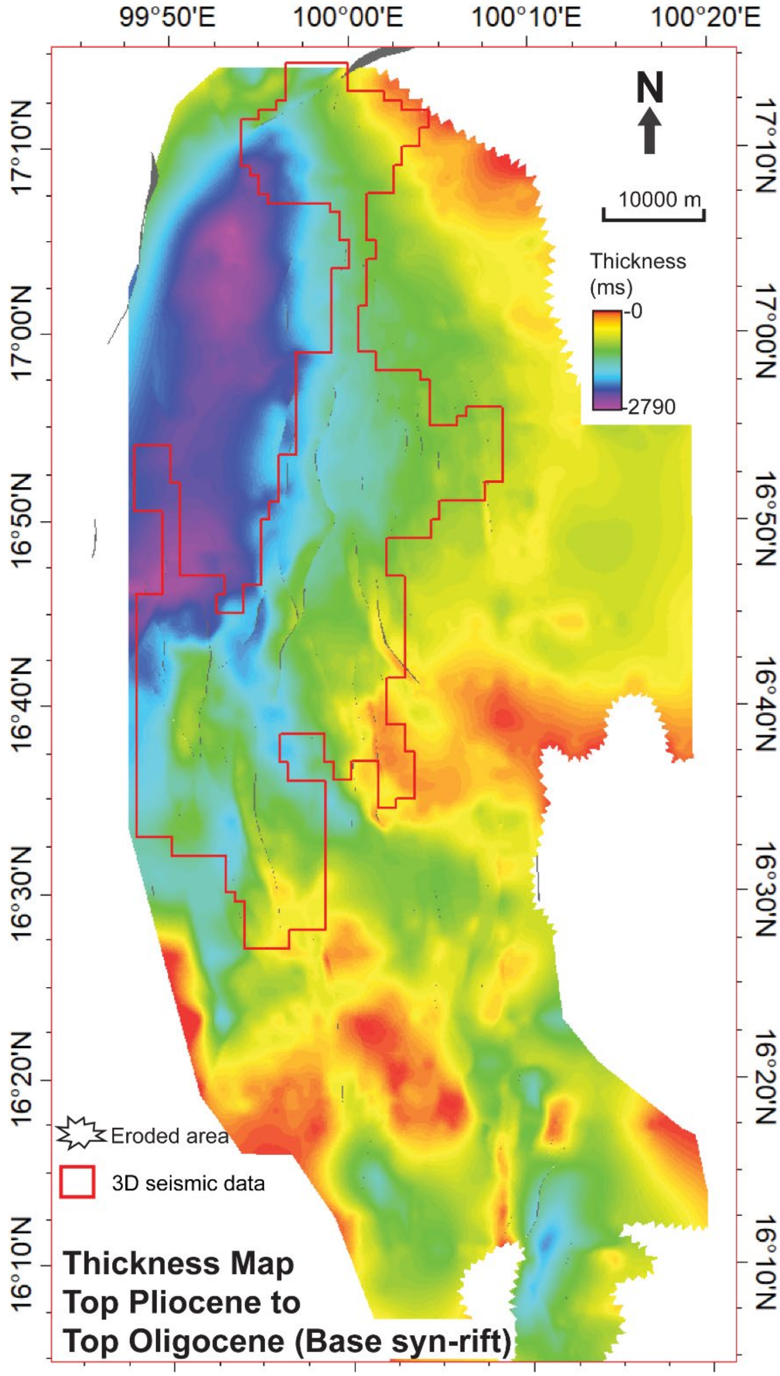

Figure 2.6 The Pliocene to Oligocene (Base syn-rift) isochron thickness map which represented the total sediment thickness of the Phitsanulok in the time domain. The purple color shows the thickest area within the Phitsanulok basin is within the north-west (i.e. Sukhothai depression). The red color shows thinned sediment layer that indicate Oligocene (Base syn-rift) highs. Wavy edges at the map boundaries indicate erosional contacts.

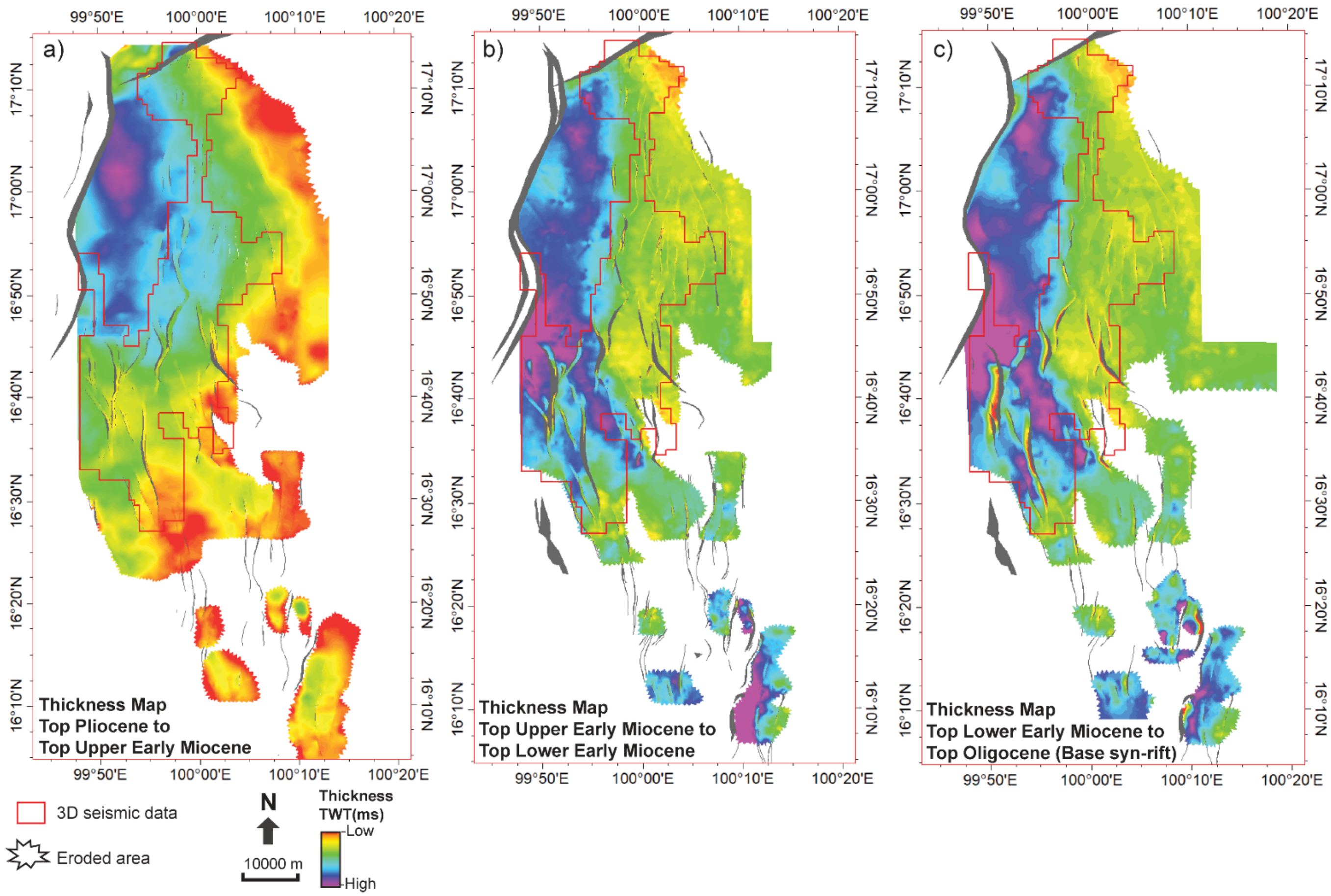

Figure 2.7 Isochron maps of a) the Pliocene to Upper Early Miocene horizon, b) the Upper Early Miocene to Lower Early Miocene and c) the Lower Early Miocene to Oligocene (Base syn-rift). At the early stages b) and c) the maps show preserved areas of thick sediments along the Western Boundary fault far to southern basin margin. In contrast, at later stages in a) the southern area is clearly thinned south of around 16°45'N and eroded to non-existent south of 16°25'N. The 3D seismic coverage is outlined by the red polygon. TWT = Two-way time. Wavy edges at the map boundaries indicate erosional contacts.

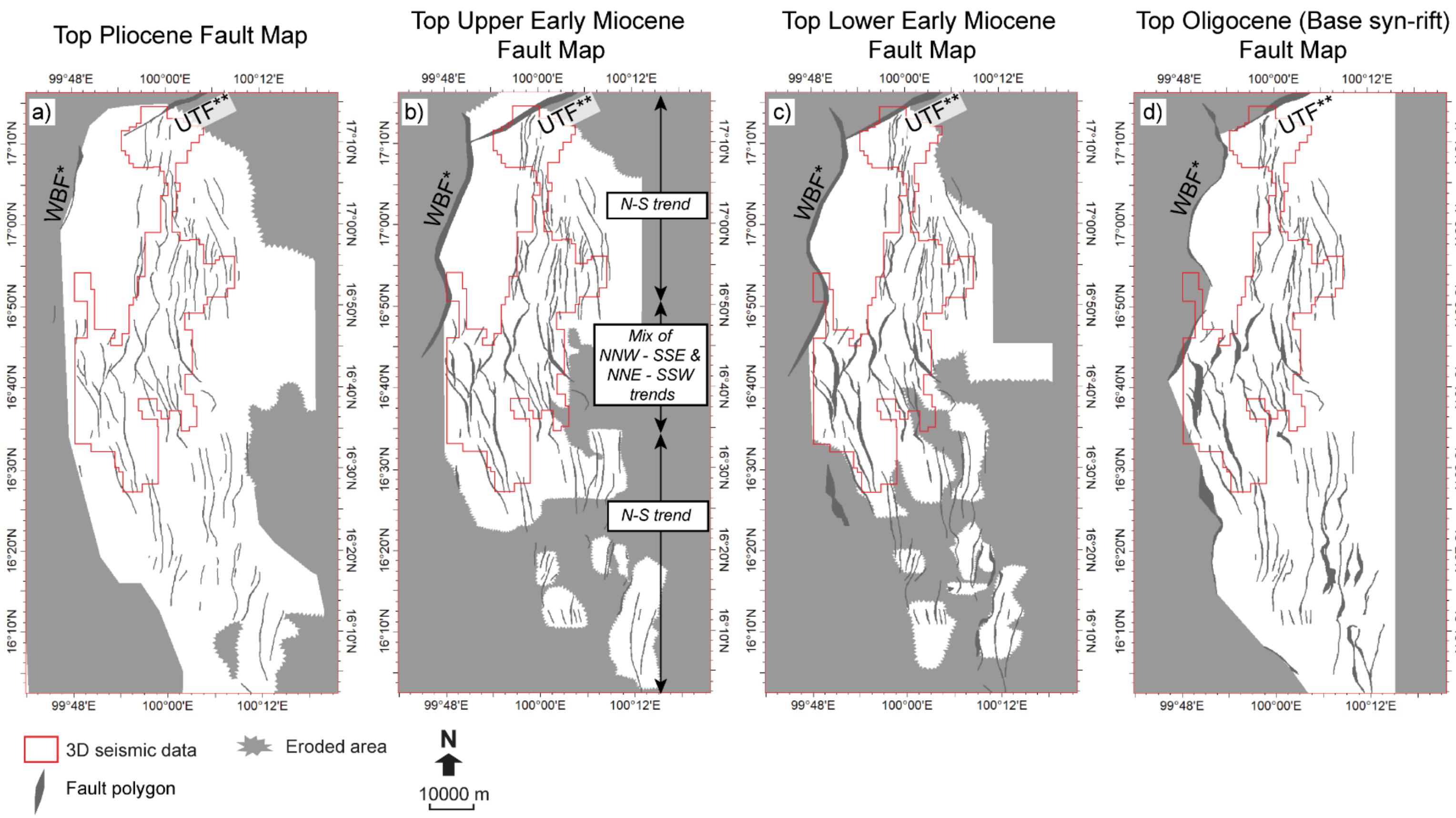

Figure 2.8 Mapped of the Phitsanulok fault patterns illustrated with outline of maximum sediment extents (white polygon): a) Pliocene (Yom formation) horizon fault map; b) Upper Early Miocene (Chum Saeng Formation) fault map; c) Lower Early Miocene (Lan Krabu L formation) horizon fault map; and d) Oligocene (Base syn-rift) horizon fault map. The 3D seismic data coverage is displayed by the red polygon. * WBF = Western Boundary fault; **UTF = Uttaradit fault. Wavy edges at the map boundaries indicate erosional contacts.

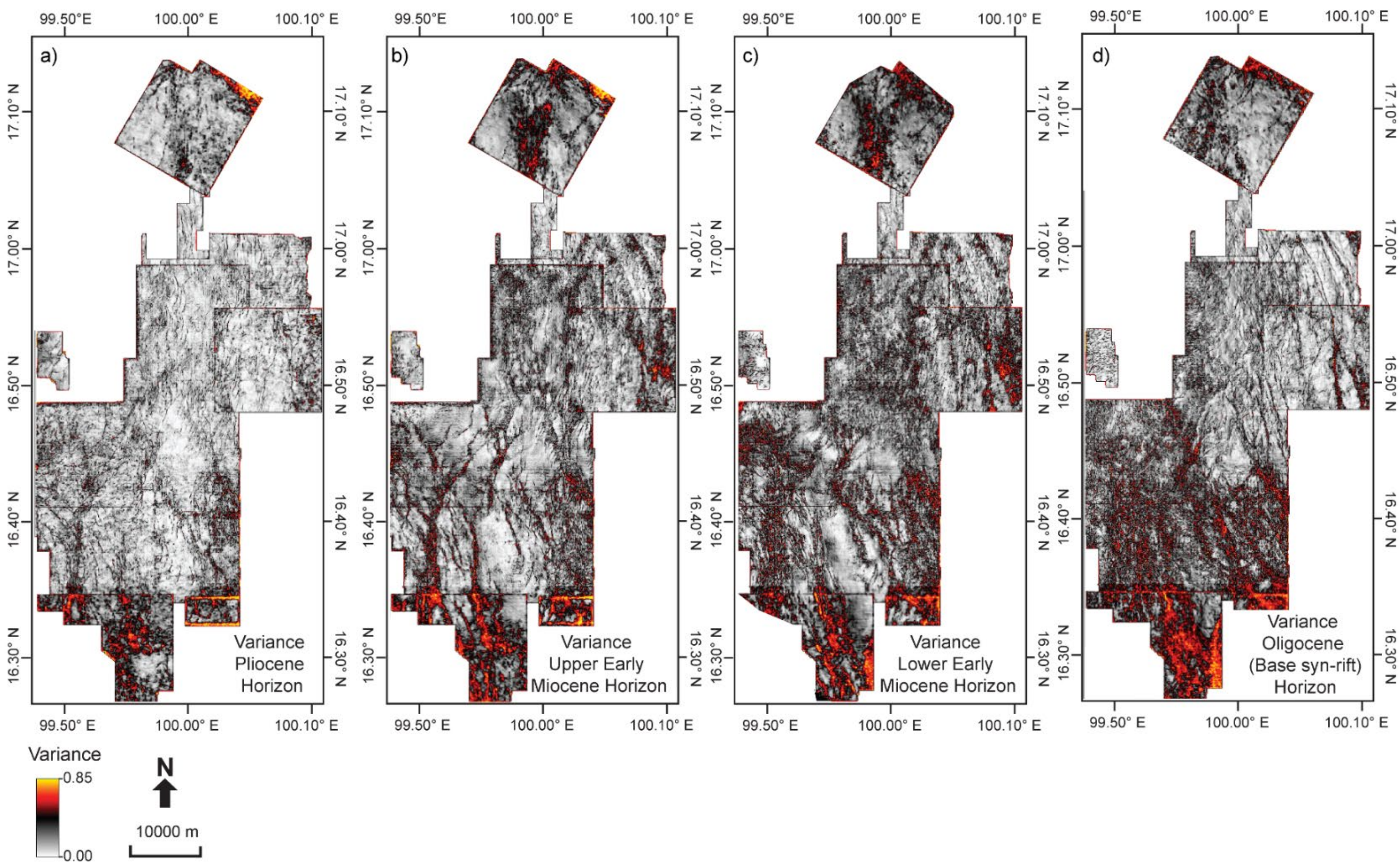

Figure 2.9 Variance attribute display along interpreted horizons: a) Top Pliocene horizon; b) Top Early Miocene horizon; c) Top Lower Early Miocene; and d) Top Oligocene (Base syn-rift) horizon. The variance maps show dark reddish colors where similarities are highly contrasted, whereas white regions represent areas of relatively equal similarity.

2.2.3. Phitsanulok basin structural analysis

Fault dip angle analysis

The results of fault dip angle analysis in the Phitsanulok basin is illustrated in Figure 2.10. Interpreted fault planes are colored red to purple by fault dip angle variations between 10° to 75° dips (Figure 2.10). Our estimated dip angles should be considered minimum values because they were measured in two-way time; in reality, fault dip angles will be steeper due to velocity increase with depth (Figure 2.11), particularly at deeper depths. However, the mapped fault dip angles in Figure 2.10 are appropriate for a relative comparison within the basin for two reasons: (1) seismic velocities do not show abrupt jumps with depth, and, (2) seismic velocities are roughly comparable from north to south (Figure 2.11).

As already seen on the seismic cross-sections (Figure 2.3), the major basin-bounding Western Boundary normal fault shows very low dip angles (10° - 30°) (Figure 2.10). The basin-bounding Uttaradit fault shows generally steep dip angles that vary between 55° - 75° (Figure 2.10). The most prominent change in fault dips occurs across 16°50'N latitudes, which divides steeper dipping normal faults to the north and shallower dipping normal faults to the south (Figure 2.10). In more detail, the areas north of 16°50'N shows fault arrays that dip greater than 45° and were generally colored blue to green in our map (Figure 2.10). The normal faults south of 16°50'N generally show an upward-steepening trajectory (i.e. listric) from 10° to 40° dips at depth and 60° to 75° dip in the shallow section. Some of the apparent 'listric' fault geometries in our two-way-time analysis can be obviously explained by seismic velocity increase with depth (Figure 2.11). However, the relative change in fault dips between the northern and southern basin across 16°50'N is robust given the relatively comparable seismic velocities between the two regions (Figure 2.11).

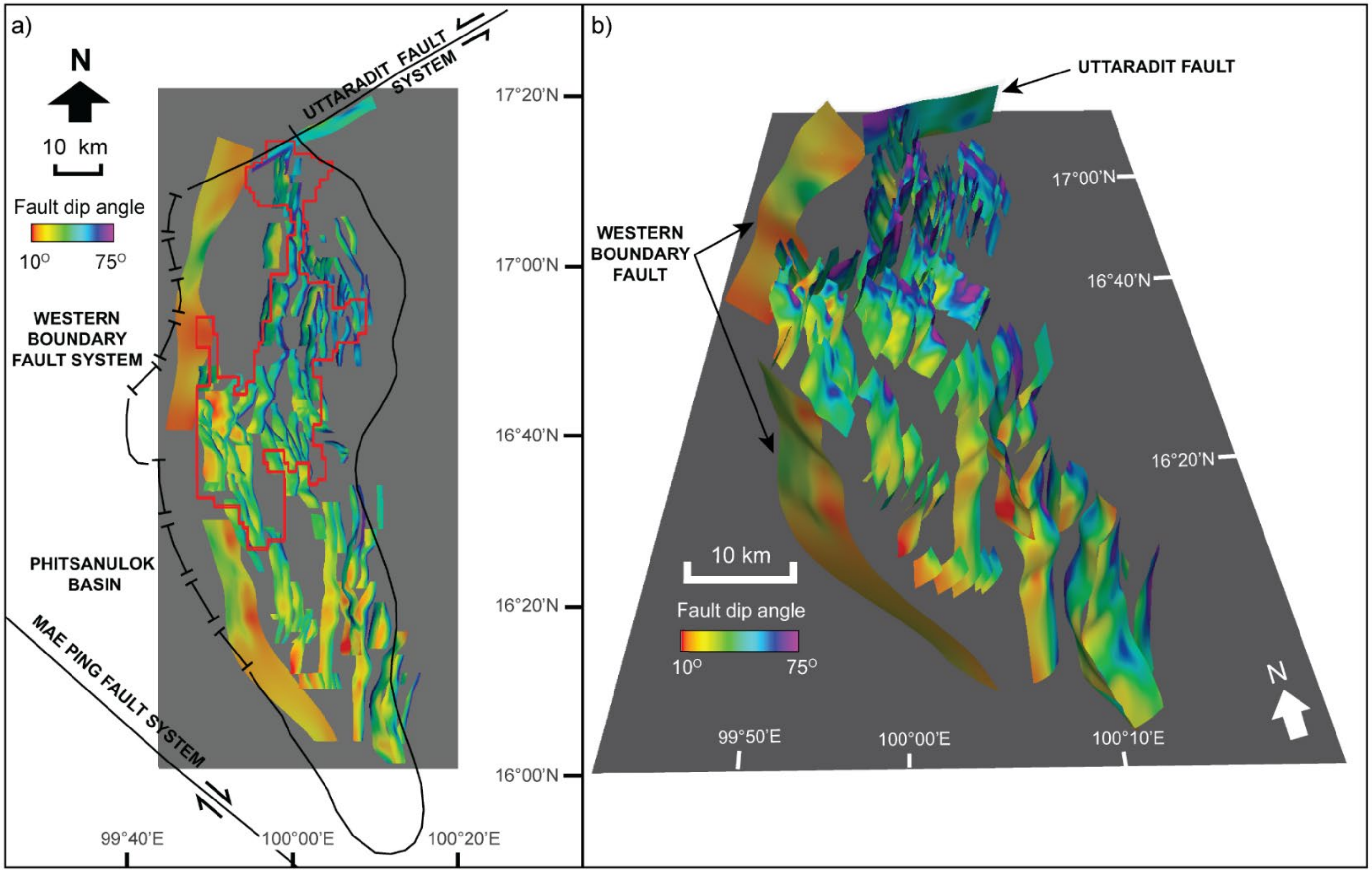

Figure 2.10 The Phitsanulok basin fault dip angle analysis. Fault planes are colored by the fault dip angle from 10° to 75° dips based on a two-way time interpretation. a) Top view of the fault dip angles; b) 3D view of the fault dip angle. The 3D seismic data coverage is outline by the red polygon. Fault patterns show relatively steeper dips to the north and gentler dips to the south. Although fault dip angles are in two-way time, Figure 2.11 shows that the contrasting fault dips between north and south are unlikely to be from regional seismic velocity changes.

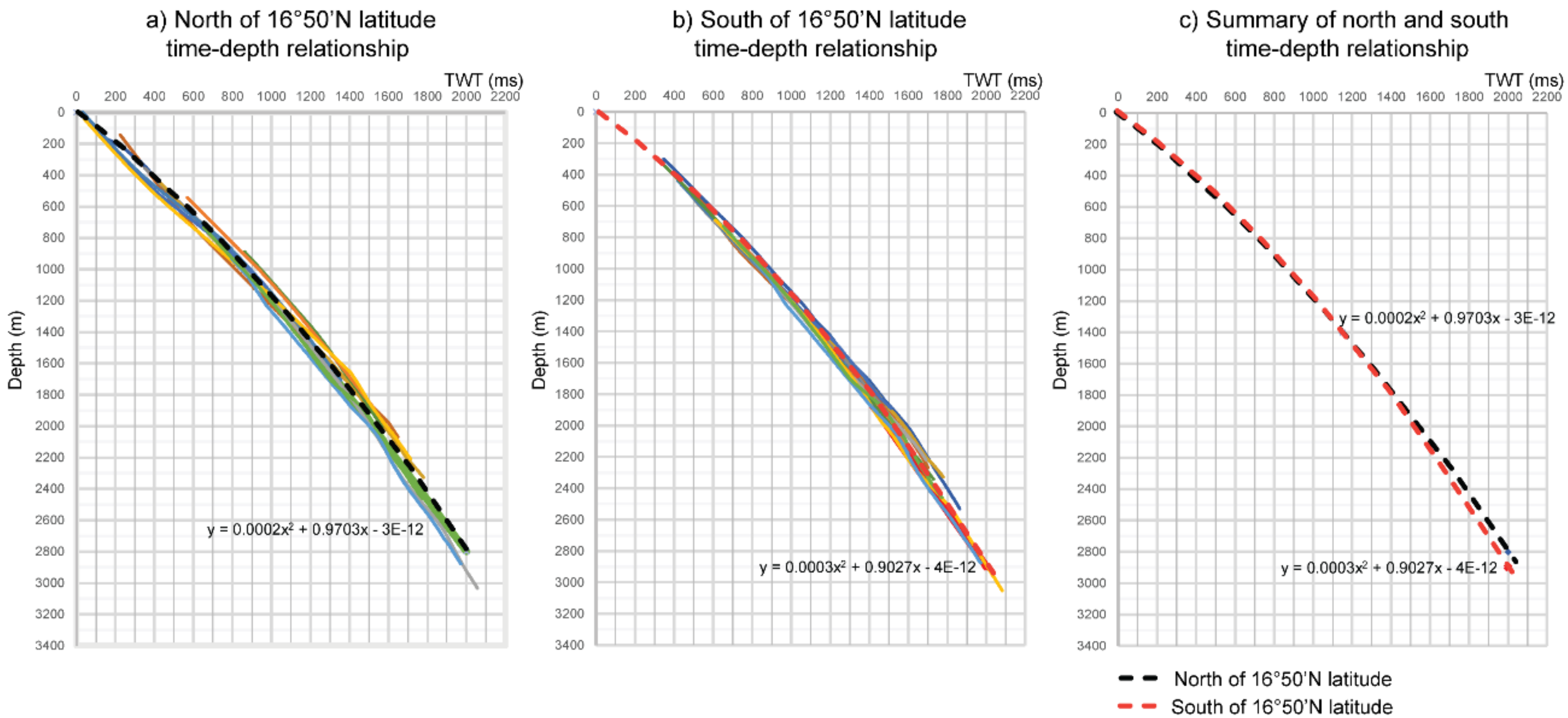

Figure 2.11 Time-depth relationship for the Phitsanulok basin based on 32 well synthetics: a) Seismic velocities north of 16°50'N latitudes, b) South of 16°50'N latitudes, and c) Summary of north and south trends modified from PTTEP (2017b). Black dash line in a) represent an average trend of North of 16°50'N latitude and red dash line in b) represent an average trend of South of 16°50'N latitude. There is not a significant separation of these two average trends when plotted it together in c). TWT = Two-way time.

Fault azimuth analysis

Fault azimuths were calculated for individual fault cutoffs across the Pliocene, Upper Early Miocene, Lower Early Miocene and Oligocene (Base syn-rift) seismic horizons and shown by latitude (Figure 2.12 to 2.15). A plot of azimuths across all four stratigraphic levels by latitude is shown in Figure 2.16 to accentuate potential trends. For all plots in Figure 2.12 to 2.16, the azimuths were incrementally sampled at every 0.1° latitude through the Phitsanulok basin and plotted in aggregate within the rose diagram in the left column; a structural map of each horizon is presented at the right side. For this study, due to the extensive seismic dataset we limited our analysis to the major faults only, which we defined as faults that cut through most or all of the stratigraphic column. Therefore, our analysis will not highlight changes in fault azimuth with stratigraphic level (e.g., Figure 2.17). These changes in fault azimuth with depth were previously shown by Morley *et al*. (2007) for shorter, vertically-discontinuous faults within the Phitsanulok basin.

In general, faults azimuths within the study area generally range from 345° to 15° (i.e. NNW-SSE to NNE-SSW) (Figure 2.16). Similar trends for observed by Morley *et al*. (2007) for Early Miocene strata within the Phitsanulok basin. Variations in fault azimuth by latitude are generally indistinguishable from our analysis (Figure 2.16). However, we note a group of fault azimuths between 17°00'N to 16°30'N that show only limited NNE-SSW trends relative to other latitudes (Figure 2.16). Therefore, it may be possible to weakly distinguish three groups of fault azimuths (a, b and c in Figure 2.16). However, the most robust observation is that the fault azimuths are generally aligned N - S (Figure 2.16), which is most closely aligned with the basin-bounding Western Boundary fault and dissimilar to the basin-bounding Uttaradit fault.

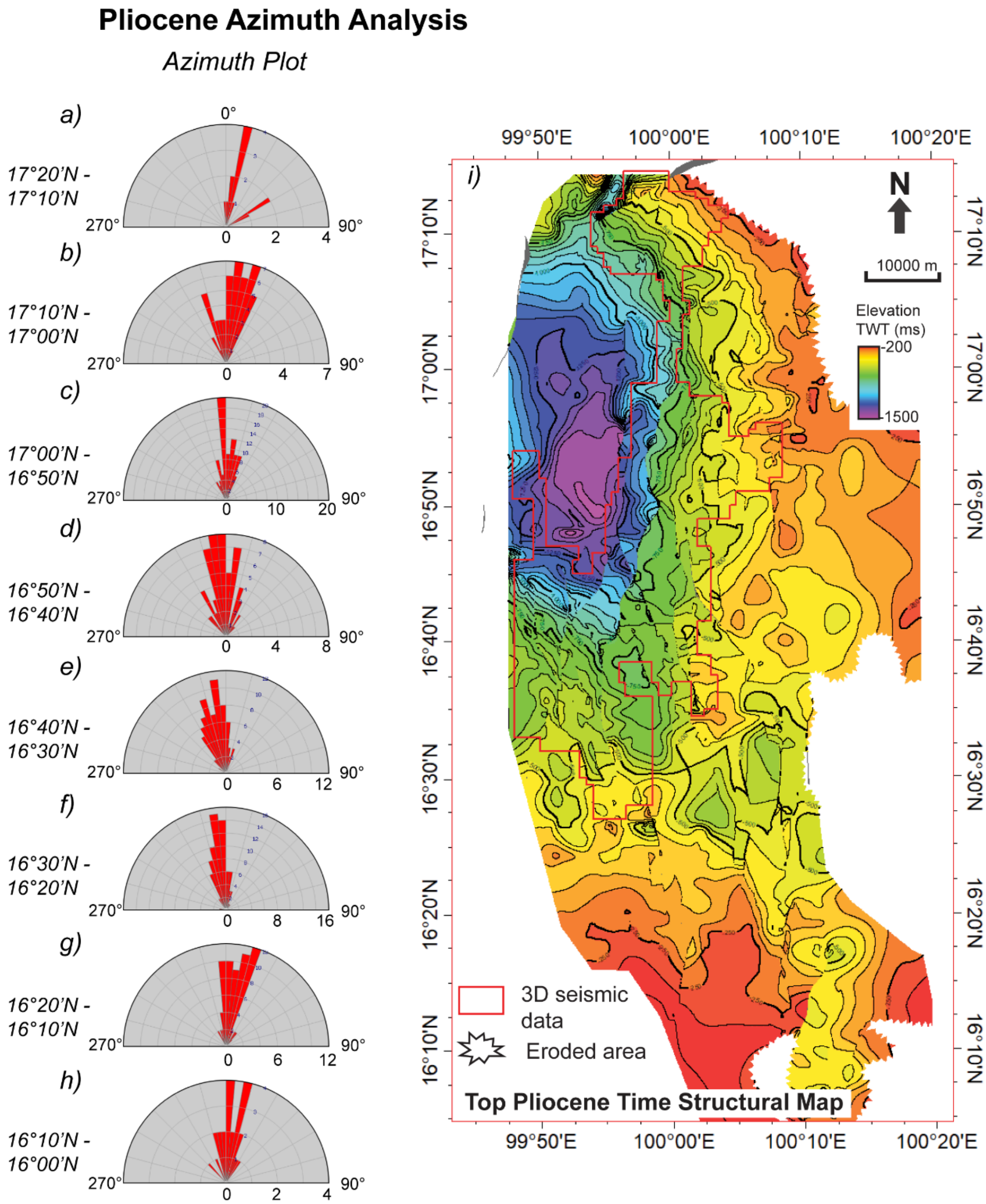

Figure 2.12 a to h) show fault azimuth analysis of the Pliocene horizon plotted on rose diagram against latitude. i) shows top Pliocene time structure map for reference. The 3D seismic data coverage is displayed by the red polygon. The dominant azimuths show minor variations between 16°50'N to 17°10'N. Fault polygons have been accentuated for visibility due to small heaves. TWT = Two-way time. Wavy edges at the map boundaries indicate erosional contacts.

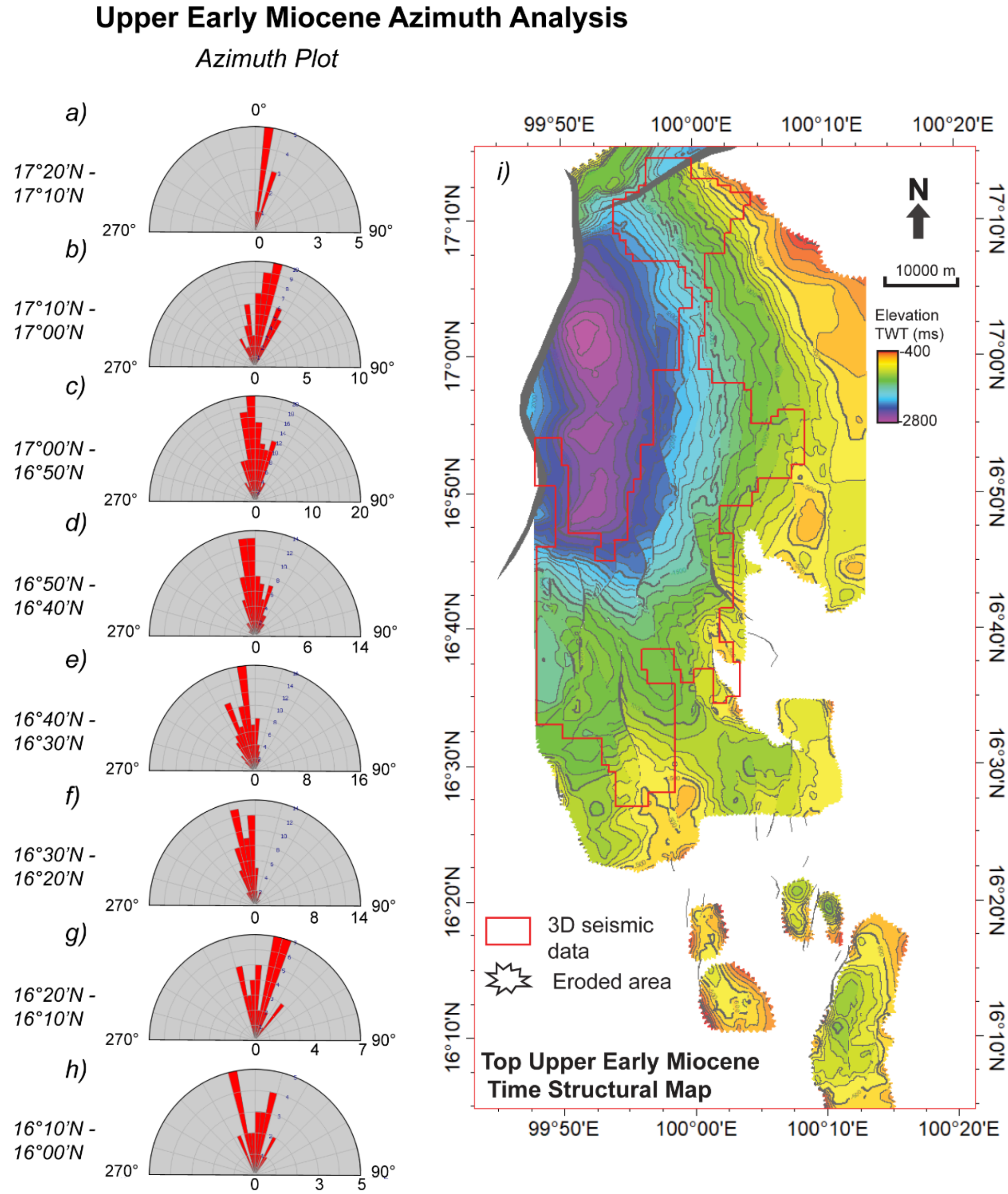

Figure 2.13 a) to h) show fault azimuth analysis of Upper Early Miocene faults plotted on rose diagram against latitude. i) shows Top Upper Early Miocene time structure map for reference. The 3D seismic data coverage is displayed by the red polygon. Fault azimuths show minor variations between 16°50'N to 17°10'N. TWT = Two-way time. Wavy edges at the map boundaries indicate erosional contacts.

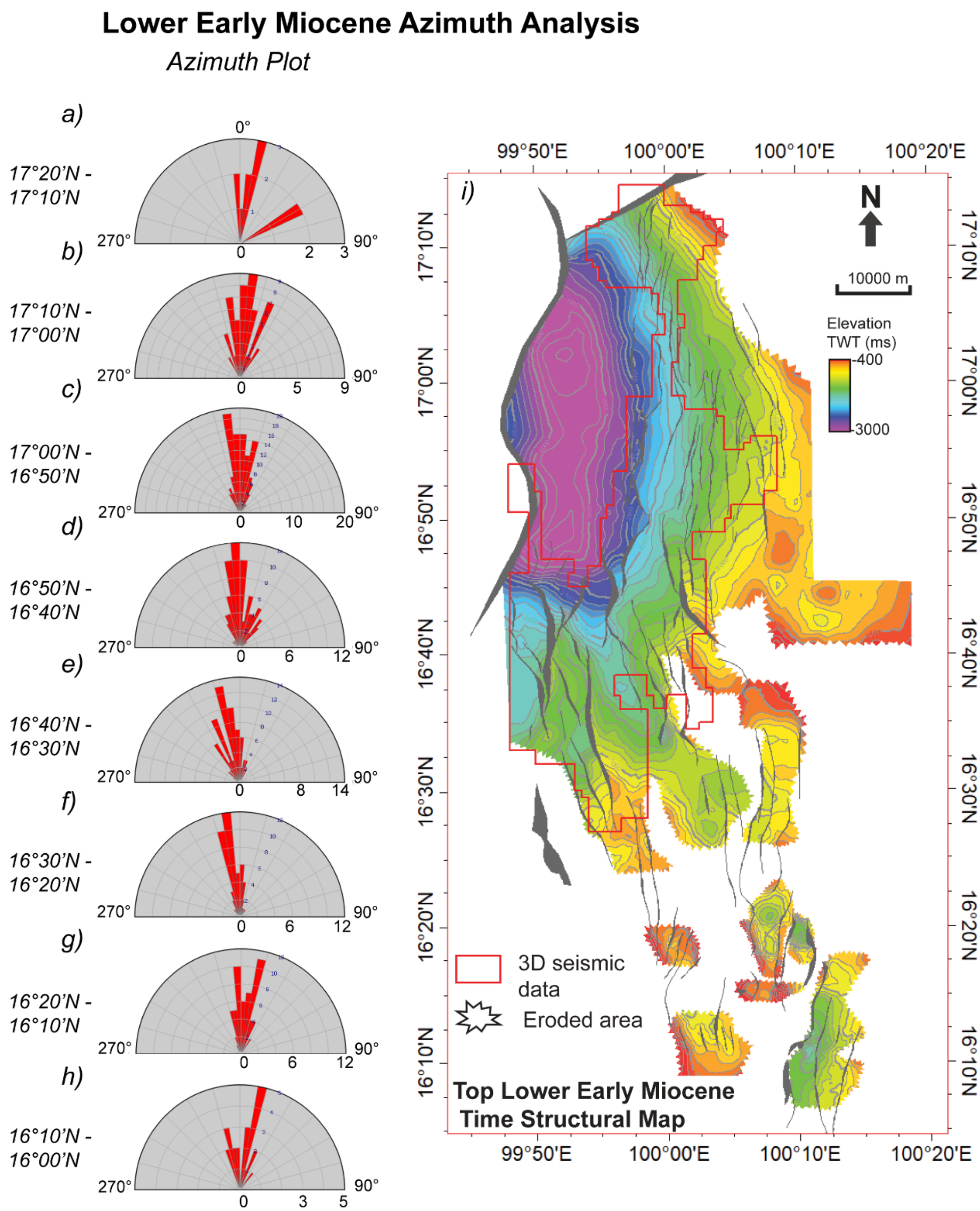

Figure 2.14 a) to h) show fault azimuth analysis of Lower Early Miocene horizon plotted on rose diagram against latitude. i) shows the Top Lower Early Miocene time structure map for reference. The 3D seismic data coverage is displayed by the red polygon. Wavy edges at the map boundaries indicate erosional contacts. TWT = Two-way time.

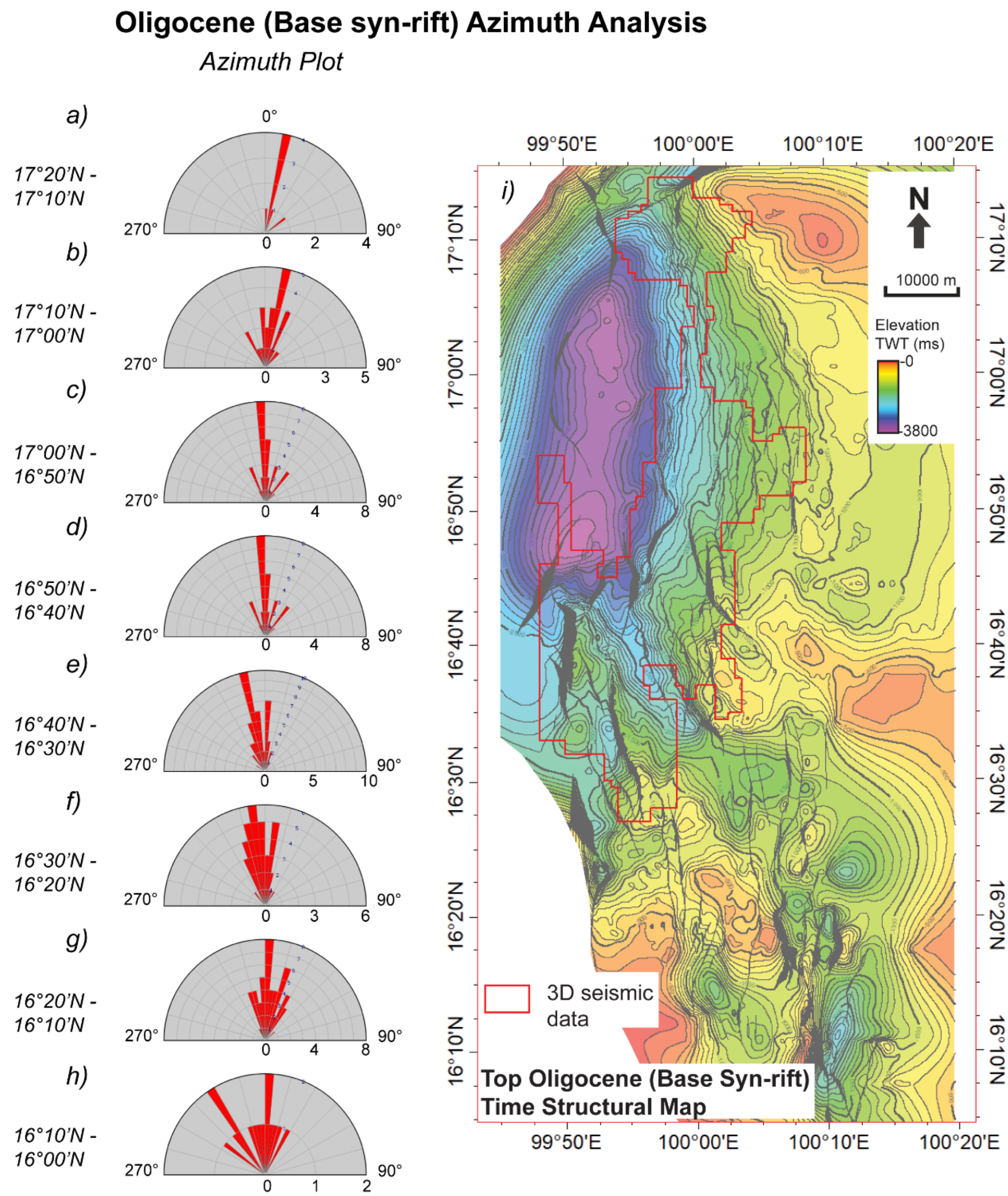

Figure 2.15 a) to h) show Oligocene (Base syn-rift) horizon fault azimuth analysis plotted on rose diagrams by latitude. i) shows the top Oligocene (Base syn-rift) time structure map for reference. The 3D seismic data coverage is displayed by the red polygon. Wavy edges at the map boundaries indicate erosional contacts. TWT = Two-way time.

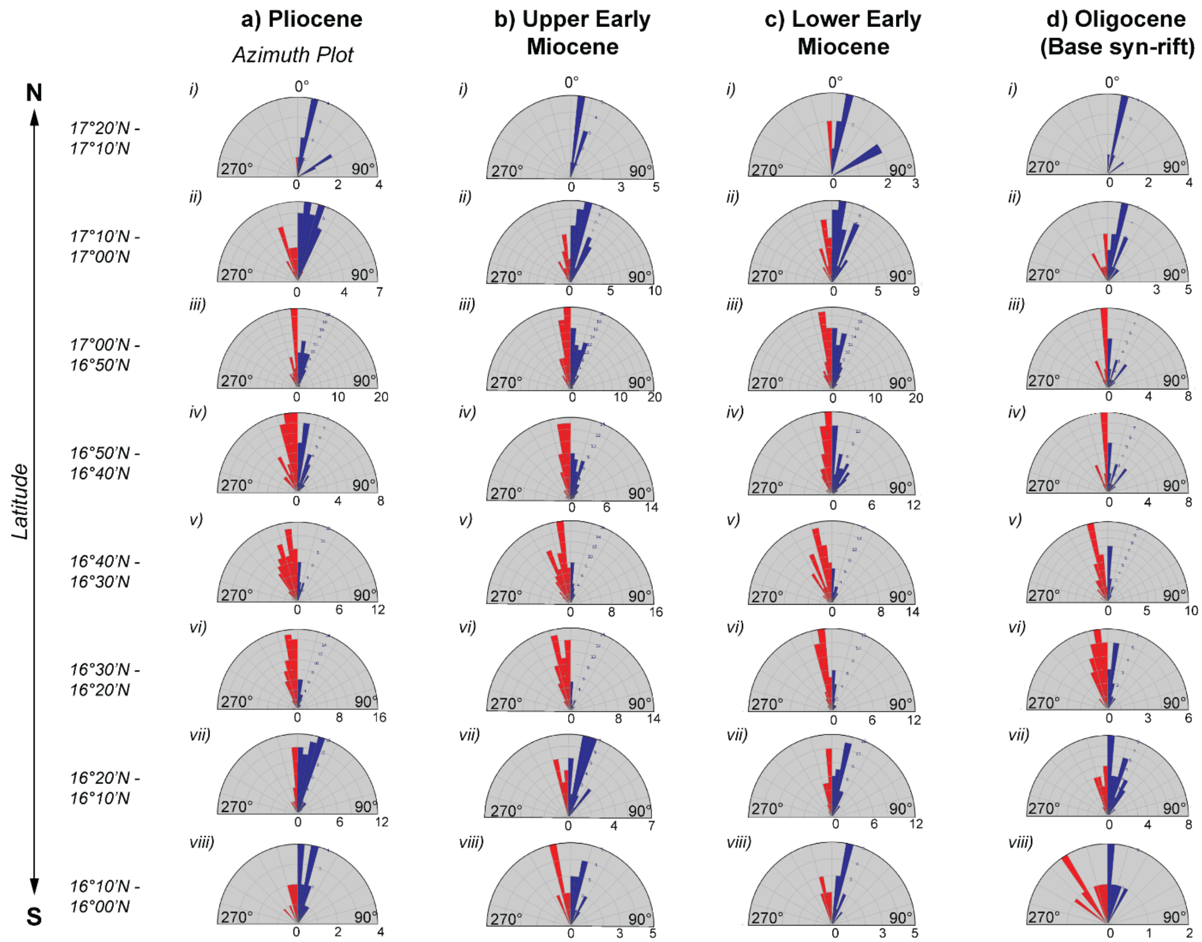

Figure 2.16 Fault azimuths plotted against latitude for the four main horizons in this study: a) Pliocene; b) Upper Early Miocene; c) Lower Early Miocene; and d) Oligocene (Base syn-rift) against latitude. Westerly azimuths are colored red and easterly azimuths are colored blue. The azimuth analysis included major faults the cross-cut the entire stratigraphic section only. In general, all fault azimuths trend N-S. A minor trend of relatively higher NNW-SSE azimuths was noted across 16°50'N to 17°10'N latitudes.

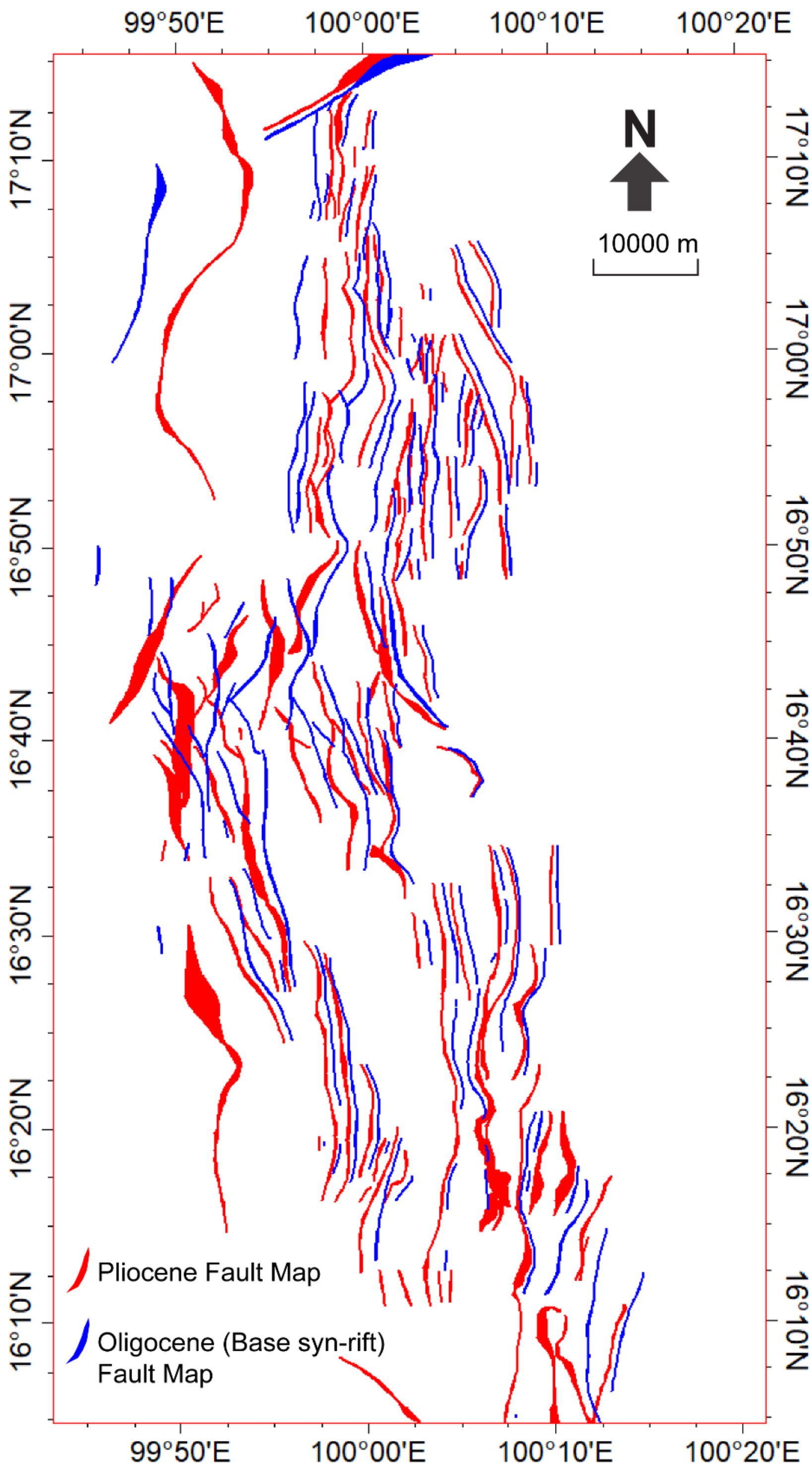

Figure 2.17 Overlay of Pliocene fault map (blue) and Oligocene (Base syn-rift) fault maps (red). Only minor differences of fault azimuths were observed across stratigraphic levels, such as between 16°40’N to 16°50’N latitudes, which is consistent with our approach of analyzing only the major, throughgoing faults that cut the entire stratigraphy.

Fault throw analysis

Fault throw analyses were performed on normal faults that cut the Pliocene, Upper Early Miocene, Lower Miocene and Oligocene (Base syn-rift) as shown in Figure 2.18. The analysis was performed on two-way-time seismic data, which is susceptible to seismic velocity variations, but these variations are likely small in the basin (Figure 2.11). Regardless, we look only for first-order features in this analysis. Also, some fault throws are likely reduced by later erosional events (e.g. Figure 2.4c). The erosional events were mainly observed in the Upper Early Miocene and Lower Early Miocene strata south of 16°40'N latitude. However, we note that a full stratigraphic section still preserved in the lowermost Oligocene (Base syn-rift) Formation, and a near-complete section is preserved in the Lower Early Miocene strata (Figure 2.4a). Therefore, we mainly focus our analysis on the deeper horizons (i.e. Oligocene (Base syn-rift) and Lower Earth Miocene) but show all fault throws for completeness. To illustrate the fault throw patterns of the Phitsanulok basin north and south, the seismic cross sections A-A' and B-B' are later presented in Figure 2.18.

In general, fault throws decrease within stratigraphically higher levels (Figure 2.16), which is consistent with the 'syn-rift' interpretation of our analyzed time periods (Figure 1.7). The Oligocene (Base syn-rift) horizon fault throws showed the strongest variations across the 16°50'N latitudes (Figure 2.16a). Fault throws north of ~16°50'N were generally less than 300 ms TWT, whereas fault throws south of ~16°50'N show fault throws up to ~1000 ms TWT. Similar fault throw variations across ~16°50'N were also observed for the Early Miocene horizons (Figure 2.16b, c). For the Early Miocene and Pliocene horizons, apparently lower fault throws between 16°00'N to 16°30'N latitudes are due to erosion (Figure 2.16b to d). It is more difficult to distinguish fault throw trends within the uppermost Pliocene horizon due to erosion and lower fault throw displacements (Figure 2.16d). Although not directly pointed out in the study, earlier fault throw analyses shown by Morley *et al*. (2007) is consistent with our observations. According to Morley *et al*. (2007), the Pratu Tao (PTO) fault located north of 16°50'N latitude showed smaller (200 m) fault throws compared to 800 m of fault throw along the Nong Tum (NTM) fault, which is located south of 16°50’N.

To better demonstrate variation in fault throws across 16°50’N latitudes, the seismic cross section A-A’ and B-B’ were provided in Figure 2.19. The A-A’ transect located at 17°05’N latitude showed a normal fault array that was formed by high angle faults with smaller throws. As seen in the Oligocene (Base syn-rift) section in Figure 2.19A-A’ it was rare to find the fault throws higher than 300 ms. The B-B’ seismic cross section across 16°35’N illustrated many large fault throws (> 300 ms TWT) in the seismic section Figure 2.19B-B’. Therefore, we conclude that our fault throw analysis is able to indicate a structural transition within the Phitsanulok basin across 16°50’N latitudes, similar to the isochron thickness analysis (e.g., Figure 2.7) and fault dip analysis (e.g., Figure 2.10) above.

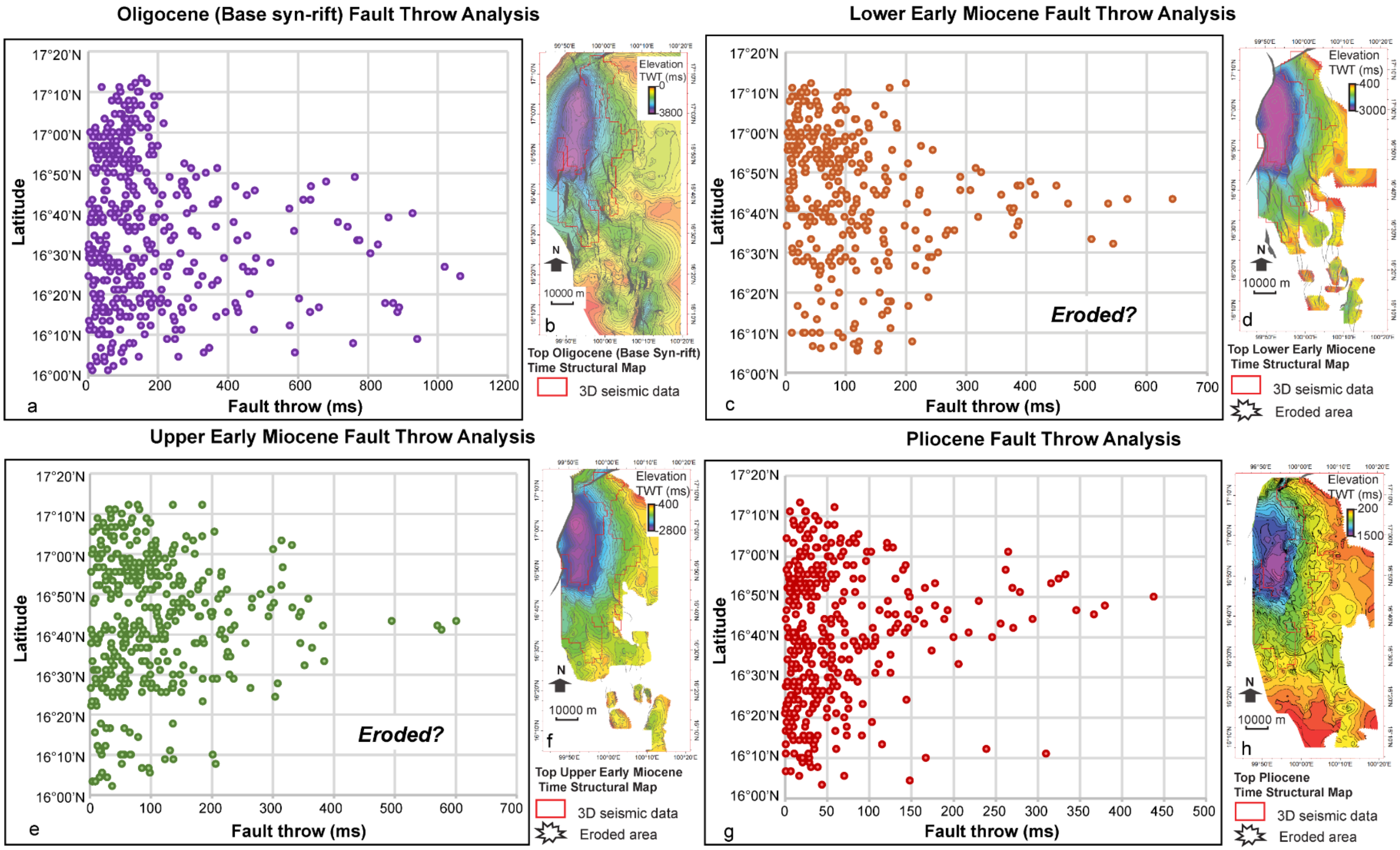

Figure 2.18 a), c), e) and g) Fault throw analysis of the Oligocene base syn-rift horizon (purple dots), Lower Early Miocene (orange dots), Upper Early Miocene horizon (green dots), and Pliocene (red dots) plotted against latitudes, respectively. b), d), f), and h) show time structure maps of the Oligoene (Base syn-rift), Lower Early Miocene, Upper Early Miocene, and Pliocene horizons for reference. For c) and e) latitudes south of 16°30'N show lower fault throws due to erosion.

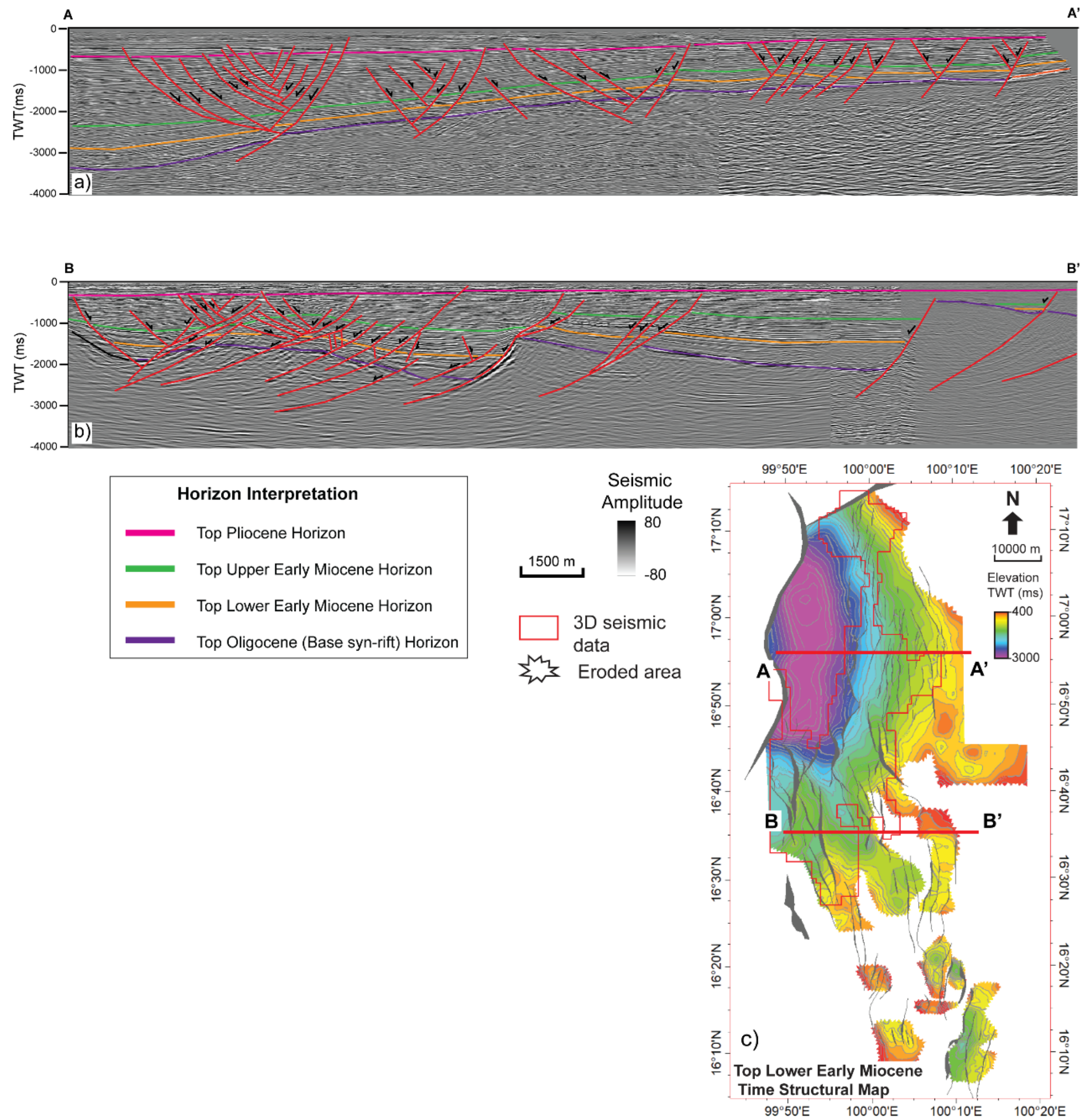

Figure 2.19 Seismic cross section of north and south area showing contrasted fault throws between the northern and southern Phitsanulok basin. a) A-A' seismic cross section in north area (17°05'N) showed only rare large fault throws (>300 ms) within the normal fault arrays. b) B-B' seismic cross section in south area (16°35'N) shows many large fault throws (>300ms). c) Location map of top Lower Early Miocene time structure map. 3D seismic data coverage shown by the red polygon. TWT = Two-way time.

2.3. Discussion

2.3.1.Synthesis: Phitsanulok basin structural domain

To summarize the tectonic domains within the Phitsanulok basin, all analyses were integrated and compared together (Figure 2.20). In general, the following analyses indicate a change across ~16°50'N latitudes: regional seismic transects (Figure 2.3), time structure maps (Figure 2.5), isochron thickness maps (Figure 2.7), fault mapping (Figure 2.8), fault dip angles (Figure 2.9) and fault throws (Figure 2.18). The fault azimuth analysis (Figure 2.16) did not show obvious trends across latitude. This may have been a result of our choice to analyze only the major faults that cut across multiple stratigraphic levels.

In summary, we observed the following structural differences across the Phitsanulok basin:

- North of 16.50°N latitude showed and wide distribution of Sukhothai depression while the south of 16.50°N latitude showed uplifted section (Figure 2.3).
- Oligocene (Base syn-rift) time structural map indicated base syn-rift generally deeper (up to 3800 ms) at the north of 16.50°N latitude and shallower at the south of 16.50°N latitude (up to 200 ms) (Figure 2.5).
- Fault mapping indicated the N - S trend at the north of 16.50°N latitude while mix of NNE – SSW & NNW – SSE and N - S in the south of 16.50°N latitude (Figure 2.8).
- North of 16.50°N latitude, isochron thickness of the Pliocene to Oligocene (Base syn-rift) isochron interval was generally thicker especially in Sukhothai depression (up to 1700 ms) (Figure 2.7a) while south of 16.50°N, isochron thickness were thinner (up to 400 ms) (Figure 2.7a).
- North of 16.50°N latitude showed steeper normal fault dip angle (greater than 45°) with synthetic and antithetic normal fault array (Figure 2.9), in contrast with south of 16.50°N latitudes, where there was a listric fault style with variation of dip angle from deep to shallow section (generally 10° - 45°in deeper section and 60° - 75° in shallower section) (Figure 2.9).

- Areas north of 16.50°N generally showed lower fault throws (<300 ms) whereas areas south of 16.50°N showed larger fault throws (>300 ms) (Figure 2.18).

Based on observation above, we propose two main structural domains in the Phitsanulok basin that we call ‘the Northern domain’ and the ‘Southern domain’, as shown in Figure 2.20.

<table>
<tr><th>Latitude</th><th>Regional Transects</th><th>Time Structural Mapping</th><th>Isochron Mapping</th><th>Fault Mapping</th><th>Fault Dip Angle</th><th>Fault Azimuth</th><th>Fault Throw</th><th>Interpreted Structural Domains</th></tr>
<tr><td>17°20’N
17°10’N</td><td rowspan="3">Sukhothai depression</td><td rowspan="3">Deeper up to 3800 ms at Oligocene (Base syn-rift)</td><td rowspan="2">Thicker sediment layer up to 1700 ms during Pliocene to Oligocene (Base syn-rift)</td><td rowspan="2">N-S trend</td><td rowspan="3">Steep dip angle pattern</td><td>0° - 20° azimuths</td><td rowspan="2">< 300 ms at Oligocene (Base syn-rift)</td><td rowspan="2">Northern Domain</td></tr>
<tr><td>17°00’N</td><td rowspan="3">Limited NNE-SSW azimuths</td></tr>
<tr><td>16°50’N</td><td rowspan="3">Thinner sediment layer up to 400 ms during Pliocene to Oligocene (Base syn-rift)</td><td rowspan="2">Mix of NNE-SSW & NNW-SSE trends</td><td rowspan="3">> 300 ms at Oligocene (Base syn-rift)</td><td rowspan="3">Southern Domain</td></tr>
<tr><td>16°40’N</td><td rowspan="2">Uplifted depression</td><td rowspan="2">Shallower up to 2000 ms at Oligocene (Base syn-rift)</td><td rowspan="2">Listric pattern</td></tr>
<tr><td>16°30’N
16°20’N
16°10’N
16°00’N</td><td>N-S trend</td><td>0° - 15° azimuths</td></tr>
</table>

Figure 2.20 Summary table of tectonic domains in the Phitsanulok basin from the seven structural analyses in this study: Regional transects, Time structural mapping, Isochron mapping, Fault mapping, Fault dip angle, Fault azimuth, and Fault throw analysis. Based on the outcome of these analyses, we divide the Phitsanulok basin into the “Northern” and “Southern” structural domains across 16°50’N latitude.

2.3.2.Phitsanulok basin structural analysis and regional tectonics model

According to Morley *et al*. (2011a); Morley *et al*. (2001), the inversion was occurred in the southern half of the Phitsanulok basin and was possibly caused by the post-Oligocene dextral movement of the Mae Ping fault zone. According to this model, the intensity of the inversion in the Phitsanulok basin will decrease when go further north. This is generally consistent with the results of this study (Table 2.1). However, our analysis defines an abrupt change in Phitsanulok structural domains around 16°50'N.

Fault patterns and the natural limit of large earthquakes occur at 16°45'N latitude (Figure 1.2). Also, earthquake hypocenters change from strike slip to normal and reverse faulting across 16°00'N latitudes. This fits with our 16°50'N structural domain boundary. Furthermore, it is thought that the southern limit of the Sukhothai arc and Nan suture may terminate just south of Phitsanulok basin. The tectonics regions in Thailand (Figure 1.4) indicated an ambiguous of the Phitsanulok basement and their effect. The extension of the Sukhothai arc and Nakhon Thai block to the south were still under debated (Ridd *et al*., 2011). Hence, the variation of tectonics across the Phitsanulok basin could be influenced from the southern extension of basement under the basin. The limit of basement extension could affect the tectonic variation across the Phitsanulok basin such as limit the influence of Uttaradit fault in the north and Mae Ping fault in the south. On the other hand, the structural domain in the Phitsanulok basin could indicate the southern extension of the Sukhothai terrane and Nakhon Thai block basement under the Phitsanulok basin. Therefore, the structural domains defined here may help to show where Sukhothai arc and Nan suture terminate at depth in the crystalline basement. This southern limit also supported by magnetic anomaly sharp contact as in Figure 2.21. The sharp contact of magnetic anomaly could indicate the changing of basement across the Phitsanulok basin due to a terrane boundary.

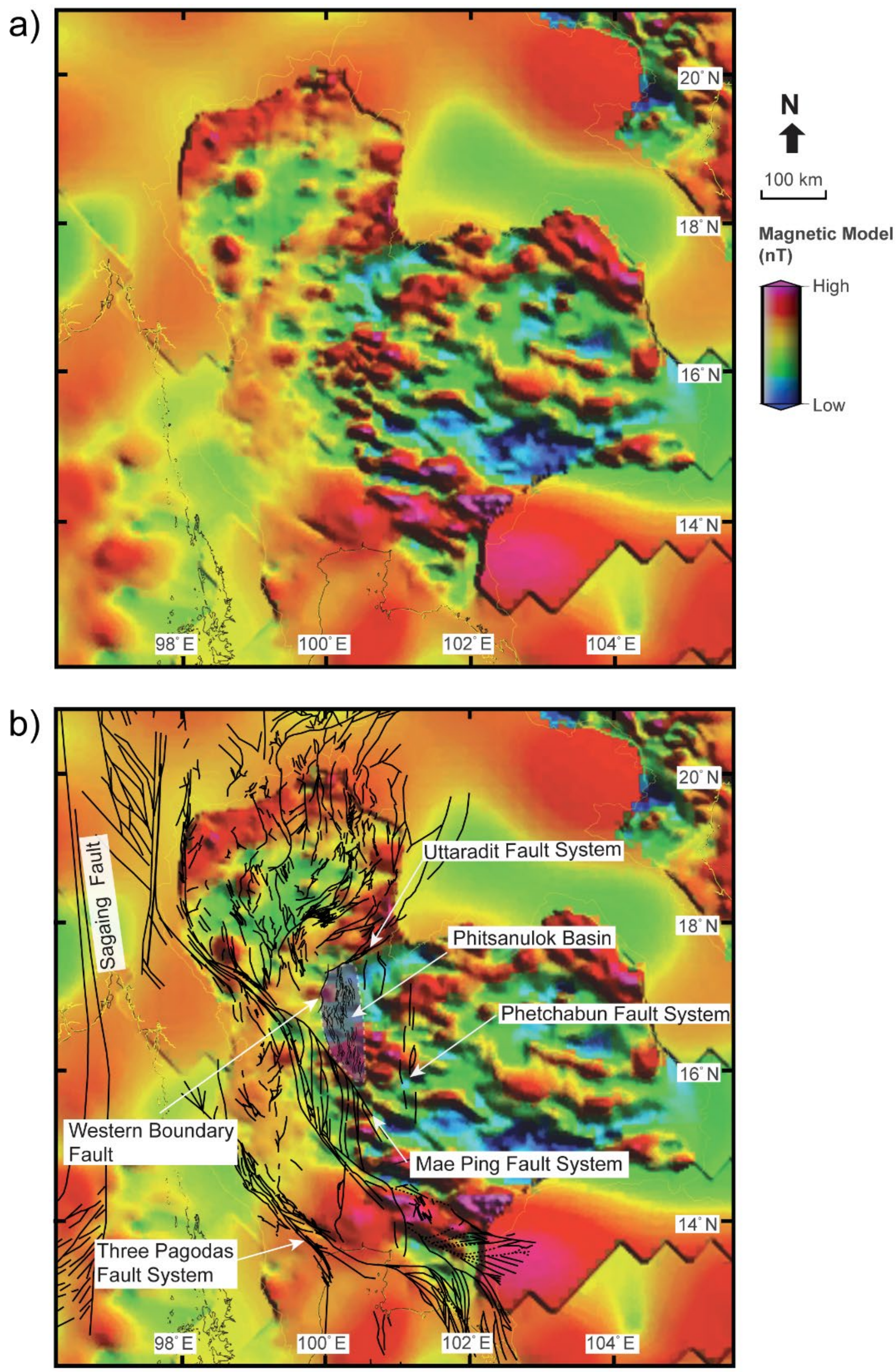

Figure 2.21 Magnetic map in the northern of Thailand indicated the sharp NE-SW trending contact between 16°00'N - 18°00'N latitude and 100°00'E - 102°00'E longitude. We interpret this contact to show a basement terrane boundary. a) Magnetic map without fault zone interpretation; b) Magnetic map in a) with Phitsanulok basin structural features and the interpreted regional faults of Morley *et al*. (2011a).

Our structural domain separation also get along well with suggestion of Morley (2015) which divided the Phitsanulok basin into three domains by structural distribution. The area of inversion alternating with syn-rift section in the southern half (Lahan graben and Nong Bua subasin) and mix of extension and inversion in the Sirikit field could correlate with the inversion effect (southern of 16°50’N latitudes) in this study. The extension mostly in the north could comparable with the extension area in the north of 16°50’N latitudes in this study. However, the separation boundaries of Morley study and this study are different. In this study, the structural domain was separated by latitude base, so the boundary area may not follow the natural elongate of the basin shape. In addition, the boundary domain was also supported by the southern limit of large natural earthquake which proposed by (Morley *et al*., 2011a) (Figure 1.1 and 1.2). The occurrence of southern limit supported the variation of tectonics regime across the Phitsanulok basin. When compare the location of southern limit of large natural earthquake and structural boundary domain from this study, they indicated almost the same location. This could support the structural variation domain from variation of tectonic regimes across the Phitsanulok basin.

2.3.3.Implications for Phitsanulok basin hydrocarbons

Previous studies have suggested that the structural history of the Phitsanulok basin has played a role in hydrocarbon distributions (Morley, 2015). In this section, we make a simple comparison of our Northern and Southern structural domains against hydrocarbon volume estimates and production data provided by PTTEP. Hydrocarbon volumes and production data are obviously affected by many geological (i.e. source, seal, reservoir quality) and engineering factors other than basin structure. Therefore, we limit our analysis to searching only for broad first-order trends, with an aim to deduce whether our mapped structural trends have any obvious effects on the hydrocarbon system. We first begin by characterizing the five main Phitsanulok basin ‘hydrocarbon play trends’, as defined by PTTEP (Figure 2.22). We then compare hydrocarbon volume estimates and production data within these play trends against our mapped structural domains (Figure 2.23 to 2.25). Due to confidentiality, the data are shown by 'bubble plots' that highlight relative quantities but obscure specific numbers.

Review of play type distributions

According to PTTEP (1998, 2016, 2019), the play types varied across the Phitsanulok basin as in Figure 2.22. The Phitsanulok basin was divided into five main plate trends: alluvial fan stratigraphic traps, upthrown fault closures, unconformity basement highs or onlaps, combined up- and downthrown fault closures, and pinch out stratigraphic traps (PTTEP, 2016).

Play Trend 1: Alluvial fan stratigraphic trap

In this trend, the reservoir is Sarabop (SBP) Formation which is an alluvial fan developed along the Western Boundary fault (PTTEP, 2017b). This trend is completely within our Southern structural domain (Figure 2.22). The original oil in place (OOIIP) was calculated to be approximately 14 MMBBL as in Figure 2.23 (PTTEP, 2016). There is no well success to prove hydrocarbon potential in this area. Hence there is no available production data within this play trend. Due to limited well and production data in this Play Trend 1, this trend is shown but excluded from the discussion below.

Play Trend 2: Upthrown fault closure trap

This trend has a major reservoir in Lan Krabu (LKU) Formation, which is an interfingering between sandstone and shale in lacustrine depositional environment (PTTEP, 1998, 2018; Thai Shell Exploration and Production Co.Ltd, 1988). This trend is completely within our Southern structural domain (Figure 2.22). Lower angle faults are generally observed in this area as in Figure 2.11. Hence the main trap mechanisms are upthrown fault closures as in Figure 2.22. There have been successful wells that have proven hydrocarbon potential in this trend since 1983 (Bal *et al.*, 1992; Brooks, 1986; Knox and L Wakefield, 1983; PTTEP, 1998). The original oil and gas in place were calculated to be approximately 1300 MMBBL and 350 MMBOE, respectively as in Figure 2.23 (PTTEP, 2016). Significant oil and gas production rates were observed at approximately 22500 bbl/d and 5000 BOE/d respectively as in Figure 2.24 (PTTEP, 2019).

Play Trend 3: Unconformity basement high or onlap trap

The third play trend straddles both the Northern and Southern structural domains, as in Figure 2.22. The 'basement' formation, which is a major reservoir, plays the major role in this trend (Figure 2.22a). The reservoir in this area is varies from a pebble lag just above basement to the alluvial fan on top of the basement (PTTEP, 2016). Hydrocarbons have been proven within this trend since 1980 (Knox and L Wakefield, 1983; PTTEP, 1998). The southern part of this trend is affected by erosion and structural inversion. The original oil and gas in place in this area were at approximately 200 MMBBL and 30 MMBOE, respectively as in Figure 2.23. There were around 1700 bbl/d and 2350 BOE/d of oil and gas produced from this area as in Figure 2.24 (PTTEP, 2019).

Play trend 4: Combined up- and downthrown fault closures

The fourth play trend appears to straddle both our Northern and Southern structural domains; however, in essence the trend is located along faults within the Northern domain, as in Figure 2.22. Therefore, for this study we will consider this play within the Northern domain. This trend is dominated by a higher angle normal faults (Figure 2.10), as discussed in Chapter 2. Hydrocarbons are sealed against both up- and downthrown fault closures in this area (PTTEP, 2016). The primary reservoir in this area was Lan Krabu Formation. The original oil and gas in place were approximately 200 MMBBL and 5 MMBOE respectively as shown in Figure 2.23 (PTTEP, 2016). The total oil and gas production produced from this area was approximately 2000 bbl/d and 2400 BOE/d respectively as in Figure 2.24 (PTTEP, 2019).

Play trend 5: Pinch out stratigraphic traps

The fifth play trend is located entirely in our Northern structural domain and is dominated by purely extensional fault patterns, as discussed in Chapter 2. The major trap mechanism is a pinch out stratigraphic trap as shown in Figure 2.22 (PTTEP, 2016). The reservoir in this trend is the Mae Nam Nan formation (PTTEP, 1998, 2016). The original oil in place in this area was approximately 16 MMBBL (Figure 2.23) (PTTEP, 2016). Due to limited accessibility of drill site locations, the cumulative oil and gas production rate in this area was only around 60 bbl/d and 5 BOE/d respectively as in Figure 2.24 (PTTEP, 2019).

Comparison between two structural domains

Initial hydrocarbon in place

The hydrocarbons initially in place (HCIIP) volumes are dramatically elevated in our Southern structural domain relative to the Northern domain (Figure 2.23). Our preferred explanation is that the greater effect of inversion in the southern Phitsanulok basin (e.g., Morley, 2015) creates and enlarges the trap sizes in the Southern domain relative to the Northern domain (see Figure 2.19 for comparison of structures). Within our Southern domain, play trend 2 shows higher HCIIP volumes (Figure 2.23). This may be due to the relative proximity of Trend 2 to source rocks within the Sukhothai depression. Morley (2015) also speculated that tilted fault blocks near the Sukhothai depression were favorable for hydrocarbon accumulations.

At the far southern end of our study area, south of 16°30’N latitude and further south than Trend 3, Morley (2015) interpreted an intensive effect of two inversion phases that resulted limited structural closures; source rock maturation was terminated during inversion. The intense inversion was probably the main factor for absence of hydrocarbon accumulation in the southernmost area in the Phitsanulok basin (Morley, 2015). This result could suggest that the inversion with high level of erosion is not suitable to consider for exploration in the next exploration campaign of PTTEP in term of initial hydrocarbon in place. In conclusion, we speculate that our Southern structural domain between 16°50’N and 16°30’N (Trends 2,3, and 4) could be more favorable for hydrocarbon exploration compared to the purely extensional zones within the Northern structural domain and the areas south of 16°30’N, which have been strongly inverted.

Cumulative production per day

Figure 2.24 shows better overall cumulative hydrocarbon production within the Southern structural domain compared to the Northern domain. However, the cumulative production data may be slightly misleading, as the total hydrocarbon production in each trend is also a product of the numbers of producing wells. To provide an alternative perspective, we show a separate bubble plot for hydrocarbon production rate per well in Figure 2.25. This plot shows relative similar production rates per well across the study area. We note slightly lowered well productivity within Play Trend 3, which has been most affected by erosion (Figure 2.25). We speculate that the well production performance in this area could be affected by reservoir quality due to the erosional episodes, but further investigation is needed.

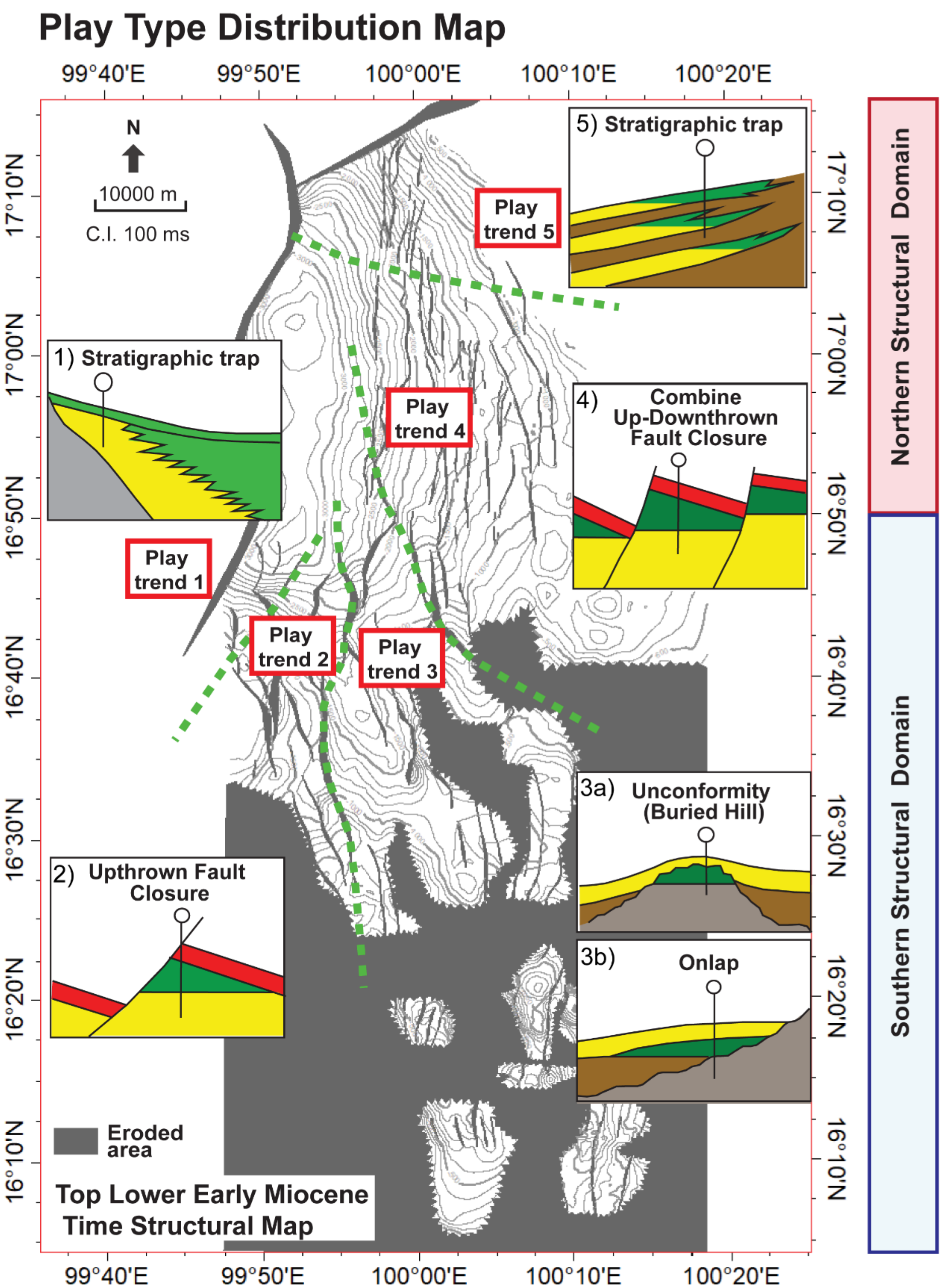

Figure 2.22 Phitsanulok basin petroleum play trend map showing the five main play types within the basin (PTTEP, 2016). Each play type is illustrated by the schematic cartoon cross-sections. C.I. = Contour interval.

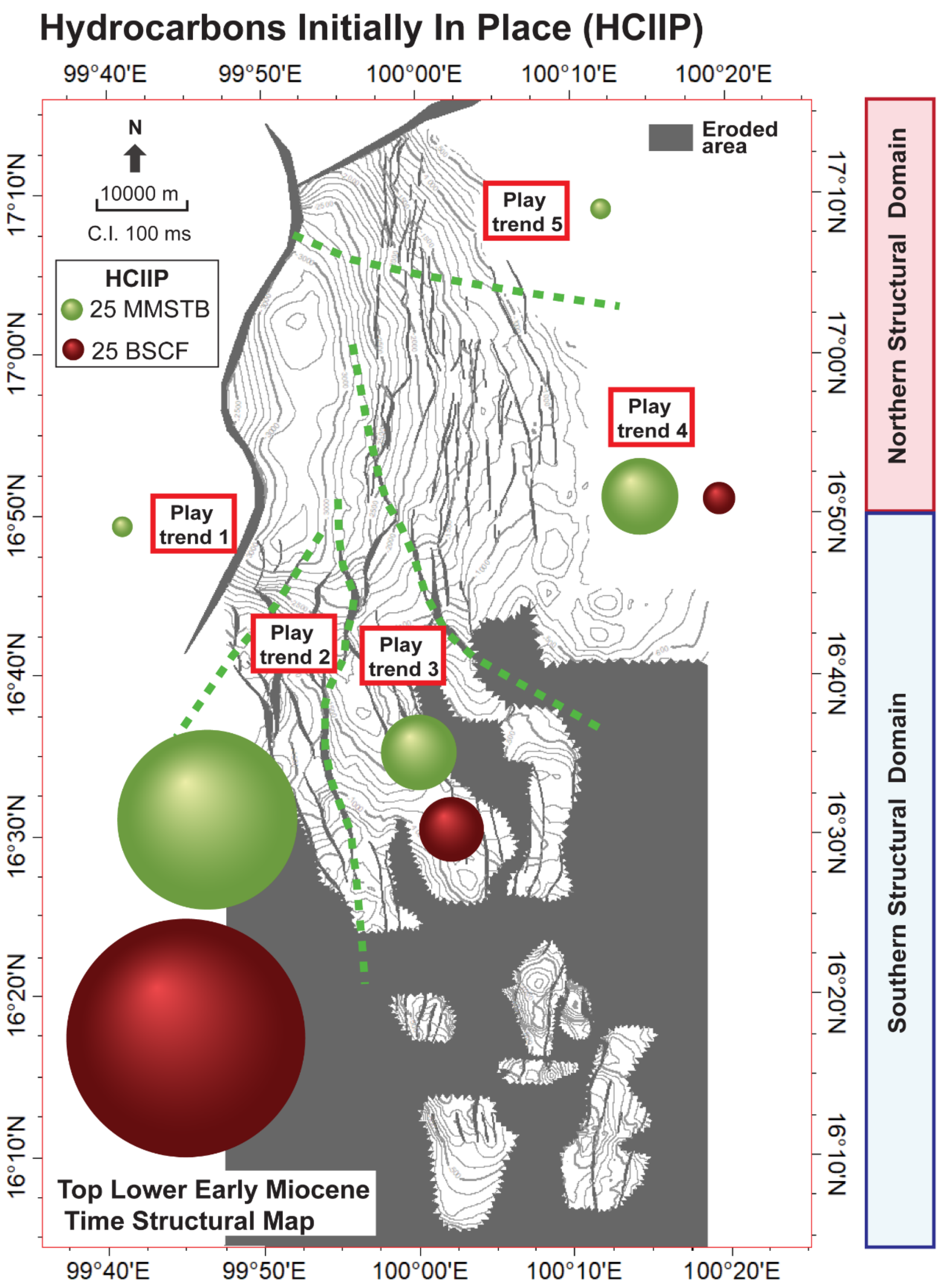

Figure 2.23 Hydrocarbon initially in place (HCIIP) volumes in the Phitsanulok basin shown by relative bubble size and colored by oil (green) and gas (red) (PTTEP, 2016). HCIIP = Hydrocarbon initially in place, C.I. = Contour interval.

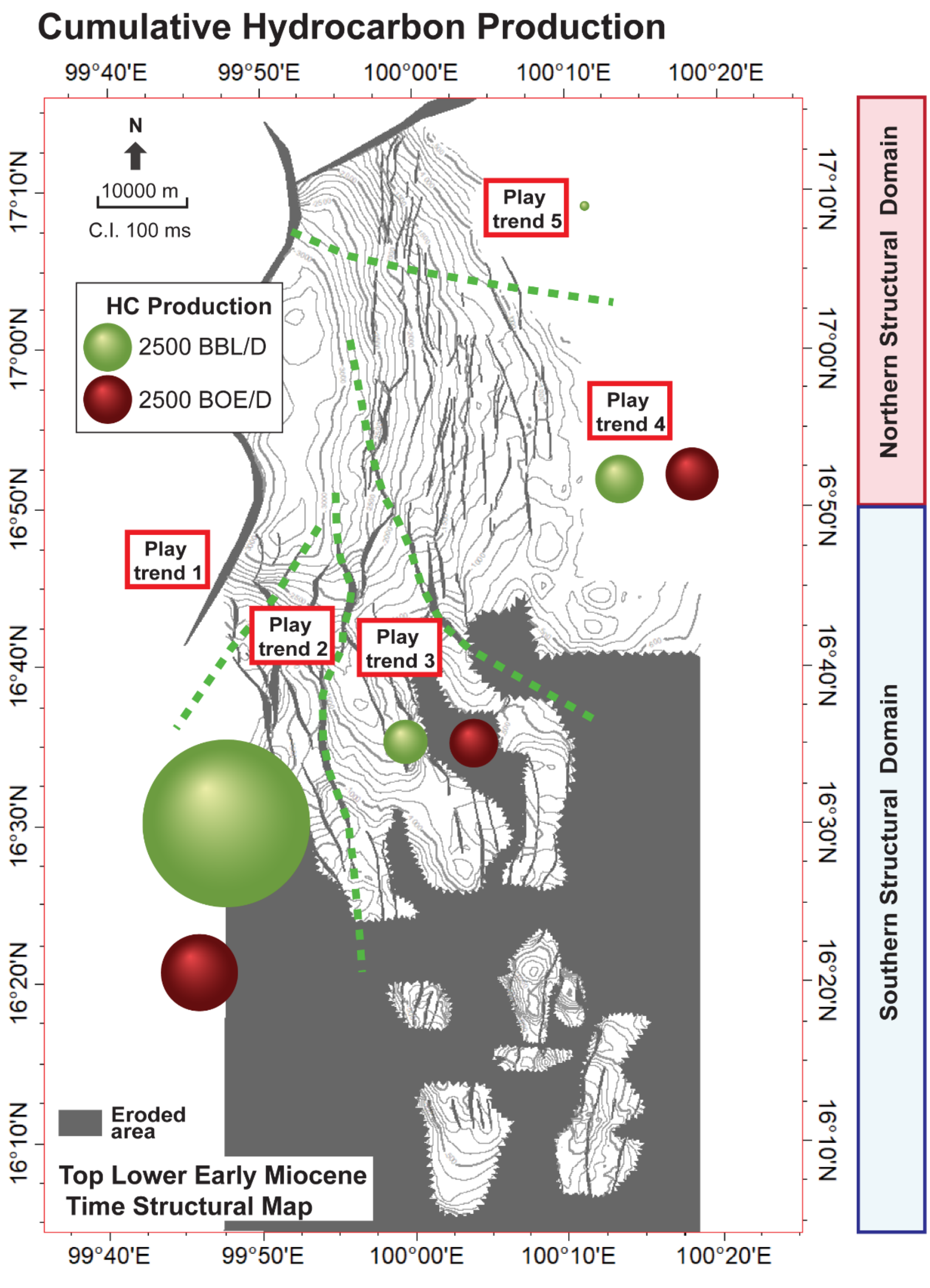

Figure 2.24 Phitsanulok basin cumulative production data as of February 2019 shown by play trend. The size of bubble represents the relative quantities of hydrocarbon production; oil in green (BBL/D) and gas in red (BOE/D) (PTTEP, 2019). HC Production = Hydrocarbon Production, C.I. = Contour interval.

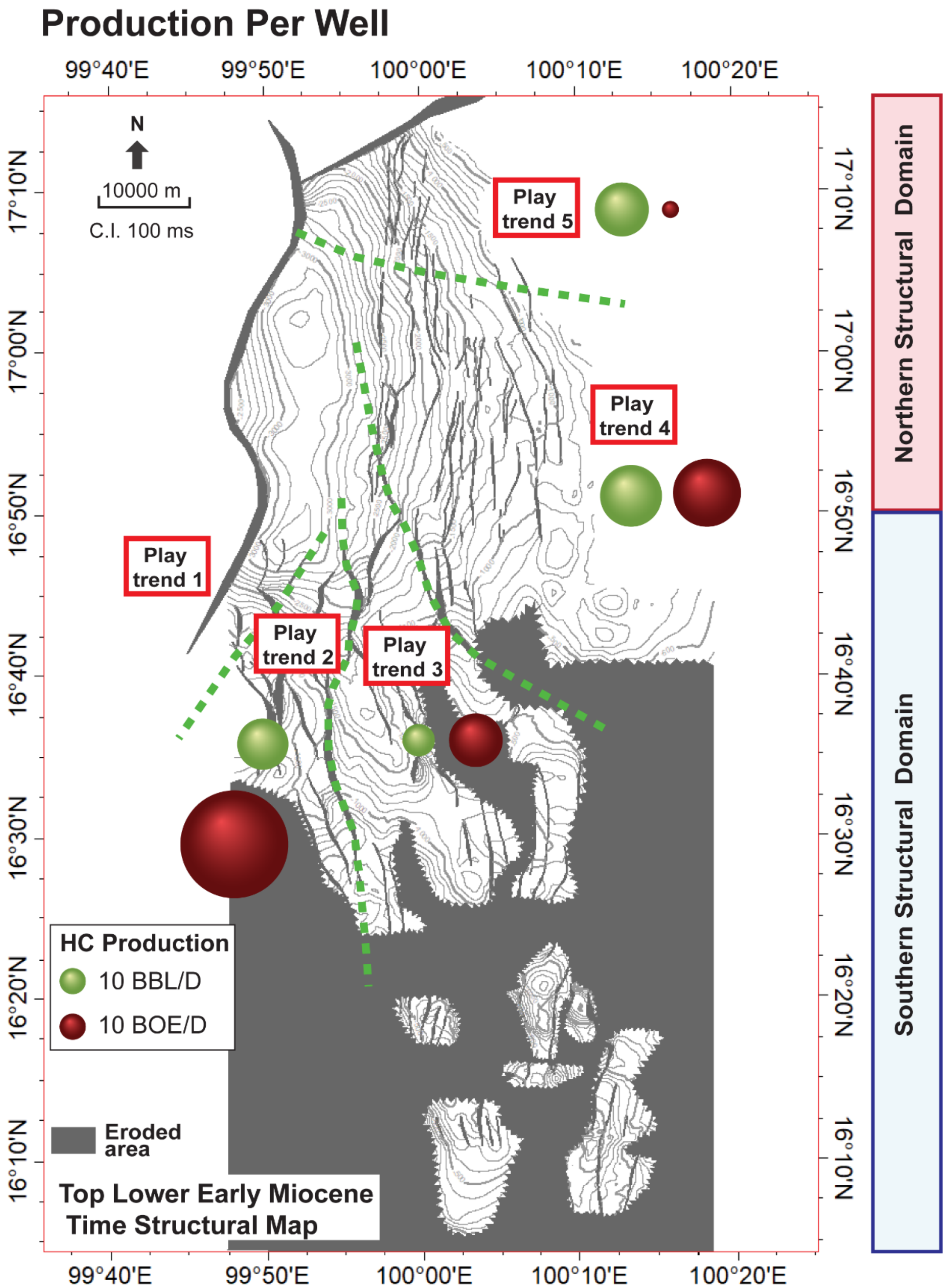

Figure 2.25 Phitsanulok production per well data as of February 2019, separated by play trends (PTTEP, 2019). The size of bubble represents the relative amount of hydrocarbon production; oil in green (BBL/D) and gas in red (BOE/D). HC Production = Hydrocarbon Production, C.I. = Contour interval.

2.4 Conclusion

Based on our tectonostratigraphic analyses of the Phitsanulok basin (summarized below), we conclude that a quantitative change in structural domains occurs across 16°50'N latitudes. We call these the Northern and Southern structural domains, respectively. North of 16°50'N latitudes, the Phitsanulok basin showed near-planar, steeply-dipping normal faults; cross cutting of synthetic and antithetic extensional faults array; a thickened deep zone with 1700 ms two-way time (TWT) thickness between the Pliocene to Upper Early Miocene horizons; fault dip angles that vary within 60°-75°dips; and, fault throws <300 ms TWT in the Oligocene (Base syn-rift).

On the other hand, south of 16°50'N latitudes the Phitsanulok basin shows listric-style extensional faults; a thinner stratigraphic section (~400 ms TWT) between the Pliocene to Upper Early Miocene horizons; more gently-dipping faults (10°-55°); and, fault throws >300 ms TWT in the Oligocene (Base syn-rift). We attribute these structural differences partly to structural inversion. However, there is also evidence for a change in the basement and deeper tectonic structure near our identified 16°50'N domain boundary. For example, our 16°50'N domain boundary is near the southern limit of large natural earthquake within Thailand as identified by previous studies. In addition, the earthquake hypocenters and magnetic anomaly change across that boundary. Furthermore, our 16°50'N Phitsanulok basin structural domain boundary occurs near the southern limit of the Sukhothai arc and Nakhon Thai block and may be influenced by these deep tectonic features. Comparison of our Northern and Southern structural domains to PTTEP hydrocarbon accumulation and production data shows the Southern domain is generally more favorable for hydrocarbons. However, hydrocarbon initially in place and well production performance are decreased south of 16°30'N. We speculate that this could be a result of erosion due to stronger inversion in the southernmost Phitsanulok basin.

Chapter 3 Sandbox Models

3.1 Motivation

Inverted fault systems are extensional faults that experience compression stress after the initial extensional stress (Cooper *et al*., 1989). Sedimentary basins with inverted faults can contain commercial hydrocarbon deposits and production (Harding, 1985; Wang *et al*., 2017). Reversal of the stress regime from extension to compression has effects on structural styles, produces reactivated faults, and may produce uplift (Cooper *et al*., 1989; Gomes *et al*., 2010; Harding, 1985; McClay, 1989; Panien *et al*., 2005). Basin inversion characteristics has been studied for natural basins (Harding, 1985) as well as simulated in sandbox models (Gomes *et al*., 2010; McClay, 1989; Panien *et al*., 2005; Richard and Krantz, 1991; Wang *et al*., 2017). However, few analog model studies have focused on inverted strike-slip basins.

Strike-slip pull-apart basins typically develop along releasing bends or stepovers (Burchfiel and Stewart, 1966; Mann *et al*., 1983; Wu *et al*., 2009). In some areas, particularly within Southeast Asia (Morley *et al*., 2011a; Ridd *et al*., 2011), changes in regional plate motions can cause a slip-sense reversal of a strike-slip fault (i.e. a change from sinistral to dextral strike-slip motions, or vice versa). Slip-sense reversal can cause inversion of a pre-existing pull-apart basin, such as the Yinggehai basin, offshore western South China Sea (e.g., Fyhn and Phach, 2015; Lei et al., 2015; Rangin et al., 1995), or the Mae Sot basin, Thailand (Morley *et al*., 2011a). In this study, slip-sense reversal on pull-apart basins is investigated using sandbox models. The sandbox experiments were based on well-studied, underlapping 30° releasing bend pull-apart basin sandbox models (McClay and Bonora, 2001; McClay and Dooley, 1995; Sugan *et al*., 2014; Wu *et al*., 2009). Here we conduct a sandbox modeling study of inverted pull-apart basins with two aims: (1) to characterize inverted strike-slip fault systems within sandbox models and compare to sandbox models of inverted rift basins; and, (2) to develop a workflow to structurally characterize the 3D internal geometry of sandbox models with complex fault systems.

3.2 Data and methodology

This study is composed of three sandbox analog models: a) pull-apart basin (reference model), b) transpressional pop-up basin and c) inverted pull-apart basin (pull-apart followed by transpression). The models had similar initial conditions; the only changes were the implemented plate motions above. Quantitative comparisons of sandbox model fault geometries and basin evolution was performed from top surface photographs and internal sections. To complement these analyses, a novel workflow was constructed to build 3D digital model reconstructions from serial cross-sections using Petrel and Cegal seismic interpretation software (see Appendix). The results of this workflow are shown later in this section.

3.2.1. Sandbox model experimental procedure

The sandbox models in this study were conducted using a deformation rig that had aluminum baseplates cut with a 30° underlapping releasing-bend stepover (Figure 3.1), similar to Wu *et al*. (2009). During the experiments, the basement plates were displaced by stepper motors at average rate of 2 cm/hr using pure strike-slip motions. A rubber sheet was glued beneath the basement plates to distribute strain across the plate boundaries. The dimensions of the sandbox model were approximately 150 × 50 × 7.5 cm. The model scaling was 10^{-5} such that 1 cm in the models represented 1 km in nature. Sandbox experiments used in this study were performed at the Fault Dynamics Research Group laboratory at Royal Holloway, UK, by Dr. Jonny Wu. Sandbox experiments were monitored by photographs and laser scans of the top surface after every 1.0 cm of displacement. Photographs of the internal vertical sections were acquired after the experiment at 0.4 cm increments.

At the start of each experiment, pre-kinematic sand layers were infilled to approximately 7.5 cm thickness. The pre-kinematic sand layers were colored blue, white, and black (Figure 3.2). After 3 cm of horizontal strike-slip displacement along the master fault, syn-kinematic sediment layers were infilled. The first syn-kinematic sand layers were colored red and white (Figure 3.2). For the inversion model 3, additional layers of syn-inversion sediments were added in a second inversion phase after 10 cm of strike-slip displacement. The syn-inversion sand layers were colored green and white (Figure 3.2).

The top view of sandbox models was captured by overhead photographs after every 1 mm of horizontal displacement. Laser scans were acquired every 1.0 cm of horizontal displacement. Laser scanner data were used to calculate subsidence or uplift rates. All complete models were gelled and vertically sliced at 4 mm increments and then photographed. The summary of sandbox parameters and data acquisition are shown in Table 3.1.

The sandbox model serial cross-section photos were processed as .tiff raster images. The raster files were populated into an empty seismic volume that was consistent with the sandbox scaling ratios (see Appendix). All photos were then imported into Petrel software using a Cegal Blueback academic license plugin to create a sandbox seismic 3D volume. The 3D reconstruction workflow is illustrated in Figure 3.3 and described in detail in the Appendix.

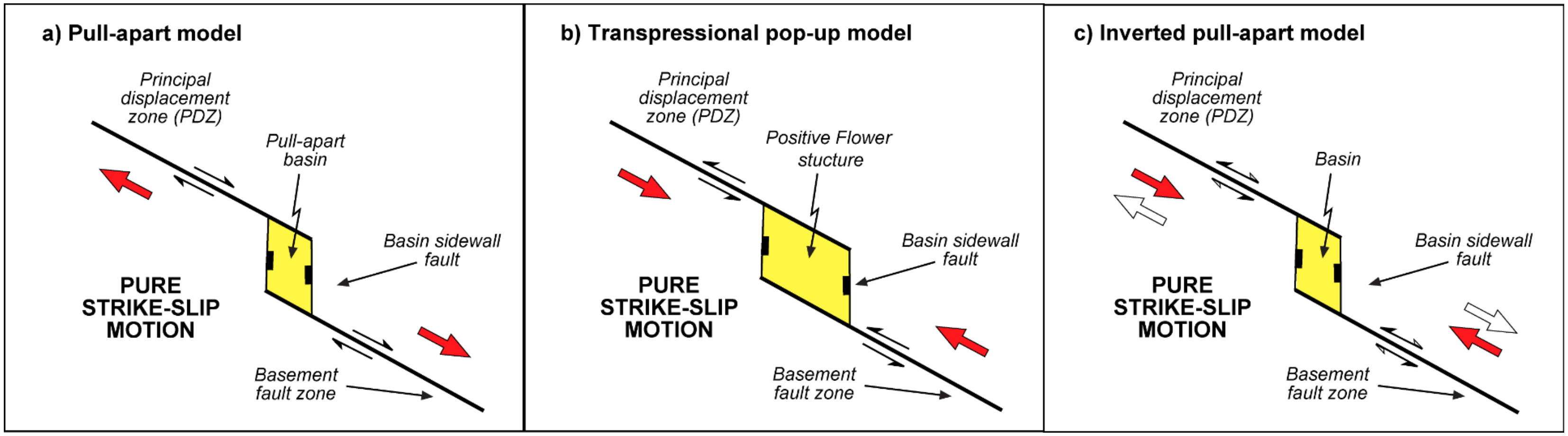

Figure 3.1 Sandbox model experimental procedure showing: a) Pull-apart model; b) Transpressional pop-up model; and c) Inverted pull-apart model configurations.

Sandbox model stratigraphy

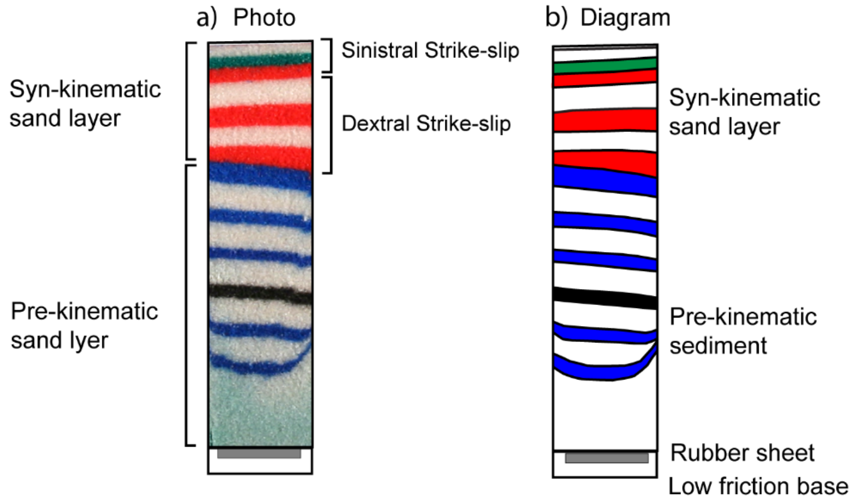

Figure 3.2 Sandbox model stratigraphy. a) Photograph of sandbox model cross section. b) Line drawing interpretation of a). The pre-kinematic strata were represented by white, blue, and black sand layers. The first syn-kinematic sediment layer was red and white in color. The syn-inversion strata are shown by the green and white sand layers.

Table 3.1 Sandbox model experiment and data acquisition

Sandbox model	**Experimental parameters**					**Data acquisition**		
	Stepover	**Translation**	**Plate motion**	**Sand /Clay**	**Total displacement**	**Top shots**	**Sections**	**Laser scanner**
Model 1: Pull-apart	30°	Pure strike-slip	1:1	Yes	6 cm	1 mm	4 mm	1 cm
Model 2: Transpressional pop-up	30°	Pure strike-slip	1:1	No	10 cm	1 mm	4 mm	1 cm
Model 3: Inverted pull-apart	30°	Pure strike-slip	1:1	No	10+10 cm	1 mm	4 mm	1 cm

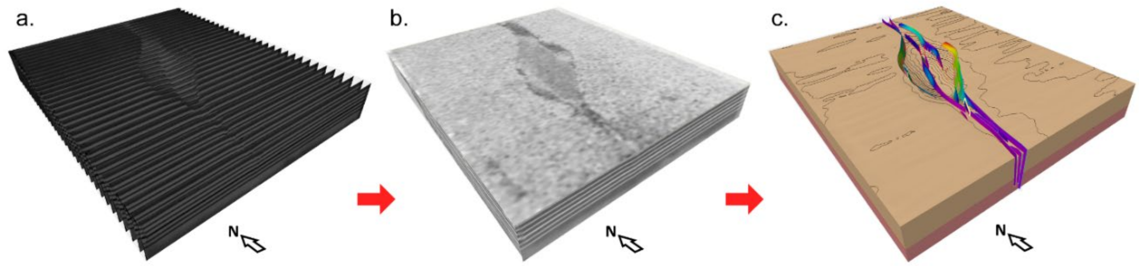

Figure 3.3 3D model reconstruction workflow. a) The cross-section photographs of sandbox were imported into Petrel software using the Cegal plugin. b) shows the 3D seismic cube that was generated from the cross-section photographs. c) The 3D seismic cube was interpreted to make a 3D reconstruction model. Additional details are available in Appendix A.

3.2.2.Sandbox model 3D interpretation

To analyze the inverted pull-apart basin model 3 in detail, all faults within the sandbox model and three key horizons (top pre-kinematic, top syn-kinematic, and top syn-inversion) were picked. The top pre-kinematic horizon was presented by the uppermost blue sand layer in the cross section. The top syn-kinematic horizon was recognized by the uppermost red sand layer and the top syn-inversion was the uppermost green sand layer. The fault framework models were constructed from faults which were picked in every single sandbox cross section slice. The full 3D models were then created from the fault framework and horizon interpretations. The full 3D models were used to analyze the fault dip angle, fault azimuth and inactive fault. The comparison of model 3 and the reference models (model 1 and model 2) was performed to identify inversion effects.

3.3 Sandbox model analysis results

3.3.1.Sandbox models interpretation

Pull-apart basin model 1

Model 1 was the reference model for pull-apart basin. Model 1 developed a rhomboidal basin bordered by oblique extensional faults within the central stepover area (Figure 3.4). The basin development sequence was illustrated in Figure 3.4. Changes in the top surface sand colors show the addition of syn-kinematic sediment, as described in the methods. Laser scanner photographs were used to generate subsidence isopach maps as shown in Figure 3.4b. After 3 cm of horizontal displacement along the master faults, an elongated rhomboidal central basin was formed that was bounded by two oppositely-dipping basin border faults (3 cm in Figure 3.4a, b). Laser scans show the development of two depocenters within the larger central basin that were divided by a central extensional fault (3 cm in Figure 3.4a, b). After 6 cm of horizontal displacement along the master faults, basin subsidence was accommodated by pre-existing faults (6 cm in Figure 3.4a, b). The central basin continued to subside and showed one central depocenter (6 cm in Figure 3.4a, b). The final basin border faults were formed by linked extensional fault segments that were oblique to the master fault orientations (Figure 3.4c). Vertical cross-sections through the center of the final model revealed basin bounding normal faults that showed steep dips (60° to 80°) (C-C' in Figure 3.5a). Faults within the basin were characterized by an array of cross-cutting normal faults and a near-vertical strike-slip fault that showed negligible vertical displacements (C-C' in Figure 3.5a).

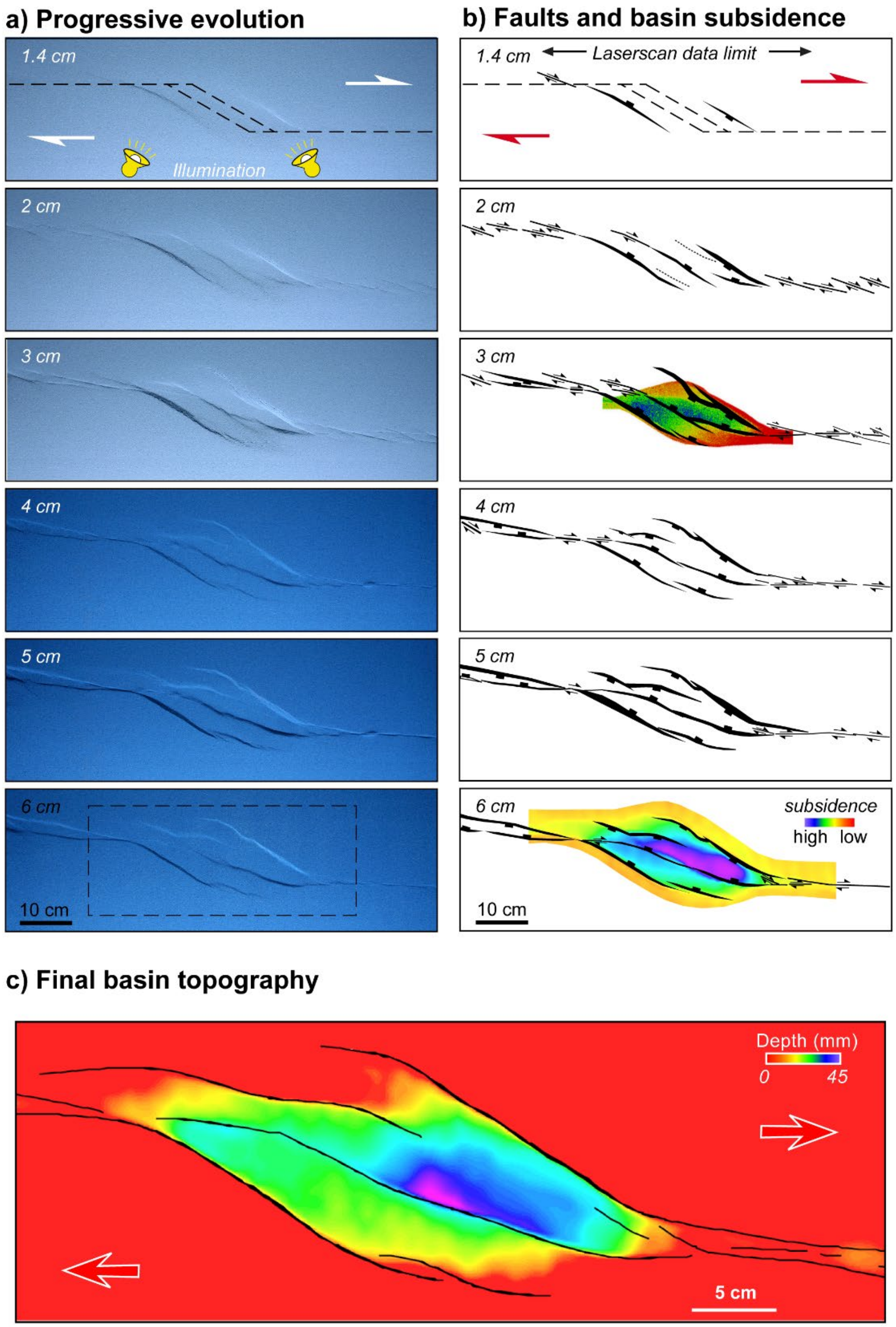

Figure 3.4 Plan view evolution of the reference pull-apart basin model (model 1). a) Time lapse plan view photography from 1.4 cm to 6 cm respectively; b) Basin subsidence calculated from differential laser scans and fault interpretation in top view; c) Basin geometry at the end state of experiment.

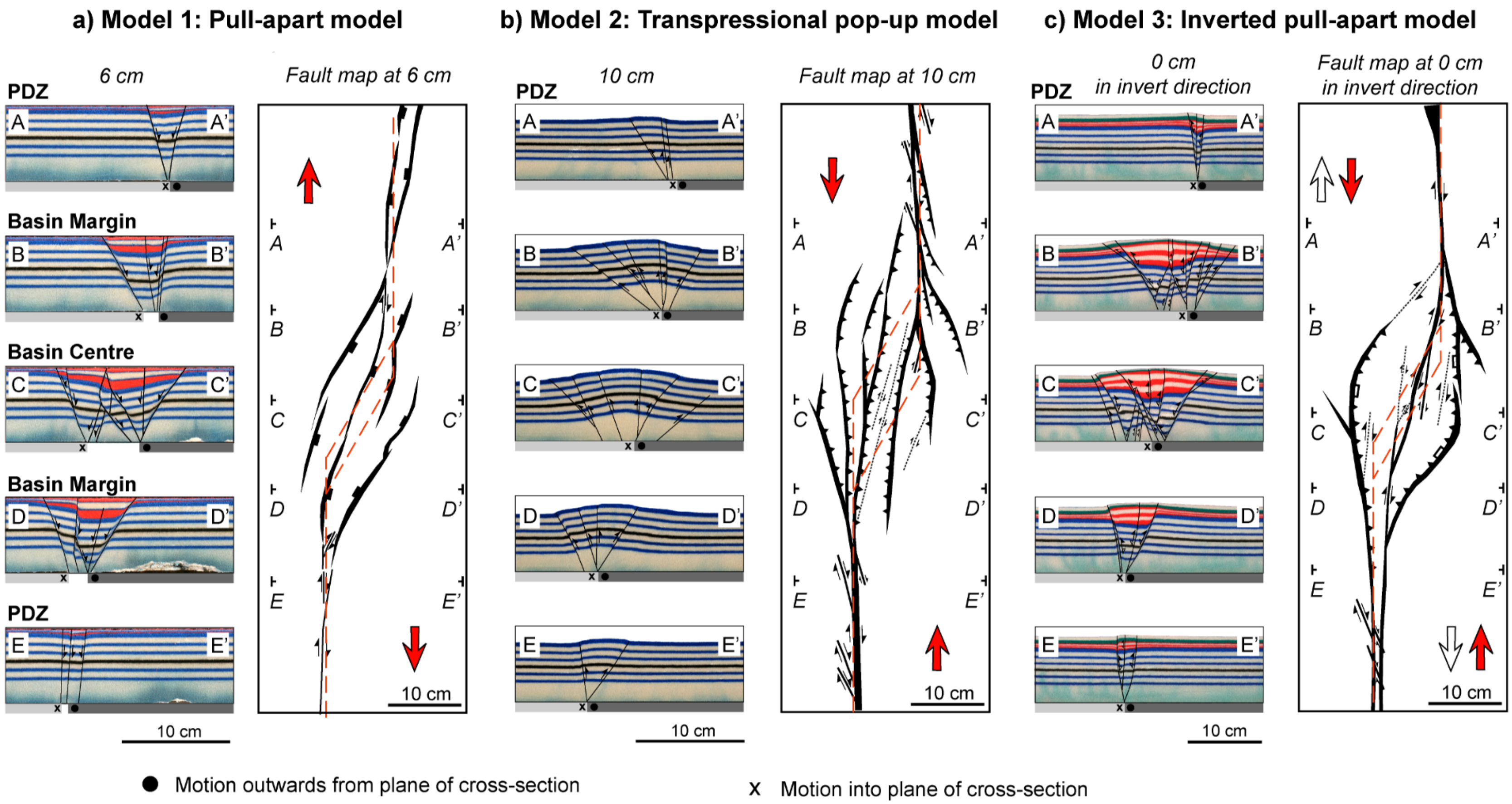

Figure 3.5 Vertical sections of the model 1: pull-apart model, model 2: transpressional pop-up model, and model 3: inverted pull-apart model. For each sandbox model a) Vertical section from north to south with fault interpretation and b) Fault geometry at final state are shown.

Transpressional pop-up model 2

Model 2 was designed to generate characteristic fault patterns within an oblique convergent setting for comparison with the reference model 1 and the inverted pull-apart basin model 3. Similar to the other sandbox models, we focus our interpretation to the complex structural region above the stepover only. The evolution of the strike-slip transpressional pop-up model is illustrated in Figure 3.6. After 5 cm of sinistral strike-slip displacement along the master faults, strike-slip faults formed above the master faults (5 cm in Figure 3.6a, b). The strike-slip faults terminated and formed an anastomosing map view pattern near the intersection of the master faults with the restraining bend stepover (5 cm in Figure 3.6a, b). A broad rhomboidal, antiformal uplift was formed above the restraining bend (5 cm in Figure 3.6a, b). After 10 cm of strike-slip displacement along the master faults, the earlier-formed strike-slip propagated inwards across the stepover region and showed reverse fault slip (10 cm in Figure 3.6a, b). Further uplift occurred above the restraining bend (10 cm in Figure 3.6a, b). The final basin topography showed a broad uplift zone that was bounded by reverse faults (Figure 3.6c). The central uplift zone showed near-parallel reverse faults that were oriented at a lower angle than the basement stepover geometry (C-C’ in Figure 3.5b). Vertical cross-sections showed a pop-up structure that was formed by multiple reverse faults that had dips of 40° to 50° (C-C’ in Figure 3.5b).

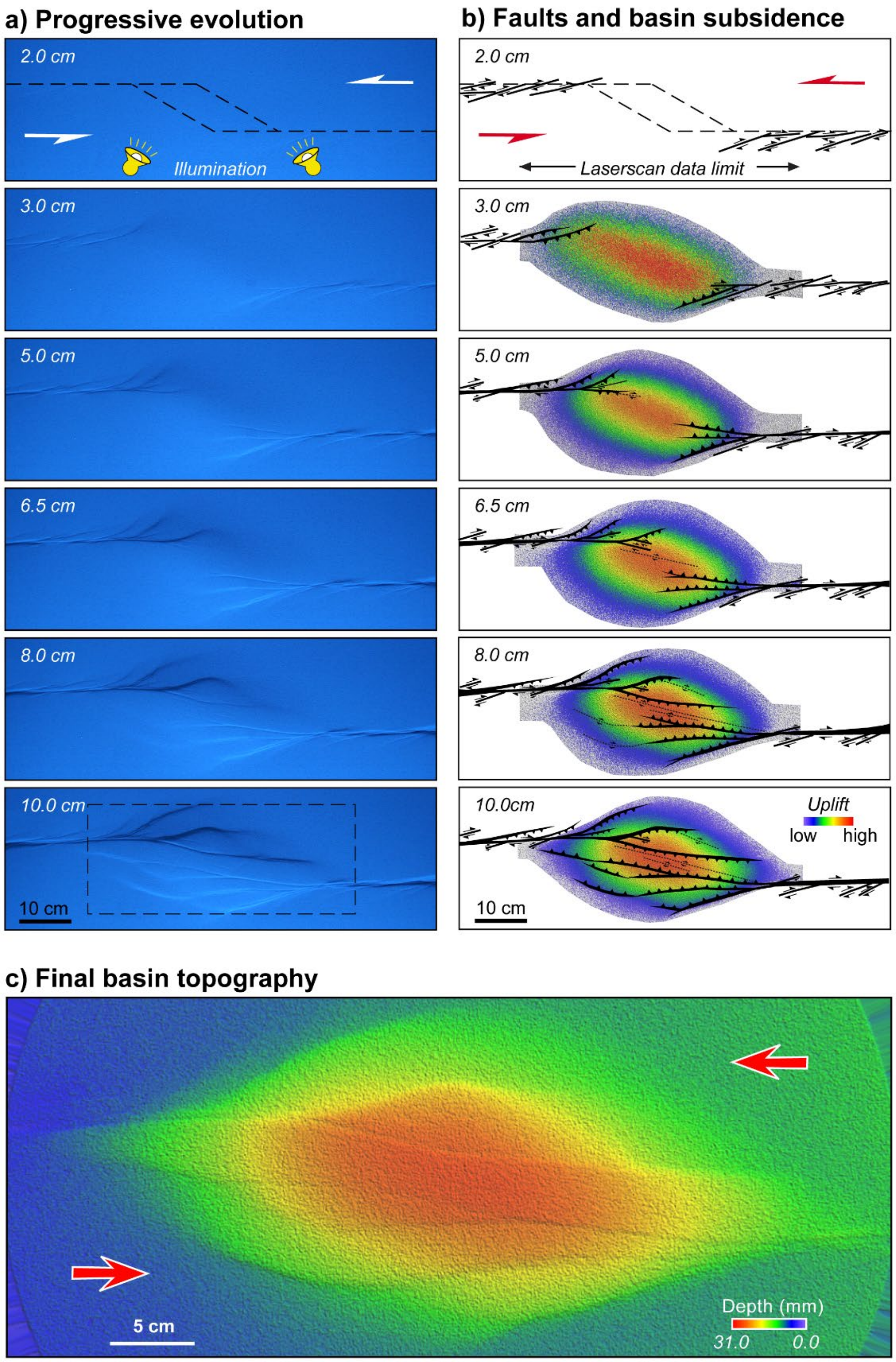

Figure 3.6 Plan view evolution of the transpressional pop-up model (model 2). a) Time lapse plan view photography from 1.4 cm to 6 cm respectively; b) Basin subsidence calculated from differential laser scans and fault interpretation in top view; c) Basin geometry at the end state of experiment.

Inverted pull-apart basin model 3

The evolution of the inverted pull-apart basin model 3 illustrated in Figure 3.7. In this model, 10 cm of transtension along the master faults were first simulated and then followed by 10 cm of transpression. Syn-extension and syn-inversion sand layers were infilled during the experiment. After 10 cm of horizontal displacement along the master faults or the end of transtension stage, a rhomboidal basin bordered by extensional faults was formed (Figure 3.7) that showed similarities to the reference pull-apart model 1 (Figure 3.4). After 5.4 cm of tectonic inversion, a rhomboidal antiformal uplift was formed that was bounded along its longitudinal margins by reverse faults (Figure 3.7a). A sinistral strike-slip fault cut across the pop-up center that linked the two offset PDZ (principal displacement fault) zones together (Figure 3.7b). Continued inversion of the 10 cm horizontal displacement along the master faults in the inverted movement produced “footwall shortcut” faults that propagated outside of the main bounding faults (Figure 3.7a, b 0.0 cm inverted horizontal displacement). The footwall shortcut faults essentially expanded the antiform size because these faults formed outside of the basin that developed during the pull-apart stage (Figure 3.7b). Shorter strike-slip fault segments were also formed within the antiformal uplift above the stepover region (Figure 3.7a, b).

The final basin topography showed a broad uplift zone that was bounded by reverse faults (Figure 3.7c). An array of strike-slip faults cut through central antiformal uplift and linked two PDZ zones together (Figure 3.7c). Vertical cross-sections revealed uplifted syn-extensional strata bounded by inverted normal faults (Figure 3.5c C-C’). Thinned syn-inversion strata above the basin center showed evidence of late uplift (Figure 3.5c C-C’). Footwall shortcut faults were revealed by the reverse faults that propagated outside of the syn-kinematic sand layers (i.e. red and white layers) (Figure 3.5c B-B’ and C-C’). The inverted normal fault showed steep dips of 50° to 75° within the syn-extensional layers and gentler dips of 40° to 50° within the syn-inversion layers (Figure 3.5c C-C’).

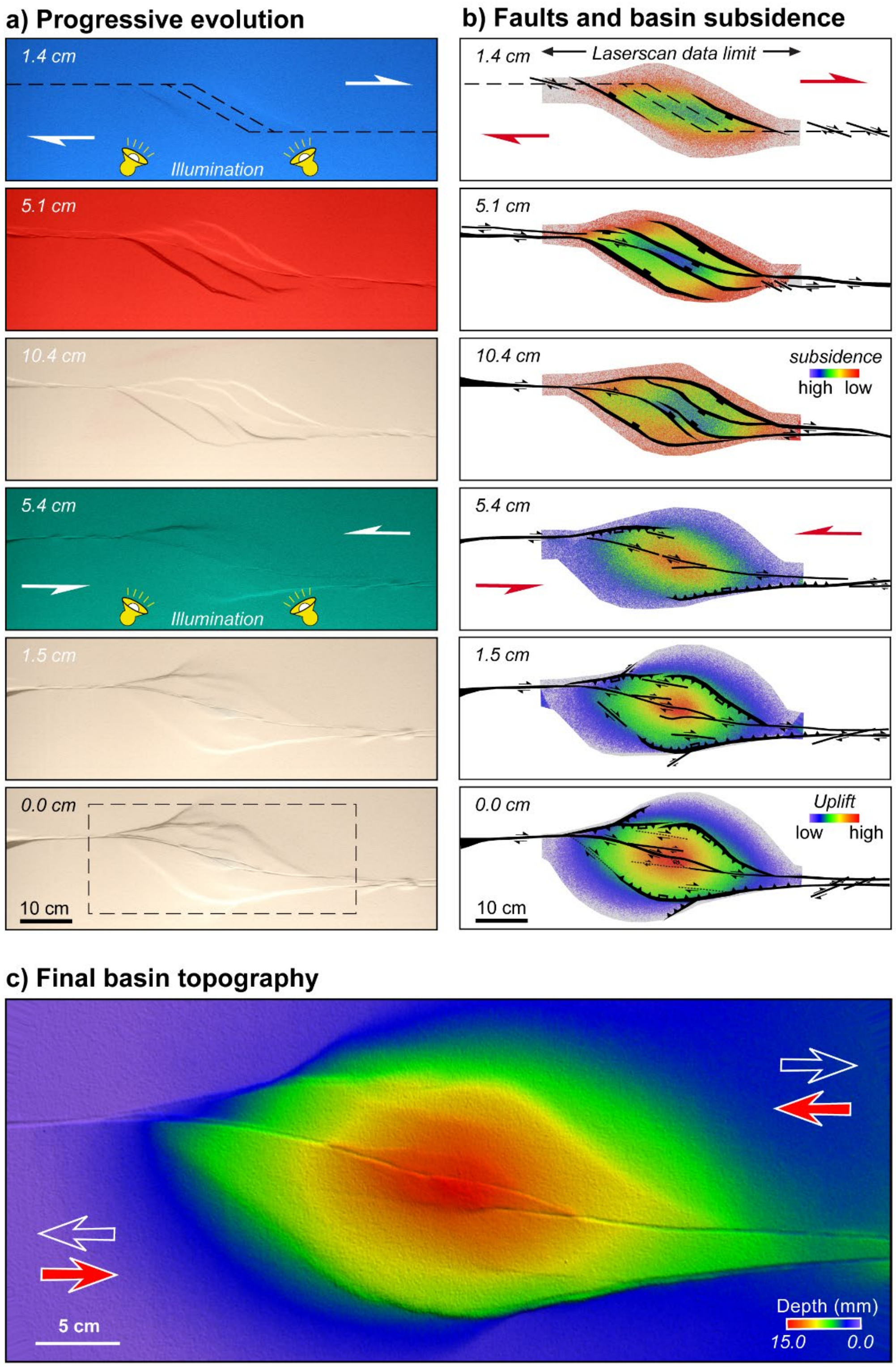

Figure 3.7 Plan view evolution of inverted pull-apart model (model 3). a) Time lapse plan view photography; b) Basin subsidence calculated from differential laser scans and fault interpretation in top view; c) Basin geometry at the end state of experiment.

3.3.2.Comparison between sandbox models

3D visualization of internal fault geometries

3D reconstruction of the three models from serial cross-sections allowed the three models to be visualized and compared (Figure 3.8 and Figure 3.9). The fault planes were colored by the fault depth. The vertical profile showed the cross-sections from the A to F location. The fault geometry was illustrated in Figure 3.10 with the fault planes colored by the depth color scale.

When comparing pre-kinematic section of pull-apart model (model1) with inverted pull-apart model (model3) (Figure 3.8a, b), the rhombohedral negative flower structure at the top pre-kinematic section of inverted pull-apart model was 1 cm wider at the pre-kinematic layer than the pull-apart model's pre-kinematic layer as shown in Figure 3.8a, b. Two depocenters were created in both models, however there were 16 more faults in the inverted pull-apart model than in the pull-apart model (C cross section in Figure 3.8a, b).

When compare pre-kinematic section of transpression pop-up model with syn-kinematic section of inverted pull-apart model (Figure 3.9a, b), the transpression pop-up model showed 6 cm wider shape than inverted pull-apart model. The total 23 faults in the inverted pull-apart model was higher than in transpression pop-up model. The pop- structure showed 0.80 cm greater uplift in transpression pop-up model relative to the inverted pull-apart model (Figure 3.9a, b).

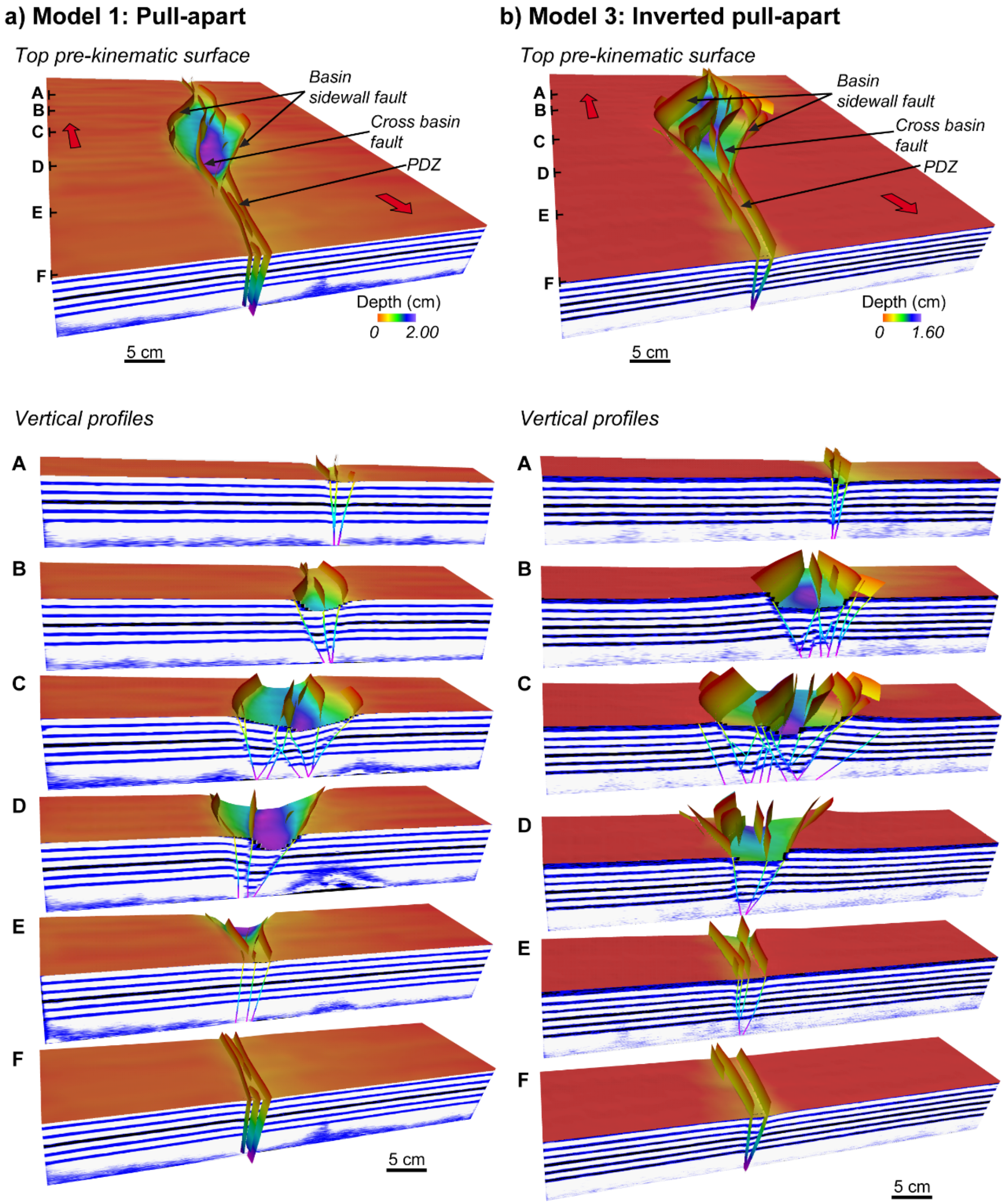

Figure 3.8 3D visualization showing a comparison of a) reference pull-apart basin Model 1 and b) inverted pull-apart basin Model 3. Each model is shown with 3D visualization of the sandbox with the top pre-kinematic section (top), and an exploded view of the vertical sections A-F (base). The fault interpretation was colored by fault depth.

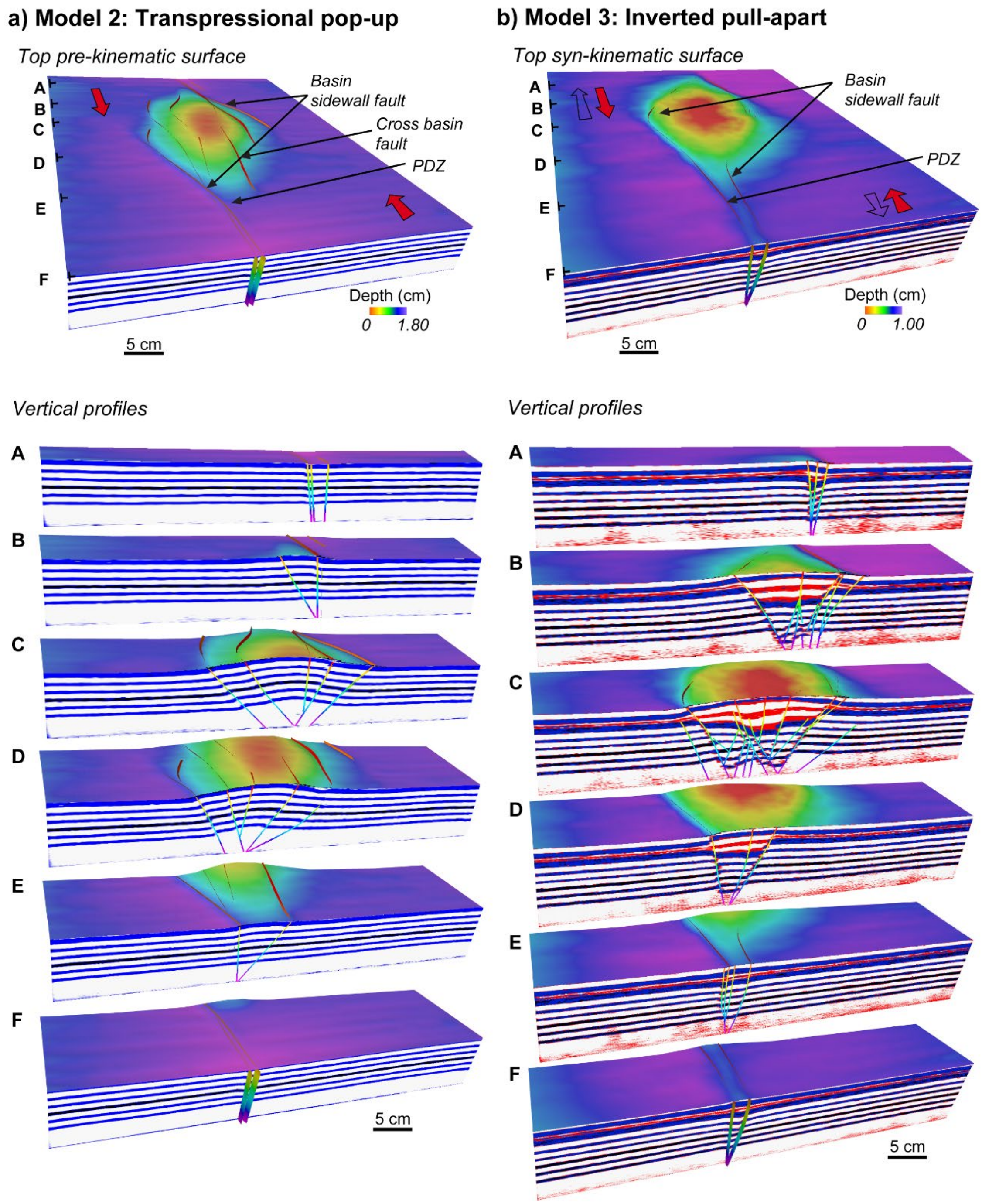

Figure 3.9 3D visualization showing a comparison of a) transpressional pop-up Model 2 and b) inverted pull-apart basin Model 3. Each model is shown with 3D visualization of the sandbox with the top pre-kinematic section (top), and an exploded view of the vertical sections A-F (base). The fault interpretation was colored by fault depth.

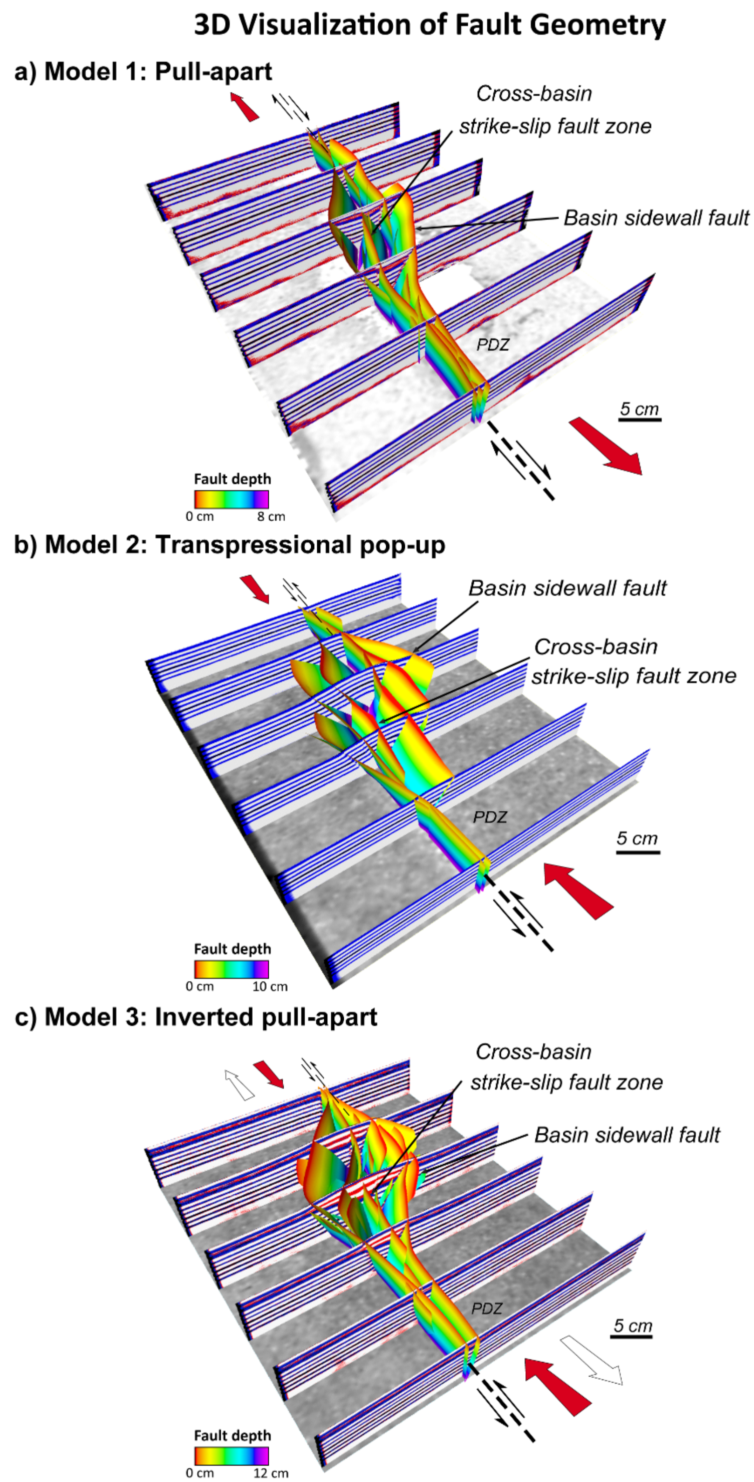

Figure 3.10 3D visualization showing fault geometry colored by fault depth for all three models: a) Pull-apart model 1; b) Transpressional pop-up model 2; c) Inverted pull-apart model 3.

Fault dip angle analysis

The fault dip angles of three models were displayed in Figure 3.11. All the models showed the basin boundary faults that had gentler dip angles than the interior basin faults. In all models the cross-basin faults showed steeper dip angles (dips >75°) than the basin border faults, which had 50° to 60° dips (Figure 3.11a). The strike-slip faults formed above the master PDZ faults showed steep dip angles (>80° dips). The pull-apart model generally showed higher dip angle faults than the other models. The inverted pull-apart model showed convex-upward inverted normal faults that had gentler dip angles within syn-kinematic to syn-inversion strata (dips <40°), and higher dip angles within the pre-kinematic strata (dips >60°) (Figure 3.11c). A number of lower angle "footwall shortcut" faults that propagated outside of the main bounding faults in the inverted pull-apart model (Figure 3.11c). The transpression model showed the gentlest dip angles among the three models (Figure 3.11c).

Fault azimuth analysis

The fault azimuth and dip direction/dip angle data of the three models were plotted within rose diagrams (Figure 3.12). The fault data were sampled at 4 cm longitudinal increments across the models. The pre-kinematic section of the pull-apart model showed azimuths that varied in 0° to 35° relative to the master fault orientation directions and maximum at the 0° (N - S) orientation (Figure 3.12a Pre-kinematic). Within the syn-kinematic section of the pull-apart model, fault azimuths showed the same major azimuth orientations as in the pre-kinematic section (Figure 3.12b Pre-kinematic).

The transpression model 2 fault data was plotted in Figure 3.12II. The maximum azimuth of the transpression model was 335° to 15° relative to the master fault orientations (Figure 3.12).

The rose diagrams of inverted pull-apart model 3 were illustrated in Figure 3.12c. The pre-kinematic azimuths were varied from two populations of 0° - 5° and 35° - 40° relative to the master faults (Figure 3.12c Pre-kinematic). Two maximum azimuth directions; N - S and NE - SW were shown in this model. The syn-kinematic azimuths were 330° to 45° relative to the master fault orientation as shown in Figure 3.12c Syn-kinematic.

Active and inactive fault

The amount of active and inactive faults was analyzed. Inactive faults after 3 cm horizontal strike-slip displacement was colored by the red line in Figure 3.13a and b. The active fault which propagated through the top of syn-kinematic layer was highlighted in blue (Figure 3.13a and b). The sandbox cross section was illustrated with interpretation in Figure 3.13c. A line drawing schematic of the same cross section is shown in Figure 3.13d. The total amount of inactive faults in the Inverted pull-apart model 3 was higher than the pull-apart model 1. During the inversion phase, a number of faults in Model 3 were abandoned (i.e. became inactive) due to development of a throughgoing cross-basin strike-slip fault (Figure 3.7). In contrast, Models 1 and 2 did not form throughgoing cross-basin strike-slip faults (Figure 3.4, 3.6). Therefore, it seems that basin inversion could potentially lead to hard linkage of some faults and abandonment of other faults (Figure 3.13).

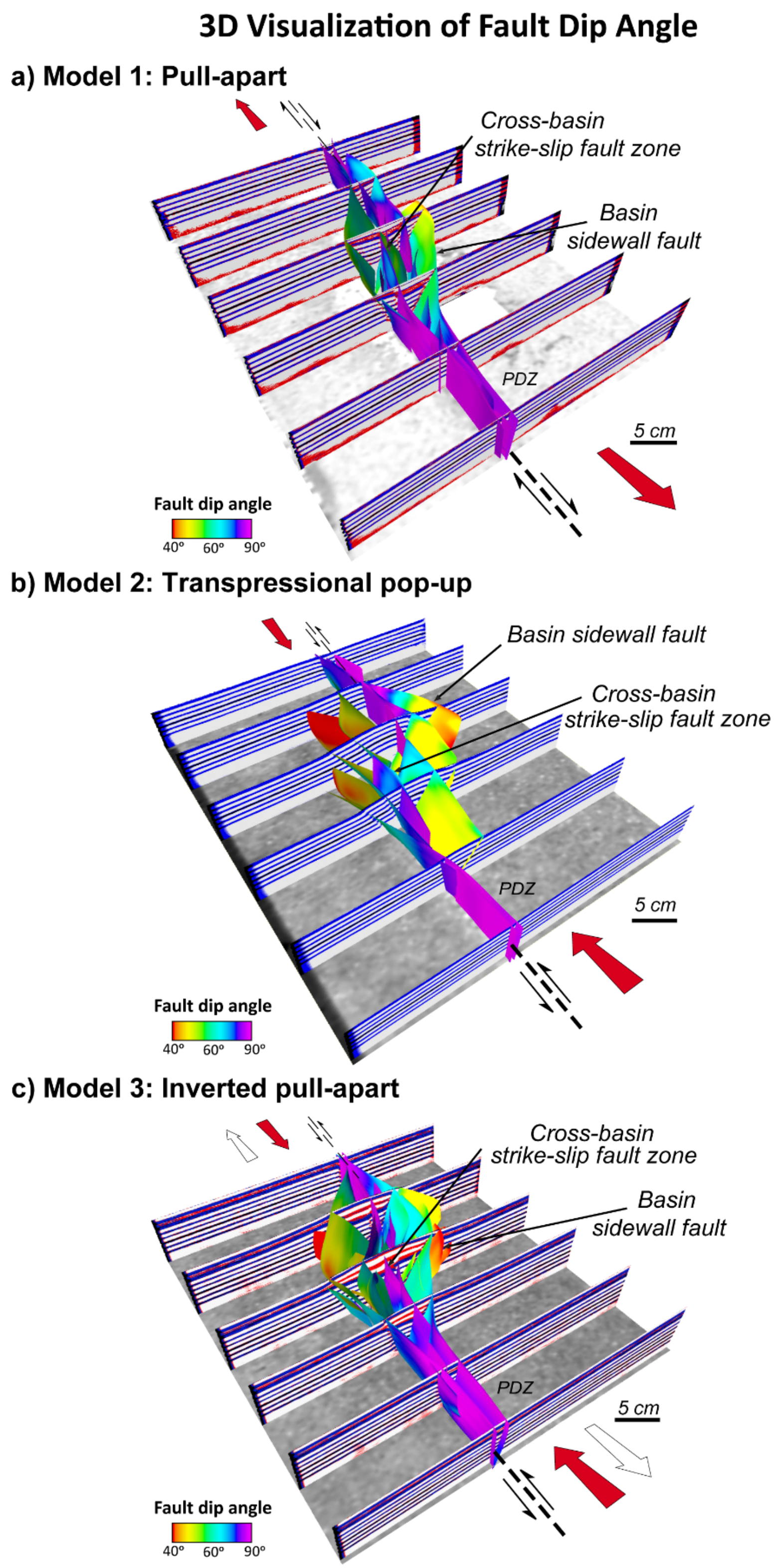

Figure 3.11 3D visualization of fault geometry colored by fault dip angle for a) Pull-apart model 1; b) Transpressional pop-up model 2; c) Inverted pull-apart model 3.

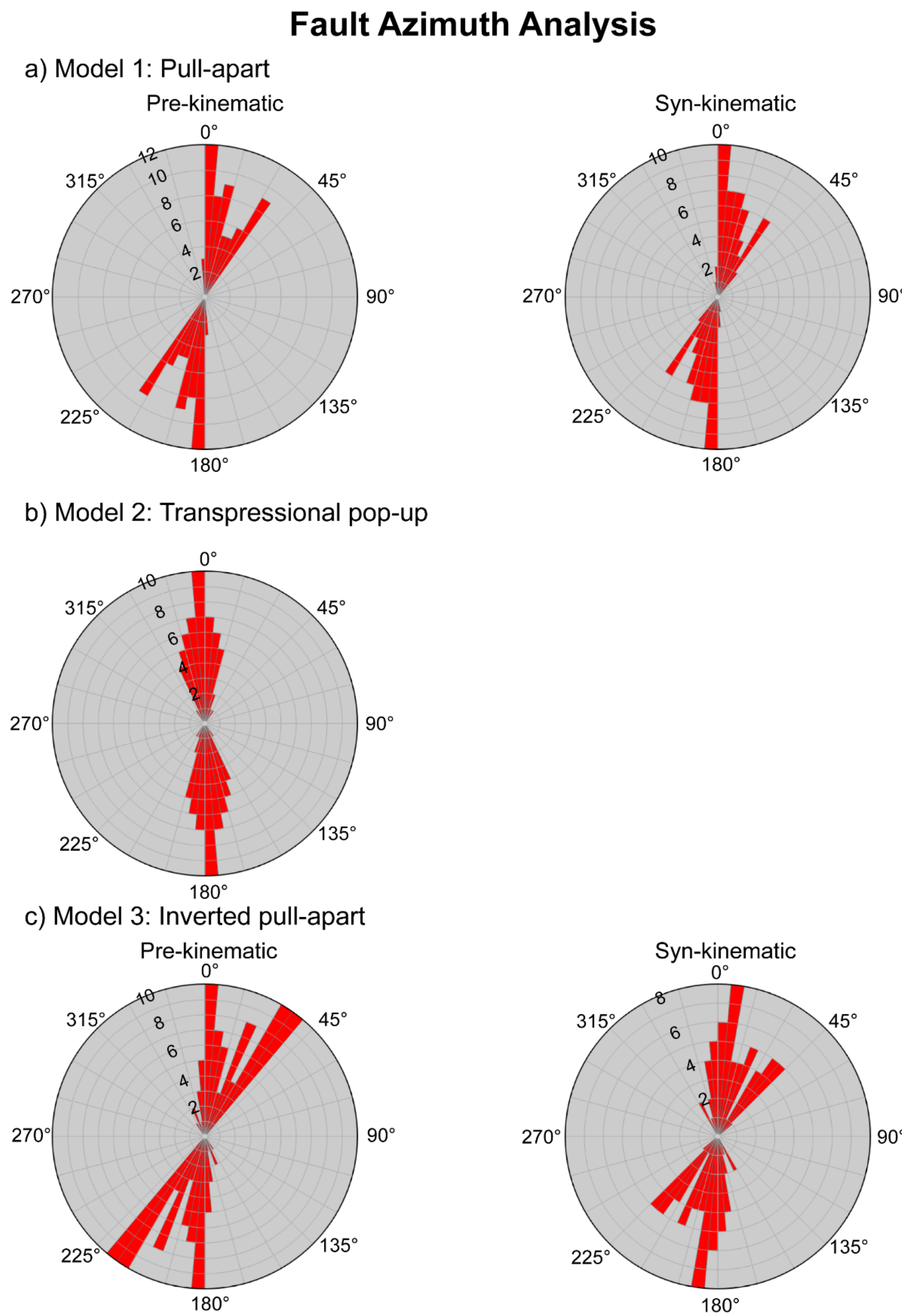

Figure 3.12 Rose diagram: a) Pull-apart model 1, b) Transpression pop-up model 2, and c) Inverted pull-apart model 3.

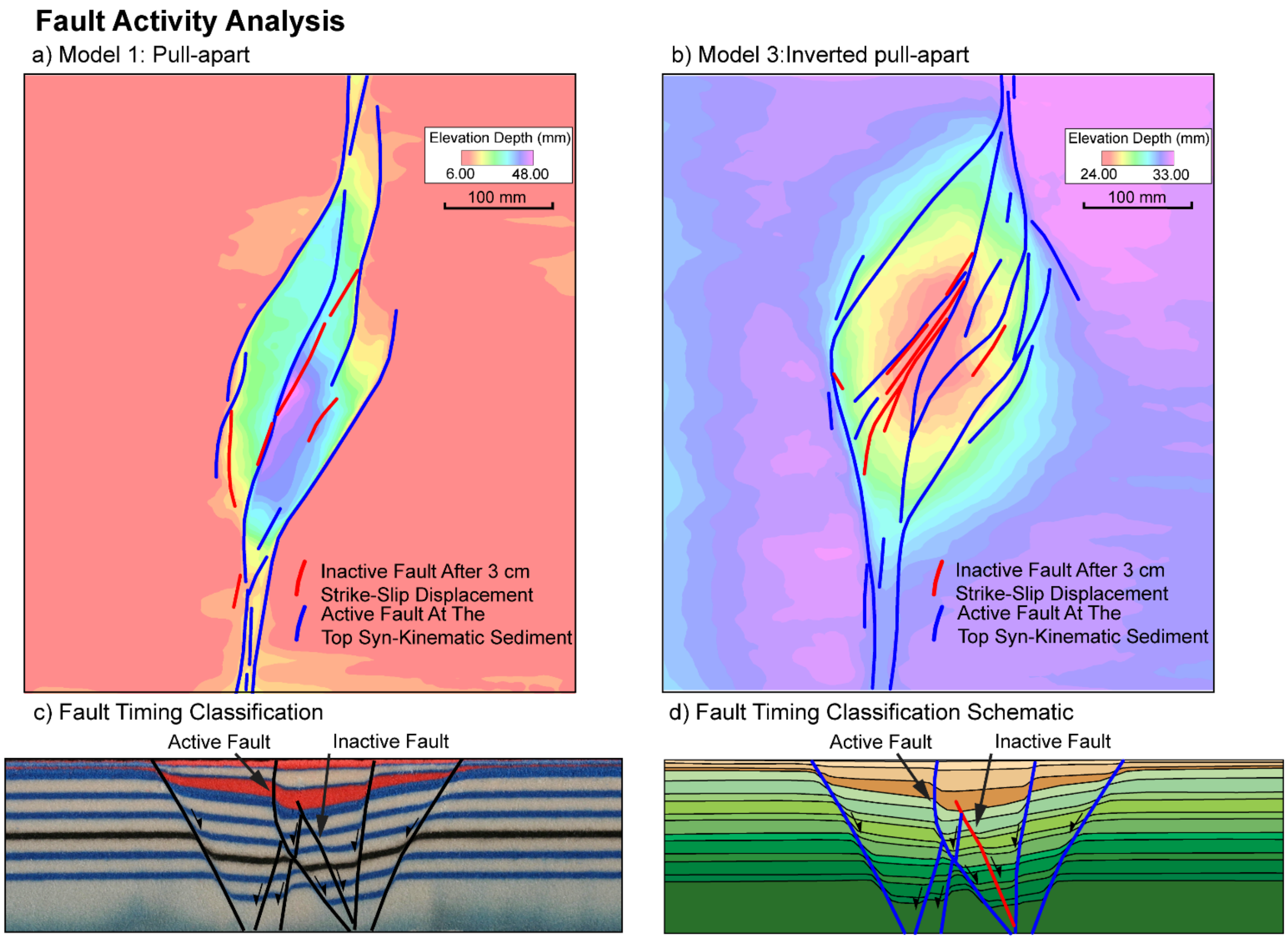

Figure 3.13 Inactive (red) and active (blue) faults analyzed from sandbox model growth strata for: a) Model 1: Pull-apart model and b) Model 3: Inverted pull-apart model. The model in b) produced an increased number of inactive faults relative to a). c) shows an example of the inactive and active fault analysis from growth strata of Model 1. d) shows a line drawing interpretation of c).

3.4 Summary of inverted sandbox model results

- All three sandbox models produced rhomboidal strike-slip basins that were bordered by oblique extensional or oblique compressional faults (Figure 3.4c; 3.6c; and 3.7c).
- The inversion key features could be observed in Model 3 are footwall shortcut faults (Figure 3.5cl C-C'), pop-up structure across the basin area (Figure 3.5c and Figure 3.7b), and normal reverse faults (Figure 3.5c and Figure 3.9b vertical profile c).
- There were 3 main key features of model 3 which different from model 1 and model 2.
  - Fault Dip angle: The variation of fault dip angle in the deep through shallow sediment were observed in Model 3 (Figure 3.11c). On the other hand, Model 1 showed steep dip angle pattern and Model 2 (Figure 3.11a) showed gentler dip angle pattern (Figure 3.11b).
  - Dominance azimuth pattern: There were two populations of dominance azimuth in the pre-existing pull-apart section of Model 3 (Figure 3.12c) while Model 1 and Model 2 showed a single dominance azimuth (Figure 3.12a and b).
  - Amount of inactive fault: There was a significant increasing of inactive fault in model 3 when compare to Model 1 (Figure 3.13).

3.5 Discussion

3.5.1.Inversion systems in inverted strike-slip basins

To identify inversion criteria, three sandbox models; transtension, transpression, and inverted, transtension were analyzed and compared. The transtension model or model 1 showed a narrow rhomboidal basin shape, less complex structure, steep dip angle faults, and one dominant fault azimuth population in the pre-kinematic section (Figure 3.8a). The transpression model or model 2 showed a wider pop-up structure shape, more complex structures, low angle thrust faults, and one dominance fault azimuth population (Figure 3.9a). Compare of these two reference models with the inverted pull-apart model or model 3 revealed the effects of pull-apart basin inversion (Figure 3.8b and 3.9b). The first criteria were the basin shape was wider after applied the inversion on the transtension model (Figure 3.8 and 3.9). The inverted zone showed the pop-up area and expanded out of the existing basin boundary as shown in Figure 3.5. The basin of the model showed approximately 0.8 cm wider than the model 1. The complexity also considered to be the second inversion criteria. The model 3 showed higher complexity of fault structure than the model 1 and model 2. There was an increase of approximately 16 in model 3 as demonstrated in the Figure 3.7. The third significant were the variation of fault dip angle pattern. The model 3 showed variation between fault dip angle in the deeper zone and shallower zone. The steep dip angle was generally present in the deep zone and the gentler dip angle were dominant in the shallower zone as illustrated in Figure 3.8. Moreover, the last inversion criteria was the dominant fault azimuth directions. The dominant azimuths of pre-kinematic and syn-kinematic section were analyzed. Both of model 1 and model 2 showed only one major azimuth in the pre-kinematic or pre-existing fabric. When compared the dominance azimuth results to model 3, the major azimuth pattern illustrated the difference. The model 3 showed 2 population of dominance azimuth in the pre-existing fabric. There were populations of 0° - 5° and 35° - 40° clockwise azimuths; therefore, model 3 showed aspects of dominant fault azimuths from both model 1 and model as illustrated in the Figure 3.9.

3.5.2.Comparison to inverted rift basin sandbox models

To identify the inversion effect criteria, the two inverted models were analyzed to indicate the significance inversion criteria. The Inverted pull-apart was analyzed as showed in the Section 3.1 and 3.2. Another Inverted model was referenced from Amilibia *et al*. (2005) who performed the Inverted 70° oblique half-graben. These two models were simulated 100% inversion displacement. The two models showed almost the same inversion criteria presence in the models. the first obvious criteria across these two models was the pop-up structure which was created at the central part of the PDZ. The second criteria were development of soft linkage of the thrust fault within the model. According to Amilibia *et al*. (2005), increased of inversion shortening lead to increase the development of the thrust fault soft linkage. The same result; development of soft fault linkage, was also presented in this study as in Figure 3.4 0.0 cm of inversion displacement. The third shared inversion criteria were the footwall shortcut faults developed outside the basin boundary fault. The footwall shortcut faults were obvious observed in the Inverted 70° oblique half-graben system experiment (Amilibia *et al*., 2005). According to Amilibia *et al*. (2005), the inversion occurred partially in the steep dip angle fault such as the basin boundary fault showed only partially inverted. Then the low angle thrust faults were created as footwall shortcut faults and cut through the pre-existing extensional fault. The footwall shortcut faults were obvious observed in the model 3; inverted pull-apart model in this study as shown in Figure 3.2. These footwall shortcut fault also expanded the basin shape and made the basin wider as showed in Figure 3.5 and 3.6 cross section.

Apart from the same criteria across these two inverted models, there are interesting quantitative criteria of inversion effect presented in this study. The first quantitative analysis showed variation of fault dip angle as the steep dip angle (dips >60°) in a deeper part and gentler dip angle (dips <40°) in the shallower part as show in Figure 3.8. The second is an increase of fault dominance azimuth within the pre-kinematic or pre-existing pull-apart part as shown in Figure 3.9. The last quantitative analysis on inversion criteria was an amount of inactive fault in the pre-kinematic or pre-existing pull-apart section. The total amount of inactive fault in the pre-kinematic section was increase when compare the pull-apart model (model 1) and Inverted pull-apart model (model 3) as shown in Figure 3.10. These three main criteria could be used to identify the inversion effect on a natural basin.

3.5.3.Summary and conclusions

- Similarities between inverted pull-apart (this study) and inverted 70° oblique half-graben experiment (Amilibia *et al*., 2005) include: a) Uplift of the central part of the basin, b). Soft linkage of the thrust faults as shortening increases, and c). Presence of footwall shortcut faults outside of the basin boundary faults. The main differences between inverted pull-apart basins from this study and inverted rift basins from published sandbox models are contrasted in Figure 3.14.

- Our new 3D structural analysis workflow for sandbox models enabled a more quantitative model analysis than traditional sandbox models. In particular, we were able to study; a) the variation of fault dip angles within the deep and shallow sediment, b) detect dominant fault azimuth populations, and c) interpret active and inactive faults in complex pull-apart basins using growth stratal analysis.

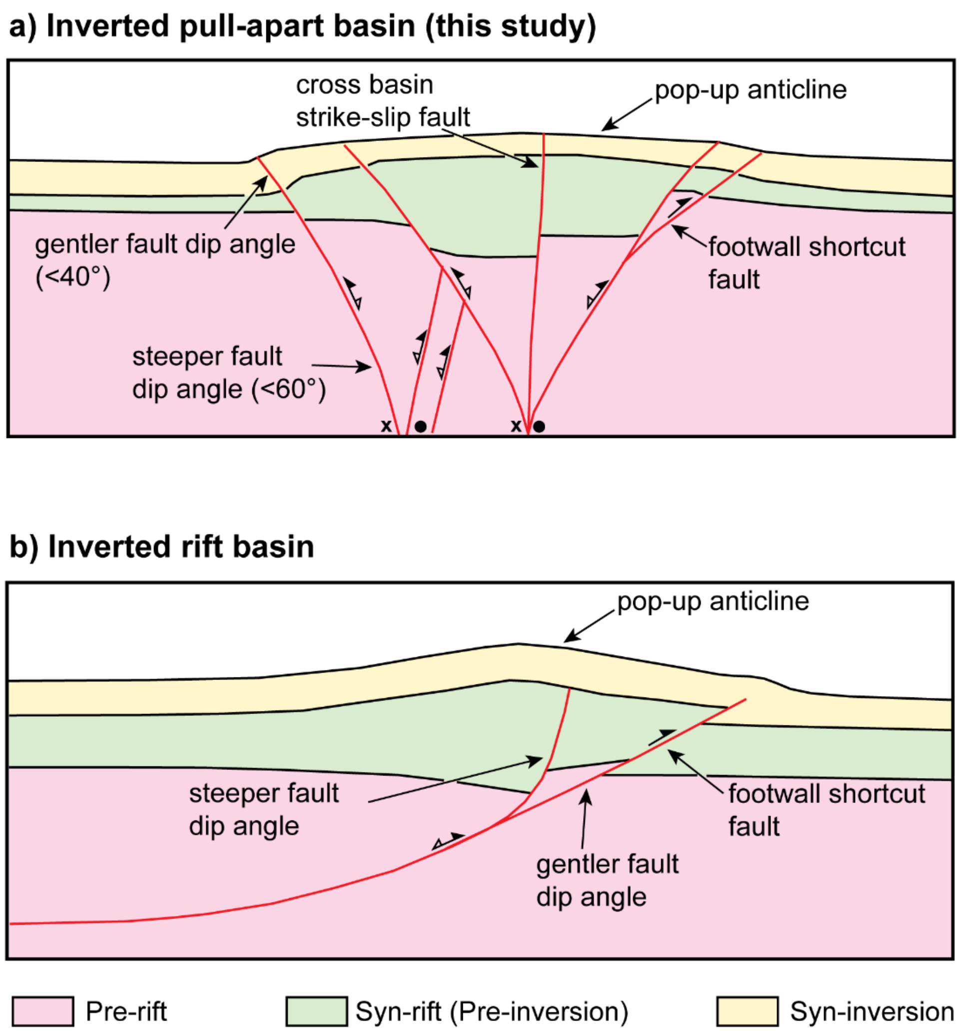

Figure 3.14 Summary diagram contrasting the key structural features formed in a) inverted pull-apart basins (this study) and b) inverted rifted basin which modified from Cooper and Warren (2010).

Chapter 4 Conclusion

According to the Phitsanulok basin tectonostratigraphic analysis (Study 1), we could conclude that:

- The Phitsanulok basin can be divided into a Northern and a Southern structural domain across 16°50'N latitudes based on structural styles, time structure maps, isochron maps, fault patterns, fault dip angles, fault throws, and fault azimuths,
- The southern limit of large natural earthquakes, earthquake hypocenter, and magnetic maps suggest the structural domains could be controlled by deep structures under the Phitsanulok basin. The structural boundary could indicate the southern extension or termination of the Sukhothai terrane and Nakhon Thai block basement under the Phitsanulok basin.
- Intense inversion and erosion in the southern domain south of 16°30'N latitudes could affect the hydrocarbon initially in place and well production performance.

According to the inverted pull-apart sandbox model analysis (Study 2), the follow conclusions could be observed:

- Inverted pull-apart basins form rhomboidal basins that host complex border faults and a throughgoing cross-basin fault system. 3D analysis of the internal sandbox model geometries using our newly developed workflow revealed two distinct fault azimuth populations (0° - 5° and 35° - 40°) relative to the master strike-slip faults, changes in fault dip angles, and increased inactive faults during pull-apart basin inversion.
- Our new workflow for analyzing the sandbox allows us to observe structural development in 3D thus introducing more quantitative methods for sandbox analysis. The more quantitative sandbox analysis could pave the way to more scientific comparisons between sandbox model and natural basin.
- Similar inversion characteristics between inverted pull-apart (this study) sandbox models and inverted rift basin (Amilibia *et al*., 2005) sandbox models include: a) Uplift of the

central part of the basin, b) Soft linkage of the thrust faults as shortening increases, and c) Presence of footwall shortcut faults outside of the basin boundary faults.

References

Amilibia, A., McClay, K. R., Sàbat, F., Muñoz, J., and Roca, E., 2005, Analogue modelling of inverted oblique rift systems: Geologica Acta, v. 3, no. 3, p. 0251-0271.
Bahae, W., 2017, structural evolution using section restoration, phitsanulok basin, central thailand [Master of Science: Chulalongkorn University, Thailand, 80 p.
Bal, A., Burgisser, H., Harris, D., Herber, M., Rigby, S., Thumprasertwong, S., and Winkler, F., The tertiary Phitsanulok lacustrine basin, Thailand, *in* Proceedings Proceedings of the National Conference on Geologic Resources of Thailand: Potential for Future Development. Department of Mineral Resources, Bangkok1992, Volume 247, p. 258.
Brooks, J., 1986, Development of the Sirikit Oil Field, Thailand.
Burchfiel, B., and Stewart, J., 1966, "Pull-apart" origin of the central segment of Death Valley, California: Geological Society of America Bulletin, v. 77, no. 4, p. 439-442.
Charusiri, P., 2002, Geotectonic evolution of Thailand: a new synthesis: Journal Geology Society Thailand, v. 1, p. 1-20.
Charusiri, P., and Pum-Im, S., 2009, Cenozoic tectonic evolution of major sedimentary Basins in Central, Northern, and the Gulf of Thailand: Bulletin of Earth Science Technology, v. 2, no. 1, p. 40-61.
Chopra, S., and Marfurt, K. J., 2007, Seismic attributes for prospect identification and reservoir characterization, Society of Exploration Geophysicists and European Association of Geoscientists and Engineers.
Cooper, M., and Warren, M. J., 2010, The geometric characteristics, genesis and petroleum significance of inversion structures: Geological Society, London, Special Publications, v. 335, no. 1, p. 827-846.
Cooper, M., Williams, G., De Graciansky, P., Murphy, R., Needham, T., De Paor, D., Stoneley, R., Todd, S., Turner, J., and Ziegler, P., 1989, Inversion tectonics—a discussion: Geological Society, London, Special Publications, v. 44, no. 1, p. 335-347.
Flint, S., Stewart, D., Hyde, T., Gevers, E., Dubrule, O., and Van Riessen, E., 1988, Aspects of reservoir geology and production behavior of Sirikit oil field, Thailand: An integrated study using well and 3-D seismic data: The American Association of Petroleum Geologists Bulletin, v. 72, no. 10, p. 1254-1269.
Fyhn, M. B., and Phach, P. V., 2015, Late Neogene structural inversion around the northern Gulf of Tonkin, Vietnam: Effects from right-lateral displacement across the Red River fault zone: Tectonics, v. 34, no. 2, p. 290-312.
Gomes, C. J., Danderfer Filho, A., Posada, A. M. A., and Da Silva, A. C., 2010, The role of backstop shape during inversion tectonics physical models: Anais da Academia Brasileira de Ciências, v. 82, no. 4, p. 997-1012.
Harding, T. P., 1985, Seismic characteristics and identification of negative flower structures, positive flower structures, and positive structural inversion: The American Association of Petroleum Geologists Bulletin, v. 69, no. 4, p. 582-600.
Knox, G., and L Wakefield, L., 1983, An Introduction to the Geology of the Phitsanulok Basin.
Lei, C., Ren, J., Sternai, P., Fox, M., Willett, S., Xie, X., Clift, P. D., Liao, J., and Wang, Z., 2015, Structure and sediment budget of Yinggehai–Song Hong basin, South China Sea: Implications for Cenozoic tectonics and river basin reorganization in Southeast Asia: Tectonophysics, v. 655, p. 177-190.
Mann, P., Hempton, M. R., Bradley, D. C., and Burke, K., 1983, Development of pull-apart basins: The Journal of Geology, v. 91, no. 5, p. 529-554.
McClay, K., 1989, Analogue models of inversion tectonics: Geological Society, London, Special Publications, v. 44, no. 1, p. 41-59.
McClay, K., and Bonora, M., 2001, Analog models of restraining stepovers in strike-slip fault systems: The American Association of Petroleum Geologists bulletin, v. 85, no. 2, p. 233-260.
McClay, K., and Dooley, T., 1995, Analogue models of pull-apart basins: Geology, v. 23, no. 8, p. 711-714.

McClay, K., and Ellis, P., 1987, Geometries of extensional fault systems developed in model experiments: Geology, v. 15, no. 4, p. 341-344.
Morley, C., 2007, Variations in late Cenozoic–Recent strike-slip and oblique-extensional geometries, within Indochina: The influence of pre-existing fabrics: Journal of Structural Geology, v. 29, no. 1, p. 36-58.
Morley, C. K., 2017, The impact of multiple extension events, stress rotation and inherited fabrics on normal fault geometries and evolution in the Cenozoic rift basins of Thailand: Geological Society, London, Special Publications, v. 439, no. 1, p. 413-445.
Morley, C., Charusiri, P., and M Watkinson, I., 2011a, 1 Structural geology of Thailand during the Cenozoic Modern tectonic setting of Thailand, 273-334 p.:
Morley, C., Gabdi, S., and Seusutthiya, K., 2007, Fault superimposition and linkage resulting from stress changes during rifting: Examples from 3D seismic data, Phitsanulok Basin, Thailand: Journal of Structural Geology, v. 29, no. 4, p. 646-663.
Morley, C., Woganan, N., Sankumarn, N., Hoon, T., Alief, A., and Simmons, M., 2001, Late Oligocene–Recent stress evolution in rift basins of northern and central Thailand: implications for escape tectonics: Tectonophysics, v. 334, no. 2, p. 115-150.
Morley, C. K., 2009, Geometry and evolution of low-angle normal faults (LANF) within a Cenozoic high-angle rift system, Thailand: Implications for sedimentology and the mechanisms of LANF development: Tectonics, v. 28, no. 5.
Morley, C. K., 2015, Five anomalous structural aspects of rift basins in Thailand and their impact on petroleum systems: Industrial Structural Geology: Principles, Techniques and Integration, v. 421, p. 143.
Morley, C. K., Racey, A., Ridd, M., Barber, A., and Crow, M., 2011b, Tertiary stratigraphy: The geology of Thailand: The Geological Society (London), p. 223-272.
Pailoplee, S., 2014, Earthquake Catalogue of the Thailand Meteorological Department—A Commentary: Journal of Earthquake and Tsunami, v. 8, no. 05, p. 1471001-1.
Packham, G. H., 1993, Plate tectonics and the development of sedimentary basins of the dextral regime in western Southeast Asia: Journal of Southeast Asian Earth Sciences, v. 8, no. 1-4, p. 497-511.
Panien, M., Schreurs, G., and Pfiffner, A., 2005, Sandbox experiments on basin inversion: testing the influence of basin orientation and basin fill: Journal of Structural Geology, v. 27, no. 3, p. 433-445.
Polachan, S., Strikeslip tectonics and the development of Tertiary basins in Thailand, *in* Proceedings Proc. Int. Symp. Intermontane Basins: Geology and Resources. Chiang Mai1989, p. 243-253.
Polachan, S., Pradidtan, S., Tongtaow, C., Janmaha, S., Intarawijitr, K., and Sangsuwan, C., 1991, Development of Cenozoic basins in Thailand: Marine and Petroleum Geology, v. 8, no. 1, p. 84-97.
PTTEP, 1998, Sirikit structural study, PTTEP, p. 130.
PTTEP, 2015, Regional Mapping of S1 and L22/53 (Phase III), *in* HQ48149.1/2015, ed., PTTEP.
PTTEP, 2016, Sirikit Oil Filed Overview, PTTEP, p. 112.
PTTEP, 2017a, Annual Report: PTT Exploration and Production Pucblic Company Limited.
PTTEP, 2017b, S1 Stratigraphy Memorandum, PTTEP, p. 11.
PTTEP, 2018, Sandbox Modelling 2D and 3D analogue of Extensional Fault Strucutres, PTTEP, p. 31.
PTTEP, 2019, Sirikit Oil Field Production Data, PTTEP.
Pubellier, M., and Morley, C., 2014, The basins of Sundaland (SE Asia): evolution and boundary conditions: Marine and Petroleum Geology, v. 58, p. 555-578.
Rangin, C., Klein, M., Roques, D., and Le Pichón, X., 1995, The Red river fault system in the Tonkin Gulf, Vietnam: Tectonophysics, v. 243, no. 3-4, p. 209-222.
Richard, P., and Krantz, R. W., 1991, Experiments on fault reactivation in strike-slip mode: Tectonophysics, v. 188, no. 1-2, p. 117-131.
Ridd, M. F., Barber, A. J., and Crow, M. J., The Geology of Thailand2011, Geological Society of London.

Simons, W., Socquet, A., Vigny, C., Ambrosius, B., Haji Abu, S., Promthong, C., Subarya, C., Sarsito, D., Matheussen, S., and Morgan, P., 2007, A decade of GPS in Southeast Asia: Resolving Sundaland motion and boundaries: Journal of Geophysical Research: Solid Earth, v. 112, no. B6.

Sugan, M., Wu, J., and McClay, K., 2014, 3D analogue modelling of transtensional pull-apart basins: comparison with the Cinarcik basin, Sea of Marmara, Turkey: Bollettino di Geofisica Teorica ed Applicata, v. 55, no. 4.

Thai Shell Exploration and Production Co.Ltd, 1988, Hydrocarbon habitat of the Phitsanulok Basin: Thai Shell Exploration and Production Co.Ltd,.

Tingay, M. R., Morley, C. K., Hillis, R. R., and Meyer, J., 2010, Present-day stress orientation in Thailand's basins: Journal of Structural Geology, v. 32, no. 2, p. 235-248.

Wang, Q., Li, S., Guo, L., Suo, Y., and Dai, L., 2017, Analogue modelling and mechanism of tectonic inversion of the Xihu Sag, East China Sea Shelf Basin: Journal of Asian Earth Sciences, v. 139, p. 129-141.

Wu, J. E., McClay, K., Whitehouse, P., and Dooley, T., 2009, 4D analogue modelling of transtensional pull-apart basins: Marine and Petroleum Geology, v. 8, no. 26, p. 1608-1623.

https://earthquake.usgs.gov/earthquakes/browse/stats.php

APPENDIX

1. Import and create cube from sandbox model images workflow

To import a sandbox model images into Petrel software, the Cegal Blueback plug-in is needed to process. We acknowledge Cegal's generosity to grant us an educational Cegal Blueback license for this project. This workflow is based on Petrel version 2016 and Cegal plug-in version 2.0.4.184; it should be compatible with Petrel version 2017 as well. The process in this appendix section start by a set of sandbox .tiff image files. There are two main steps to import and create the seismic cube: a) Create a reference frame layout in Petrel software; b) Import sandbox images into Petrel software and create a seismic cube from the imported sandbox images. All the workflow was guided and suggested by the Schlumberger Customer Care Center team.

1.1. Create a reference frame layout in Petrel software

Open Petrel. Select Bundle 1, click to select and open all Blueback Toolbox plugins. Click OK.

Create a new project by clicking the icon under Projects menu. To create the reference frame in Petrel software, the Inlines layout from a seismic dummy cube is applied. The dummy cube is set up in the same ratio as the sandbox model in order to get a precise reference frame.

Step 1: Create a new seismic main folder by clicking "Folder" – New Seismic Main folder (Figure A.1.)

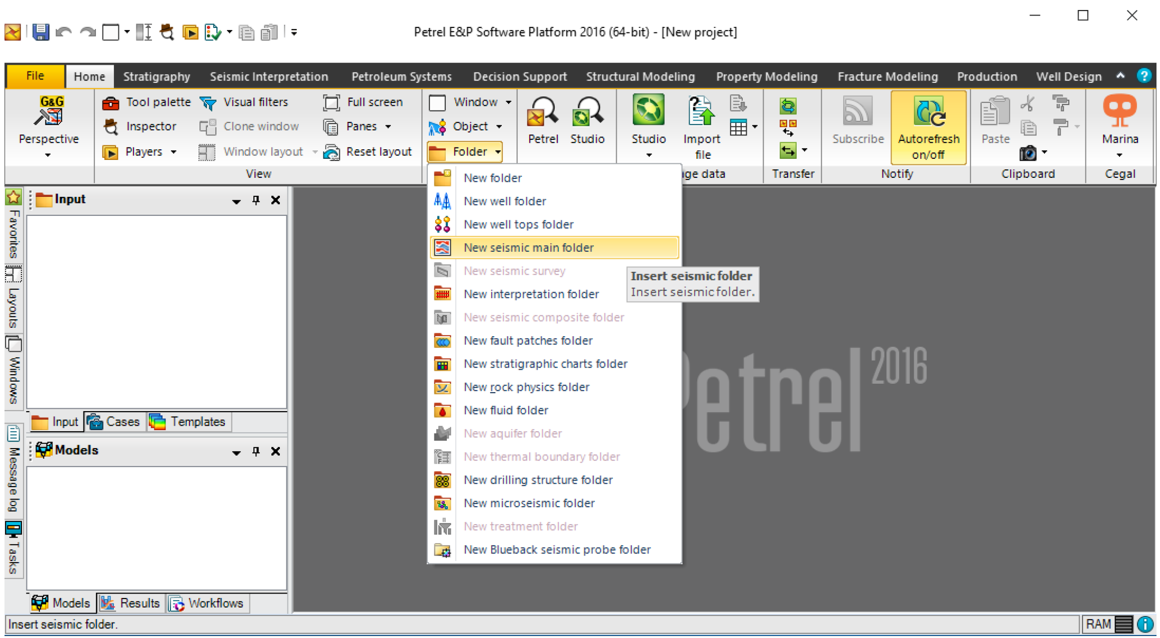

Figure A. 1 Step to insert new seismic folder into seismic main folder.

Step 2: Create a new seismic survey

Insert a new seismic survey inside the seismic main folder as in Figure A.2.

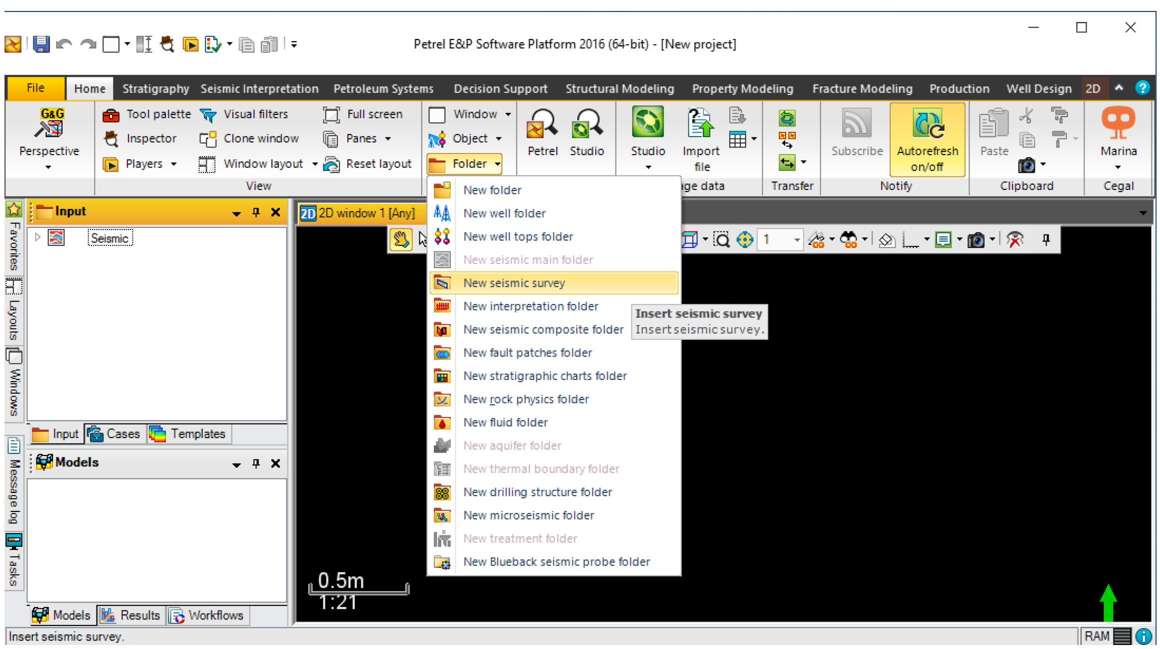

Figure A. 2 Step to insert new seismic folder into seismic survey folder.

Step 3: Create a dummy cube within the survey

Open the setting of the new seismic survey by expanded triangle in front of seismic icon and right click on the survey 1 as in Figure A.3. A warning message will popup that informs the user about coordinate systems. Click on the button to accept “Continue spatially aware”.

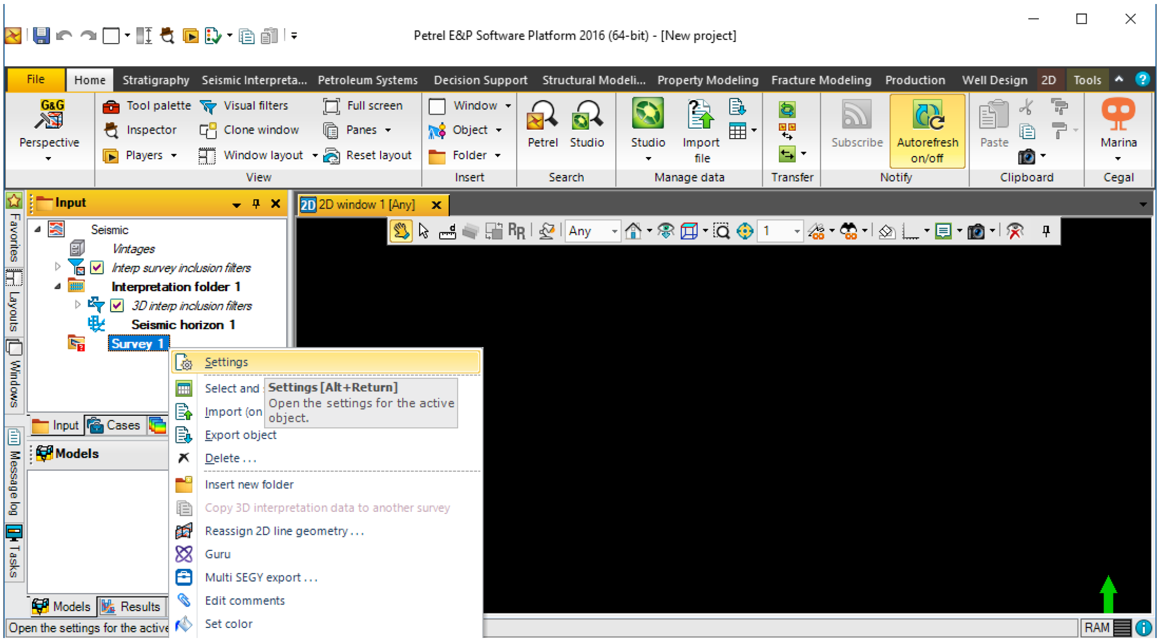

Figure A. 3 Step to Open the setting of the new seismic survey.

Set up the geometry for a new dummy cube, called ‘Survey 1’, in the setting menu. The window as in Figure A.4 will come up. Then click on define tab as in Figure A.4.

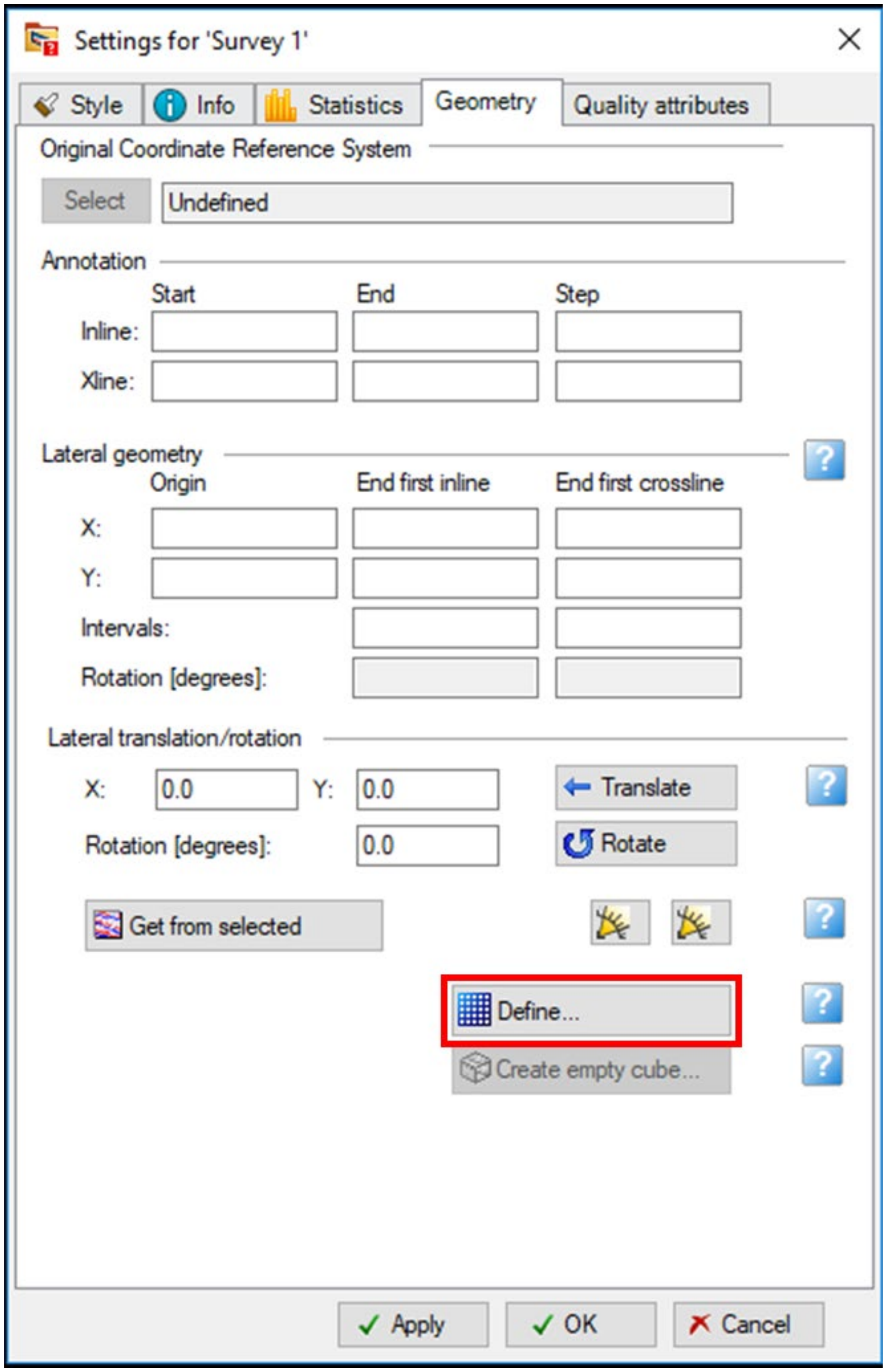

Figure A. 4 Geometry setting window for the dummy survey. The red rectangular shows define tab which is used to define the value for each sandbox model.

Before defining the X, Y, Inline, Xline and step value, the scaling of sandbox should be applied. In this project 1:100 was applied. So, 1 cm of the sandbox model equal 100 cm in Petrel software. Then put the right value which calculate from the ratio into the setting window (Figure A.5).

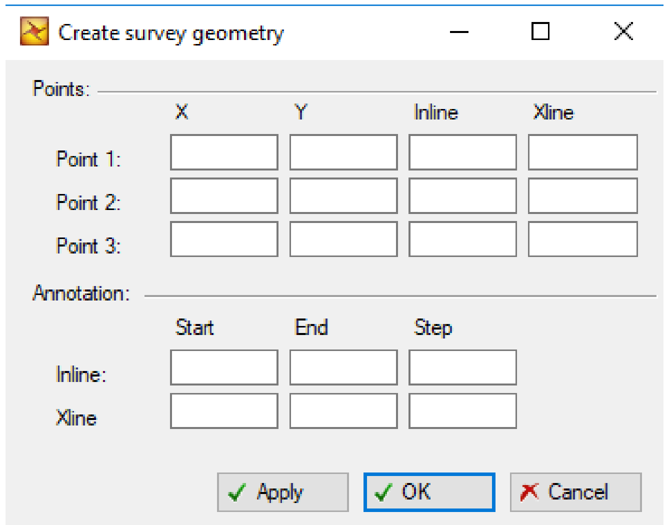

Figure A. 5 Create seismic geometry set up window.

Step to put number into the window in Figure A.5 are as follows:

a) Point 1, 2, and 3 are the control point for the dummy cube.

Table A. 1 Step to put the number into point value

Point	X	Y	Inline	Xline
Point 1	0	0	1	1
Point 2	0	5600*	1	100***
Point 3	5000**	0	140***	1

* Put on the total length of the sandbox model. For example, in this study the sandbox was 56 cm length, so the 5600 was put in the Y value.

** Put on the total width of the sandbox model. For example, in this study the sandbox was 50 cm width, so the 5000 was put in the X value.

*** Put on the total step which you want software to generate the Xline for sandbox seismic cube. In this project use total 100 for Xline.

**** Put on the total number of the sandbox images.

b) Inline and Xline are the seismic geometry of the dummy cube

Table A. 2 Step to put the number into Inline and Xline value

	Start	End	Step
Inline	1	140*	1
Xline	1	100**	1

* Put on the total number of the sandbox images.

** Put on the same value as Xline value (***) in Table A.1.

Then click OK on both seismic geometry window and geometry setting window. Then the QC step should be observed through the statistic as in Figure A.6. The main observation should make on the end of first Inline X and Xline Y. The results should be the same as the input set up.

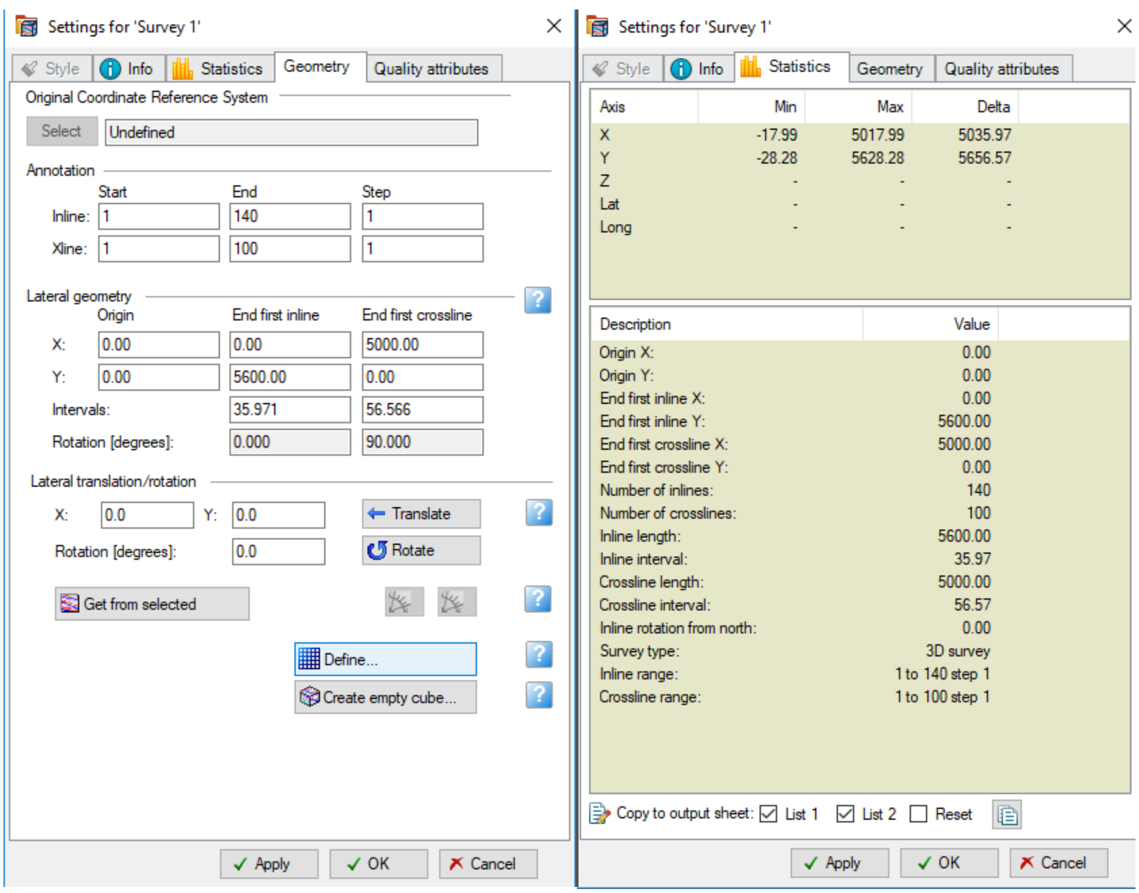

Figure A. 6 QC observation through the setting and statistic of the dummy cube.

Now click “Create empty cube…” on the Settings for Survey 1 menu (Figure A.7). Select “Elevation depth”, then enter 0, 4, 250, as below (Figure A.8). Then click OK.

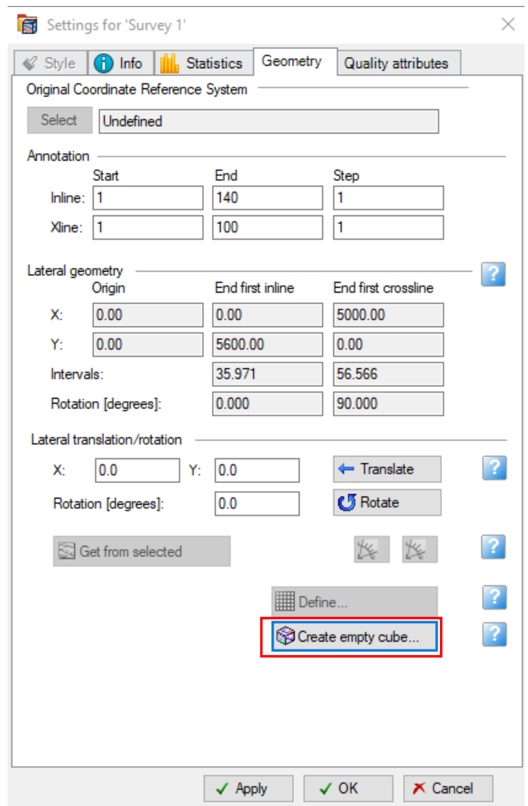

Figure A. 7 Step to create an empty cube.

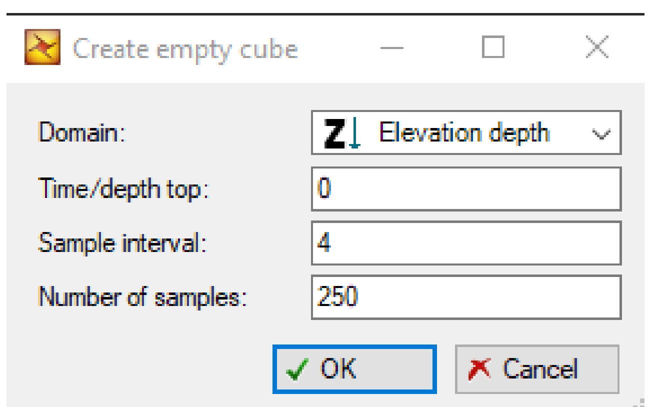

Figure A. 8 Input parameter for creating empty cube.

Step 4: Generate Inlines layout from the dummy cube

The Inlines layout, called 'polygon', will be derived from the dummy cube. The Inlines layout will be a references frame for sandbox image in the import step (see subsection 1.2). To generate the inline layouts, right click on the dummy cube, called the default name "Empty Cube 1". Select the "generate Inlines layout" as in Figure A.9. Then put the 1 in both white boxes in the generate seismic Inlines layout (Figure A.10).

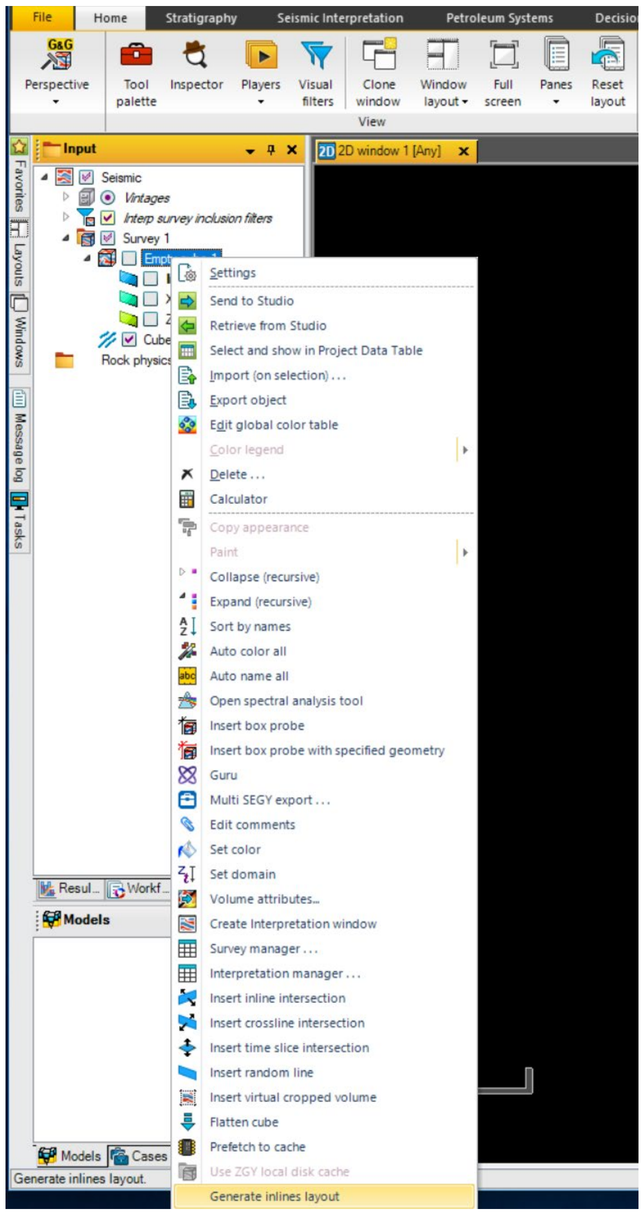

Figure A. 9 Step to generate Inlines layout.

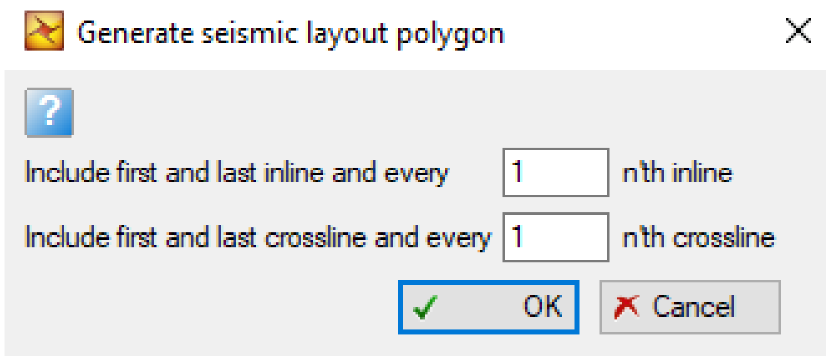

Figure A. 10 Generate seismic Inlines layout window. Put the 1 in both white boxes.

Split each Inline references frame by right click on the Inline layout. Right click "Cube layout Empty cube 1" as in Figure A.9. Select "Split" from the popup menu as in Figure A.11.

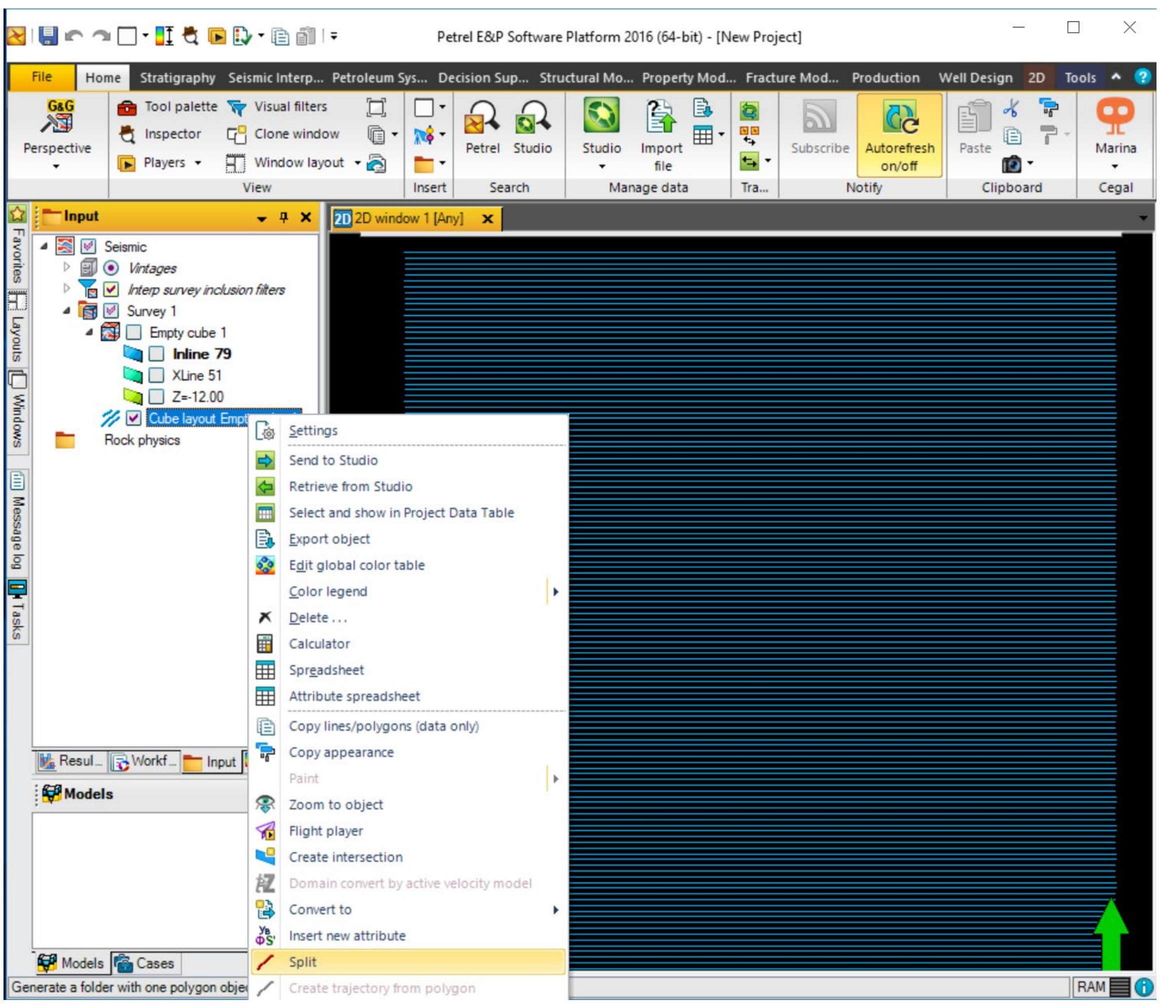

Figure A. 11 Step to split each Inline reference frame.

Results: each Inline are created and stored in polygon format inside the folder 'cube layout Empty cube 1' as in Figure A.12. Hence, in the import section, polygon 1, 2, 3, etc. are referred to the Inline reference frame.

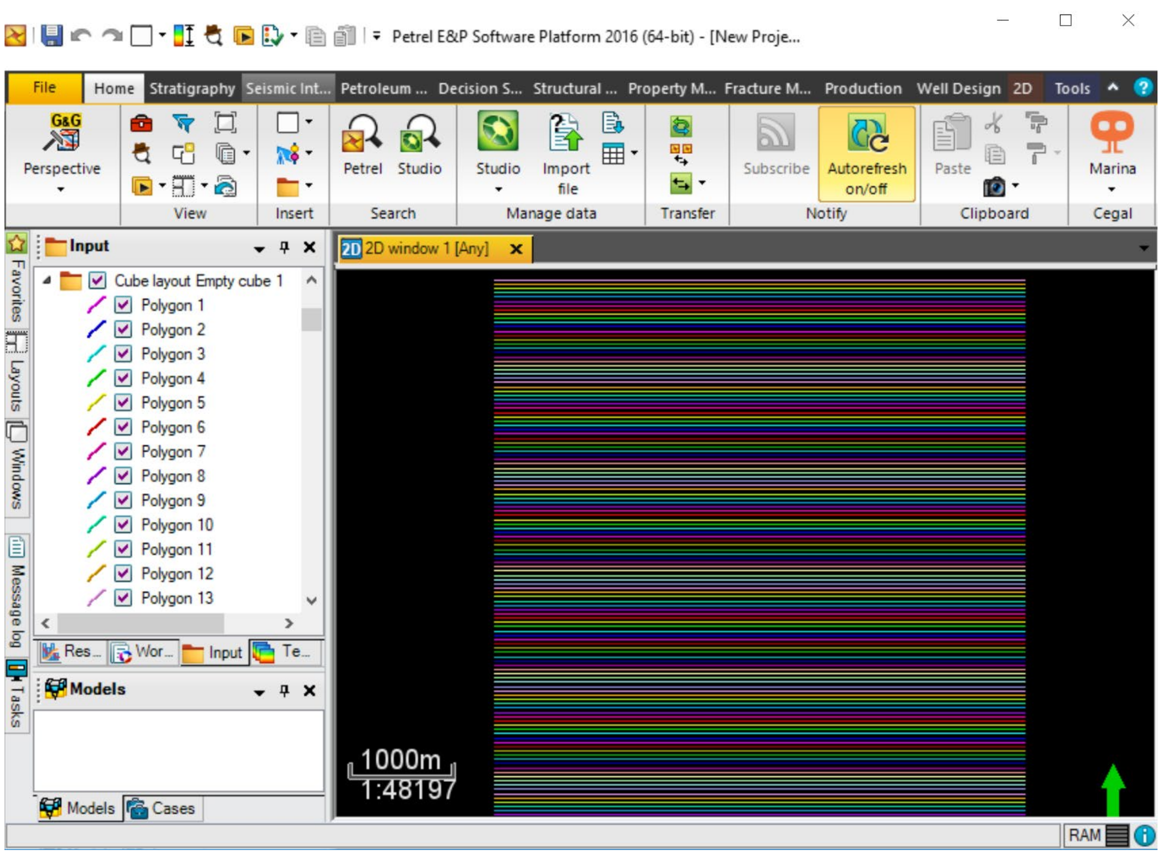

Figure A. 12 Final result for creating the Inline reference frame

1.2. Import sandbox images into Petrel software and create a seismic cube from the imported sandbox images

In order to import image into Petrel, the sandbox image should be prepared in a tiff file format.

Step 1: Import sandbox images into Petrel software

To import a sandbox tiff images into Petrel, a new empty seismic survey, called 'Survey 2' should be created. Click the "Folder" icon at the top menu, then "New seismic survey" (for reference, see section 1.1 step 1 to step 3 for a similar sequence).

In order to import the first sandbox image, the Polygon 1 (Inline reference frame 1) need to be highlighted as in Figure A.13.

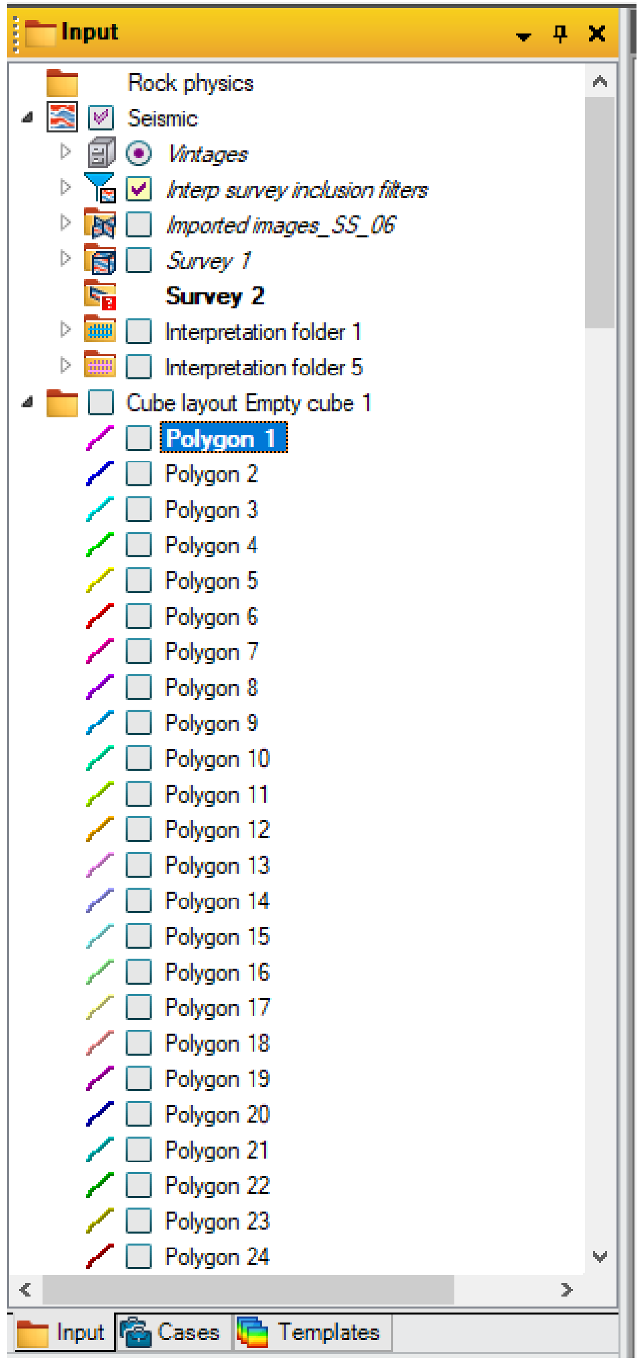

Figure A. 13 Step to highlight the Polygon 1 (Inline reference frame 1).

Then right click on the 'Survey 2' and select the import function as in Figure A.14.

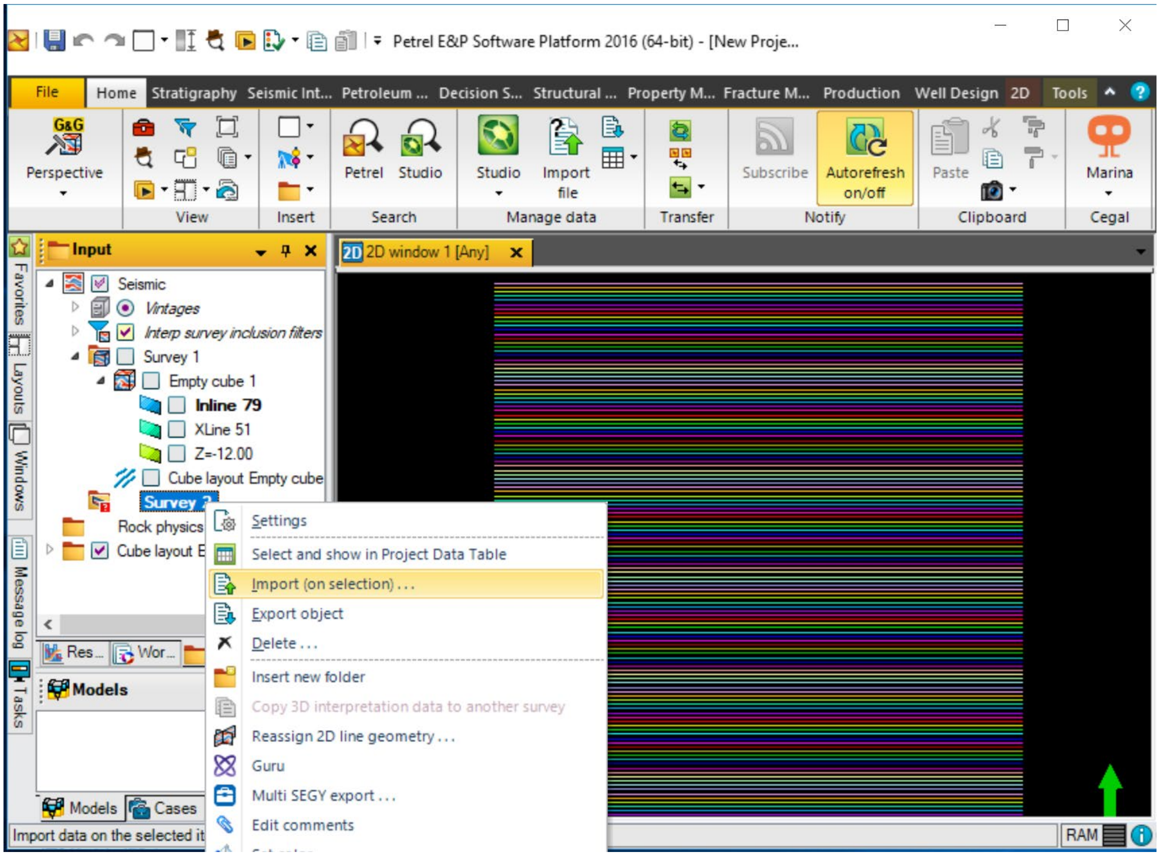

Figure A. 14 Step to import the .tiff file sandbox.

Go to the sandbox tiff file folder and select the first tiff file (Figure A.15). Ensure the “Files of type” shows “Image file loaded as 2D seismic”, as below in Figure A.15.

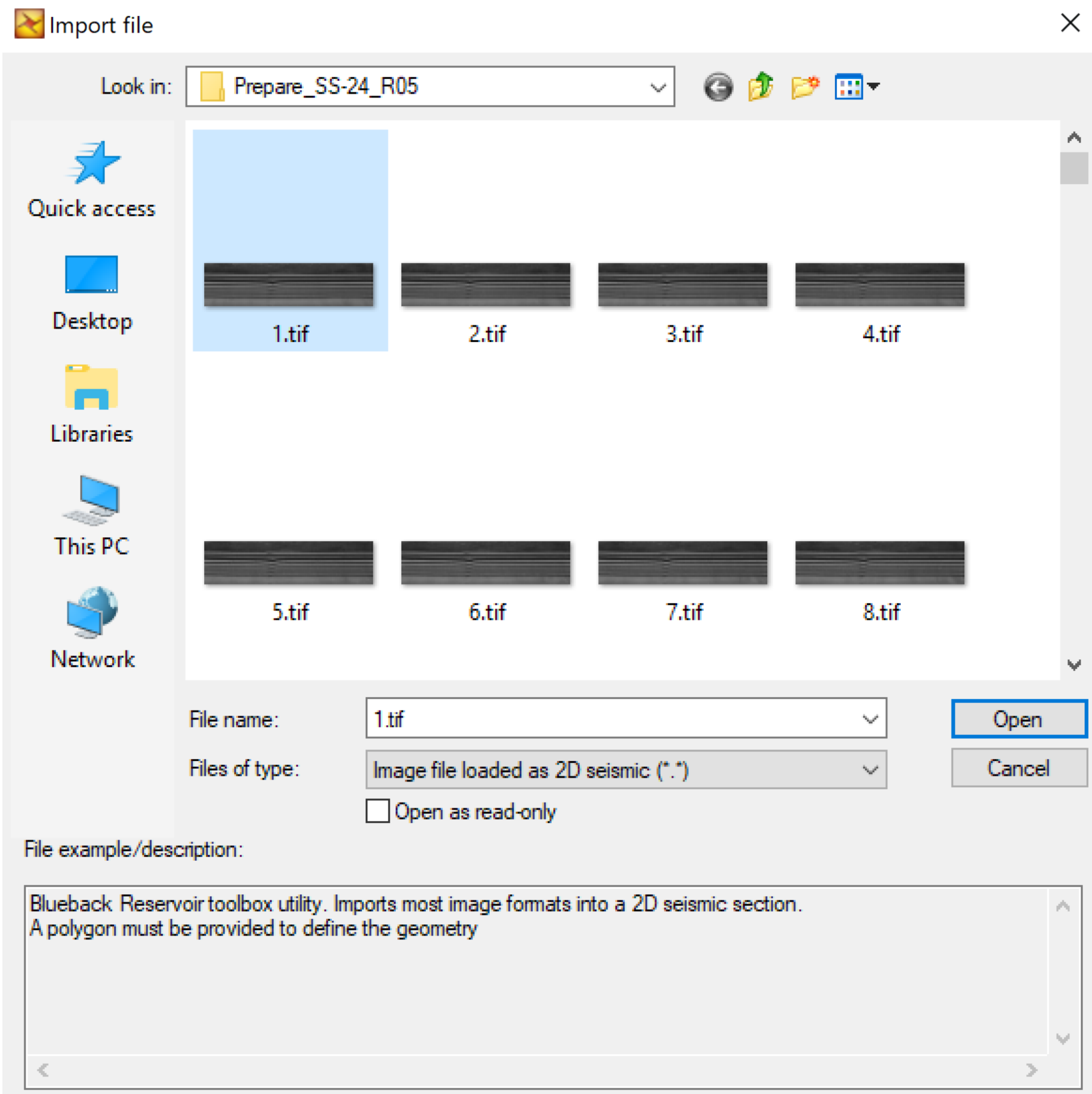

Figure A. 15 Step to select the first sandbox tiff file in the import process.

Select the depth domain and set up the thickness of the sandbox using the Top and Bottom parameters (Figure A.16). Recall that the recommended depth scale is 1 cm in the sandbox is equal to 1000 m in nature. Make sure that the selected tiff file (the first item) are matched with the polygon (the fifth item). Repeat this process for the second tiff file & polygon 2, the third tiff file & polygon 3, …, .

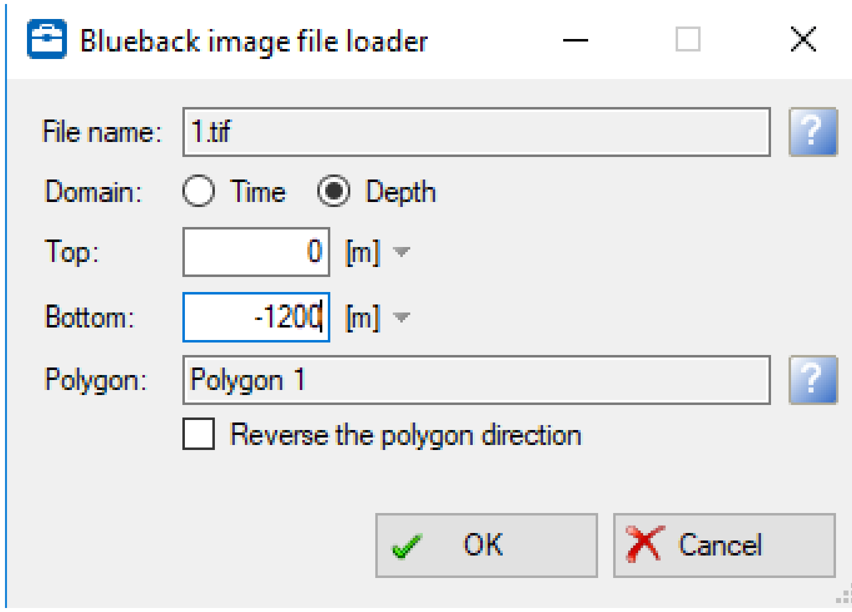

Figure A. 16 Step to set up depth domain and sandbox thickness.

The final results should be as in the Figure A.17. If unsure how to display the seismic cube, follow these instructions: at top menu click “Window”, then “3D window”. Turn on Survey 2 and click on all lines. Then set aspect ratio to 1.

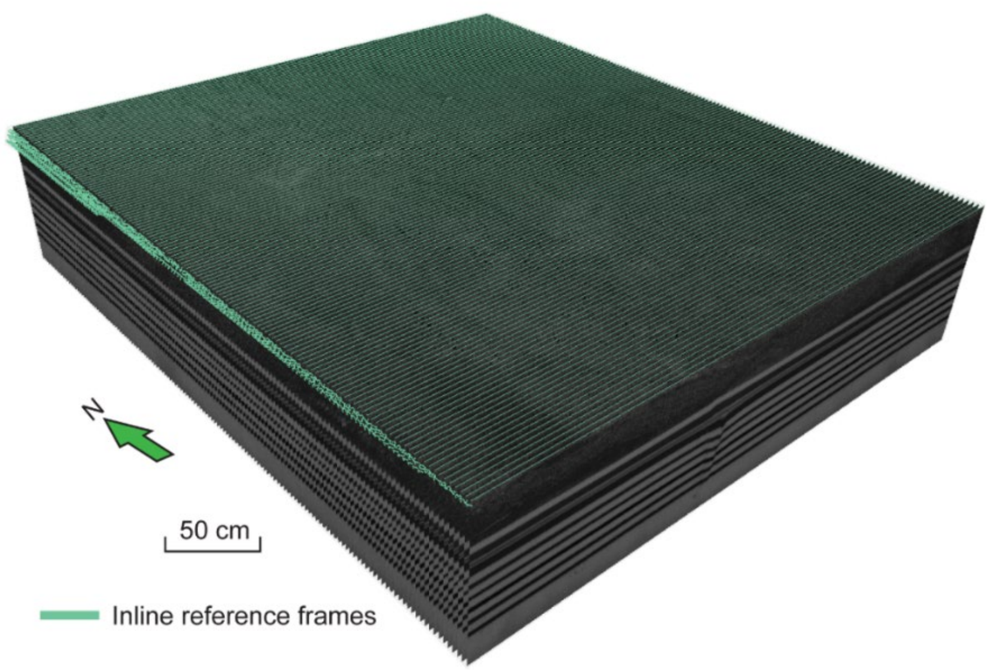

Figure A. 17 Final results for sandbox tiff image import.

Step 2: Create sandbox seismic cube from imported images

To create the seismic cube from the tiff file, launch the Blueblack Toolbox from Cegal plug-in from the top menu. The ‘Merge and resample seismic’ module is required as in Figure A.18. Drop all of sandbox images from ‘Survey 2’ into a seismic white box (Figure A.18). Set the domain to be depth(Z) using the button next to the menu label “Seismic:”. Then put the dummy cube ‘Empty cube 1’, which created in section 1.1, into the “Take lateral lattice definition from seismic, surface or model grid:” white box (Figure A.18). Make sure that the bottom depth(Z) of seismic cube is matched with bottom depth value of the imported sandbox images. Click OK.

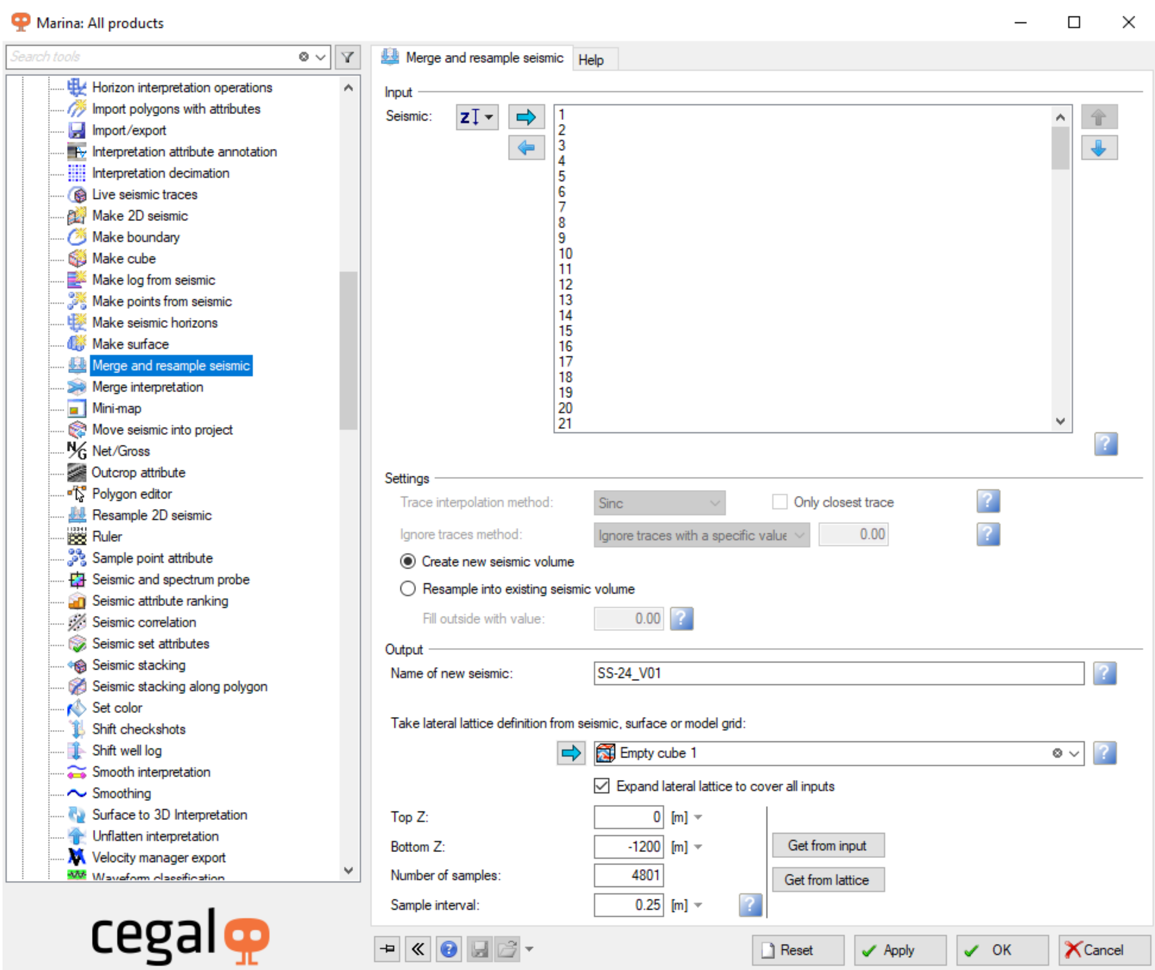

Figure A. 18 Step to create the sandbox seismic cube by using Blueblack Toolbox plug-in.

Results:

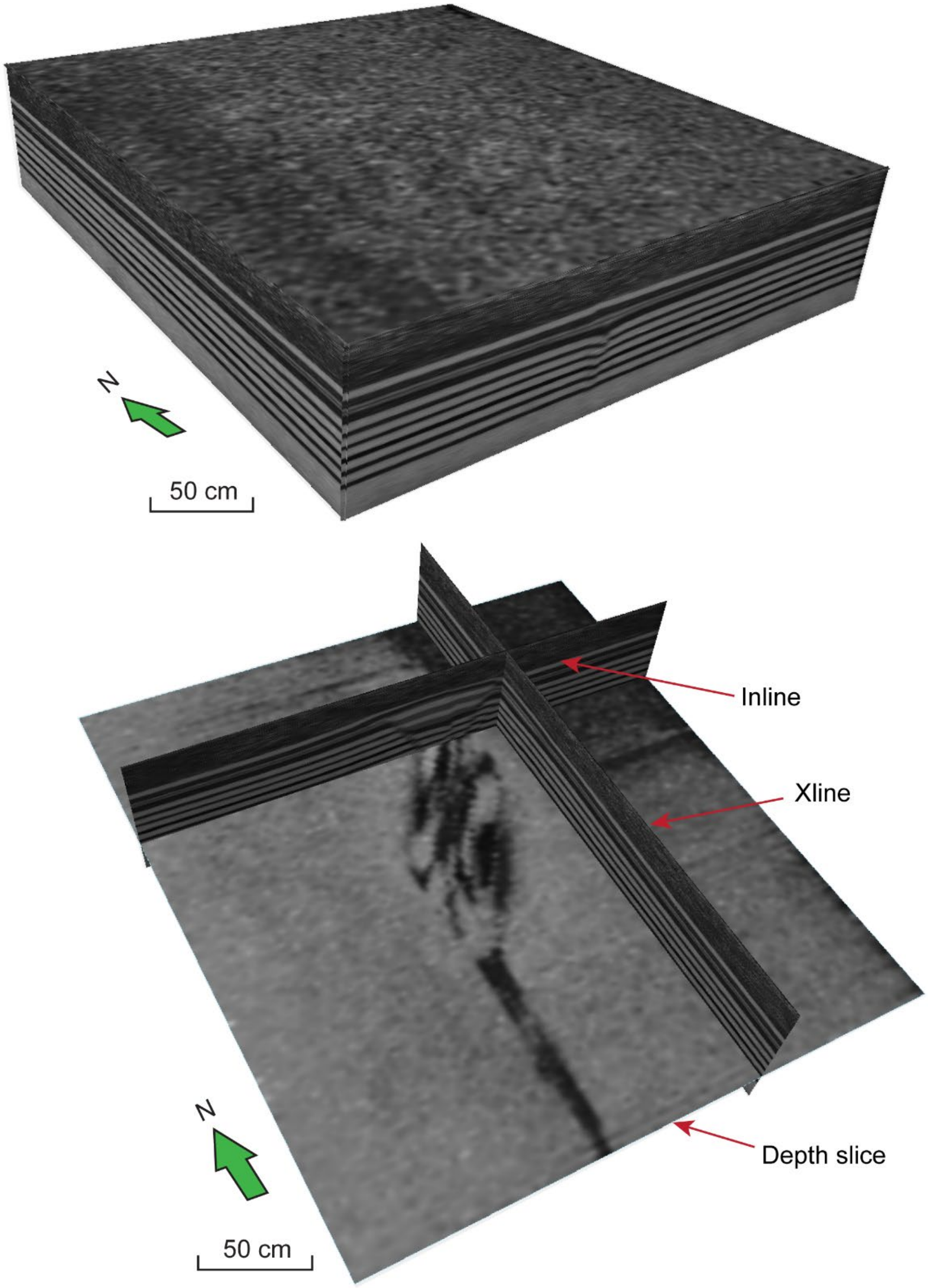

Figure A. 19 Seismic cube which is created from sandbox tiff files.

2. Analysis fault dip angle and dip direction from structural framework in Petrel software

To measure the fault dip angle and fault dip direction, the 3D structural framework is required. The whole structural framework should be finalized before analyzing the fault dip angle and dip direction. The process to create 3D structural framework in Petrel software will be excluded from this appendix section. Please find the process in the Petrel GURU section.

Step 1: Fault dip angle and dip direction analysis operation

The ‘SS-24 model’ 3D structural framework was created as in the ‘Models’ panel in Figure A.20. To measure the dip angle and dip direction in the structural framework, right click on one of the fault planes. Then select the ‘structural operation’ and select the ‘dip/dip direction’ as in Figure A.21.

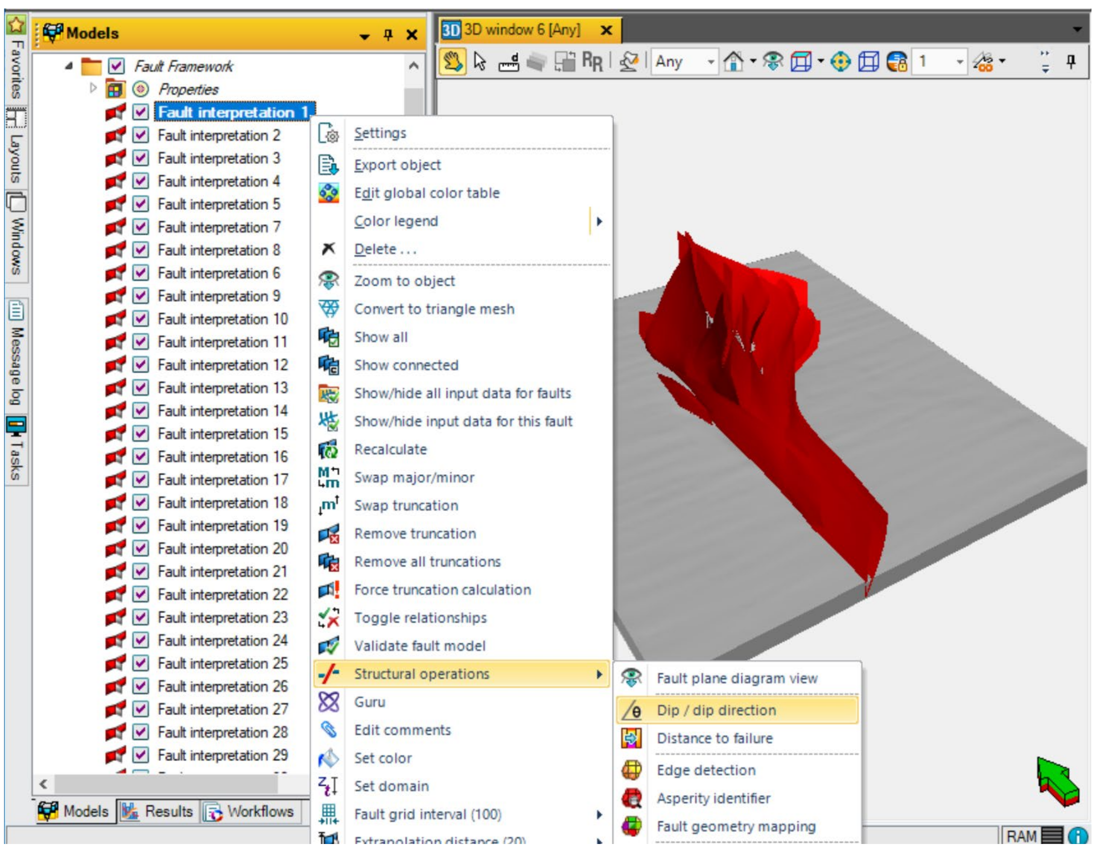

Figure A. 20 Step to measure dip angle and dip direction on fault framework model.

Select white boxes on both fault dip and fault dip direction. To process all the fault at the same time the folder icon in the bottom right corner must be selected. Then run the measurement (Figure A.21).

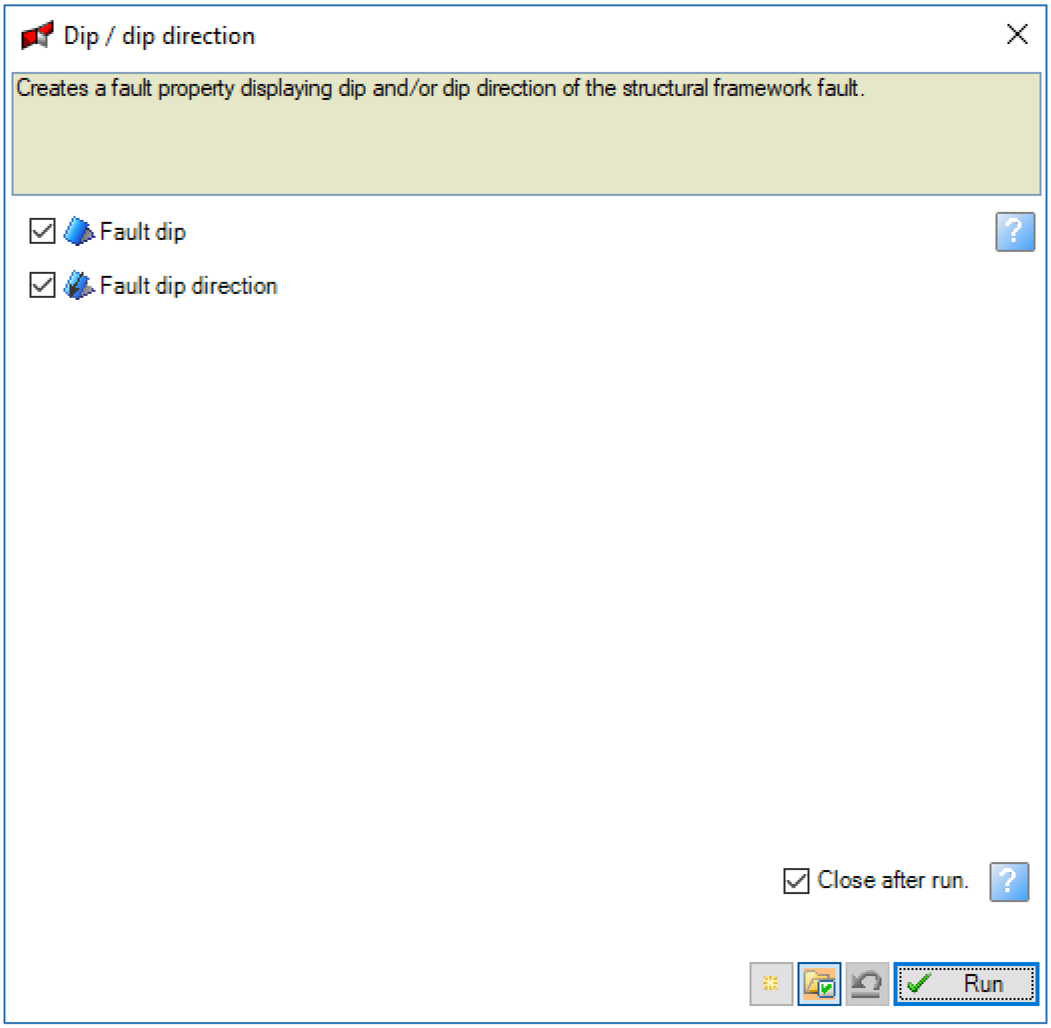

Figure A. 21 Step to measure fault dip angle and dip direction.

The fault dip angle and dip direction results will be measured and put under the properties as in Figure A.22.

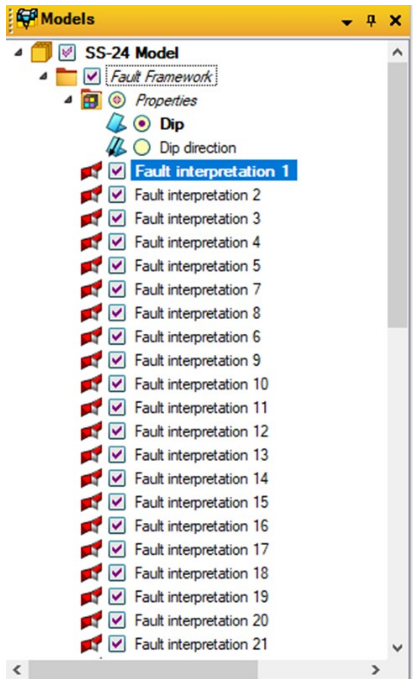

Figure A. 22 Results of fault dip angle and dip direction measurement.

Results:

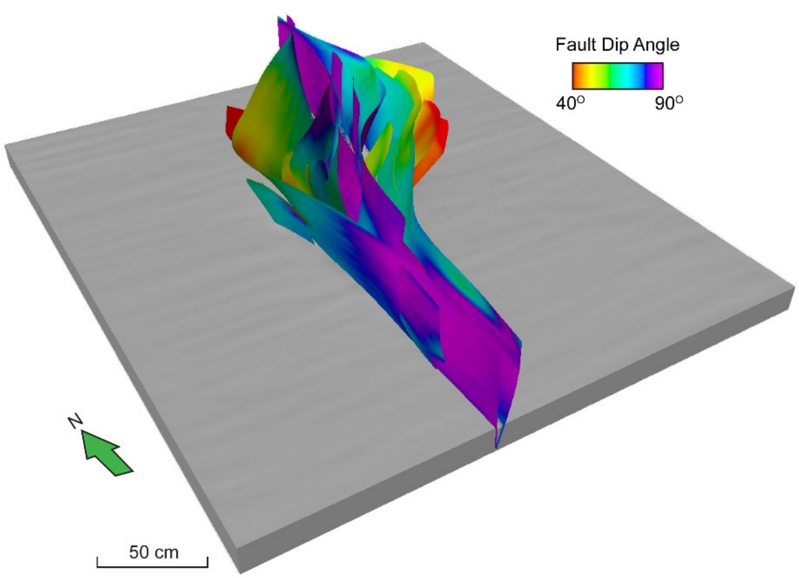

Figure A. 23 Result of fault dip angle measurement.